DROP AND IMPACT DYNAMICS ANALYSIS OF HARD DISK DRIVE (HDD) SYSTEMS

GU BIN

School of Mechanical & Aerospace Engineering

A thesis submitted to the Nanyang Technological University
in partial fulfilment of the requirement for the degree of
Master of Engineering

2016

ABSTRACT

Nowadays, hard disk drives (HDDs) are widely used in portable consumer appliances and gadgets. These HDDs are more susceptible to shock and vibration during using. Their shock performance under operation and non-operation is becoming an increasingly important issue. One important damage mode of the HDD is the "head slap" behaviour, which is triggered by a shock load that exceeds the suspension preload, causing the head to fly off from the disk and then slap on the disk. Thus, the particles generated on the disk medium may cause contamination problem. The head slap should be strictly avoided. One approach for dealing with the shock problems is to design a robust mechanical system and slider/disk interface.

It is very clear that the trend of the HDD development is higher areal density and higher speed. The size of the HDD and its components become smaller and smaller. The improved performance of the mechanical parts has been of great significance in this progress. A better understanding of dynamic characteristics of the mechanical parts is essential. To investigate the drop and impact dynamic characteristics of hard disk drives, both experiments and numerical simulations are conducted here.

Firstly, the boundary condition of disk of an HDD was investigated by finite element analysis and experimental tests. Modal analysis is conducted with simplified FE model and the results are compared with experimental results. The real boundary condition of disk is simulated with FE model considering the contact between clamp and disk and the contact between disk and hub. Based on the contact model, design

parametric studies are conducted. It is found it help to decrease the shock response of the disk with higher clamping force and higher contact stiffness between disk and hub. The effect of clamping force on the shock response of the disk is further verified experimentally. The experimental results were agreeable with the numerical results.

Secondly, both linear drop tests and rotary drop tests simulation were conducted. The HDD shows more sensitivity to the shorter duration shock. And the magnitude of the slider lift-up height grows significantly with the greater amplitude of shocks. Comparison between linear drop tests and rotary drop tests shows that the slap behavior in linear drop tests is more significant than in rotary drop tests. The fragility test on head slap was conducted experimentally. The results confirmed the numerical result that drives under linear drop test with greater amplitude and shorter duration shock was more vulnerable in consideration of the head slap behavior. Moreover, the effect of inclination angle on the head slap behavior was investigated experimentally.

Thirdly, an FEM model of operational HDD is developed. The air bearing between the disk and the slider is modeled by nonlinear springs. The nonlinearity of the vertical stiffness of the air bearing is considered. The contact between the disk and the slider is also considered. The disk clamping condition and the shock pulse amplitude and width effects are investigated. This numerical model can be applied to predict the shock tolerance during the design stage.

Fourthly, strain gauge was for the first time used to measure the dynamic strain of the HAA of an HDD in drop tests. It shows that the mounting of the stain gauge causes the increase of the natural frequency of the HAA and the first mode shape

dominates the shock response of the HAA. The maximum strain and the damping increases with the amplitude of the shock pulse. The maximum strain increases with the pulse width of the shock pulse. The effect of the pulse width on the damping is more complicated and can be further investigated in future studies. This work suggests the measurement of the dynamic strain of the HAA is conductible. A new way of measuring the shock response of small form factor HDD is proposed.

Finally, dynamic contact forces and impact-induced vibration of an HAA are measured and simulated by using LMM method and FEA. LMM method utilizes the first principles of Second Newtonian Law and the Doppler frequency shift and minimizes the uncertainties of using many sensors. A good agreement between the FEA results and experimental data is observed. The limitation of the current experimental setup in oblique impact test and in inelastic impact test is verified by the FEA. This initial attempt demonstrates the feasibility of applying FEA and LMM method to minute dynamic forces measurement involved in HDDs.

ACKNOWLEDGMENTS

It is my great pleasure to express my sincerer gratitude to my supervisor A/P Shu Dongwei, David, for his valuable guidance, careful instructions, kind help and constant encouragement throughout the course of this project.

I am highly indebted to Prof. Yusaku Fujii, Dr. Shi Baojun, Dr. Madhusudhana Rao Parlapalli, Dr. Della Christian Ngalatan and Dr. Luo Jun, for all their help, discussions and comments on issues encountered in the work. I am grateful to A/P Yap Fook Fah, Dr. Liu Mengjun, Dr. Ao Hongrui, Dr. Liu Yan and Dr. Hendri Harmoko from NTU, Mr. Quock Y Ng, Mr. Samuel Gan, Mr. Terang Thia and Mr. Joseph H T Lau from Seagate Technology, for their valuable advice, helpful discussion, important information during this project.

I would like to thank technicians in the Center for Mechanics and Micro-System Laboratory and the Strength of Materials Laboratory, for providing technical support. I would like to take great pleasure in acknowledging the financial support from Nanyang Technological University, Singapore.

I am thankful to all my friends and well wishes for their backing and encouragement.

Finally, special thanks to my wife, Nie XM and my father, for their continuous encouragement and support. Dedicated to my beloved Mom in heaven.

TABLE OF CONTENTS

LIST OF FIGURES

LIST OF TABLES

LIST OF ABBREVIATIONS

HDD	hard disk drive
FDB	fluid dynamic bearing
FE	finite element
HAA	head arm assembly
HDA	head disk assembly
CML	Computer Mechanics Laboratory, Univ. Of Berkeley
LDV	Laser Doppler Vibrometer
S1	one-inch small form hard disk drive from Seagate
DMSA	dual mass shock amplifier
HSA	head stack assembly
VCM	voice coil motor
HSA	head suspension assembly
HDI	head disk interface
CSS	contact start stop
DOF	degree of freedom
fps	frames per second
PDA	personal digital assistant
FEM	finite element method
PC	personal computer

CHAPTER 1

INTRODUCTION

1.1 Background

Hard disk drive (HDD) is one of the most important and also one of the most interesting components within a computer. Nowadays, hard disk drives are widely used in portable consumer appliances and gadgets. These HDDs are more susceptible to shock and vibration. Their shock performance under operation and non-operation is becoming an increasingly important issue. Current technological improvements are requiring more robust shock testing of hard disk drives with half-sine pulse acceleration profiles of 500-1000g amplitudes and 0.5-2.5 ms in durations.

When an HDD is subjected to a high level of acceleration shock, the head suspension system lifts off the disk and lands on it in a very short time, and the impact during this slap often leads to failure of the head mode. This head slap behaviour should be strictly avoided.

There are essentially three approaches for dealing with the shock problems. The first is to design a suitable isolation installation for the disk drives. The second is to design a robust servo control mechanism to prevent read/write error during the shock. The

third is to design a robust mechanical system and slider/disk interface [6]. We focus on the third one.

There have been various experimental and numerical studies on shock response of the mechanical system and its effects on the head/disk interface. However, much of the published works have been limited to the non-operating state of the drives, and/or to the component level. Wilson and Bogy [1] performed modal experiments of a suspension loaded on a 5 1/4-inch rotating disk, and they found that when a natural frequency of the suspension is close to one of the natural frequencies of the disk, two resonant frequencies are created after the components are coupled together. Jayson *et al* [2] investigated the effects of air bearing stiffness on an operational HDD subject to shock and vibration by finite element simulation. In their finite element model, the air bearing stiffness was determined from a finite element solution of the Reynolds equation and approximated with linear springs. Because of the approximate modeling of the air bearing using linear springs, they were not able to capture the true behaviour of the air bearing. Shi, *et al* [3-5] investigated the pulse shape effects in a shock analysis of an actuator arm of a hard disk drive. An opposite phenomenon was observed in the shock response of the actuator arm and explained by power spectrum analysis.

1.2 Objectives

This project aims to investigate the drop and impact dynamic characteristics of hard disk drives. They includes:

- Study of drop dynamic characteristics of HDDs, particularly the major factors that contribute to the head slap behavior of the HDDs.
- Development of effective shock resistance methods to reduce the head slap behavior during drop tests. To measure and evaluate the shock response of the HDDs.
- Development of levitation mass method （LMM） method and FEA model to evaluate the minute dynamic forces involved in HDDs.

1.3 Scope

This project is concerned with the numerical and experimental studies. The scope covers the following aspects.

Modeling: A completed finite element model will be developed to simulate the shock response of the small form factor drive under non-operation and operation state. The model will be composed of the head-suspension-actuator with pivot bearings, the base plate, the air bearing,

Experimental techniques: The shock response of the HDD will be measured during the drop tests, especially the lift-off height of the sliders. The non-contact measurements will be implemented by using high speed digital video camera and the LDV (Laser Doppler Vibmometer), which enable the non-contact and high-speed measurement. Strain gauge will be implemented in the measurement of shock response of HAA (head arm assembly). The dynamic contact forces and impact-induced vibration of an HAA are measured and simulated by using LMM method.

LMM method utilizes the first principles of Second Newtonian Law and the Doppler frequency shift and minimizes the uncertainties of using many sensors.

Correlation of simulation and experiment: The results from both experimental measurement and numerical simulation will correlate with each other. Some of the difficulties encountered in the simulation or experiment will be overcome through in-depth understanding of the finite element model and the experimental measurement.

Parametric studies: Design parametric studies will be conducted based on the finite element model to enhance the shock resistance of the disk drives. The prediction of the shock response is vital for short design cycle in an increasing fast changing data storage industry. An accurate Finite element simulation will substantially reduce the time and number of tests needed in the design phase of a disk drive.

Hard disk drives: A one-inch small form factor HDD, S1, from Seagate Technology will be used for the numerical modeling and experimental tests mainly.

1.4 Dissertation Outlines

This report is organized into 7 chapters. The background, the objectives and the progress of the project is introduced in Chapter 1. The literature about the history and the structure of the HDD, the development of experiments and numerical simulation of the drop test of HDDs is reviewed in Chapter 2. The basic principles for the drop test of HDDs are presented in Chapter 3. Numerical analysis of the shock response of HDDs is presented in Chapter 4. In Chapter 5, shock response is investigated through

experiments. In Chapter 6, dynamic forces of a head arm assembly (HAA) against an impact load and in free oscillation are measured by means of non-linear finite element analysis (FEA) and experiments using a modified levitation mass method (LMM). Conclusions and future work are summarized in Chapter 7.

CHAPTER 2

LITERATURE REVIEW

The trend of the HDD development is higher and higher areal density and speed. The size of the HDD and its components become smaller and smaller. The improved performance of the mechanical parts has been of great significance in this progress. Among these, the shock resistance of the more and more elaborate parts is one of the most important guideline in the design of HDD. Almost all the failure of the HDD during the shock is due to the large displacement or acceleration of the head arm assembly (HAA).

A review is given here for the structure and the details of the HAA, HDI and the HDD, its developments, and the challenges of the shock resistance in current time. Some important works about the reliability, the modal analyses and the shock resistance of the HAA, HDI and the HDD are introduced. The theoretical analyses, experiments and numerical simulations have been used by the researchers in the literature.

2.1 History of Hard Disk Drives (HDDs)

The hard disk drive has short and fascinating history. Before the disk drive there were drums. In 1950 Engineering Research Associates of Minneapolis built the first commercial magnetic drum storage unit for the U.S. Navy, the ERA 110. It could store one million bits of data and retrieve a word in 5 thousandths of a second. In 1956 IBM invented the first computer disk storage system, the 305 RAMAC (Random Access Method of Accounting and Control). This system could store five

MBytes. It had fifty, 24-inch diameter disks. By 1961 IBM had invented the first disk drive with air bearing heads and in 1963 they introduced the removable disk pack drive.

In 1970, an eight-inch floppy disk drive was introduced by IBM. In 1973, IBM shipped the model 3340 Winchester sealed hard disk drive, the predecessor of all current hard disk drives. The 3340 had two spindles each with a capacity of 30 MBytes, and the term "30/30 Winchester" was thus coined.

In 1980, Seagate Technology introduced the first hard disk drive for microcomputers, the ST506. It was a full height (twice as high as most current 5 1/4" drives) 5 1/4" drive, with a stepper motor, and held 5 Mbytes. In the early 80's, the first 5 1/4" hard disks with voice coil actuators started shipping in volume, but stepper motor drives continued in production into the early 1990's. In 1981, Sony shipped the first 3 1/2" floppy drives.

In 1986, the first 3 /12" hard disks with voice coil actuators were introduced by Conner in volume, but half (1.6") and full height 5 1/4" drives persisted for several years. In 1988, Conner introduced the first one inch high 3 1/2" hard disk drives. In the same year, PrairieTek shipped the first 2 1/2" hard disks.

In 1997, Seagate introduced the first 7,200 RPM, Ultra ATA hard disk drive for desktop computers and in February of this year they introduced the first 15,000 RPM hard disk drive, the Cheetah X15.

In 2000, IBM triples the capacity of the world's smallest hard disk drive. This drive holds one gigabyte on a disk, which is the size of an American quarter.

Fig. 2.1 shows the evolution of IBM hard disks over the past years. Several different form factors are illustrated, showing the progress that they have made over the years in terms of capacity. The improved performance of the mechanical parts has been of great significance in this progress. Among these, the shock resistance of the more and more elaborate parts is one of the most important guideline in the design of HDD. Almost all the failure of the HDD during the shock is due to the large displacement or acceleration of the HAA.

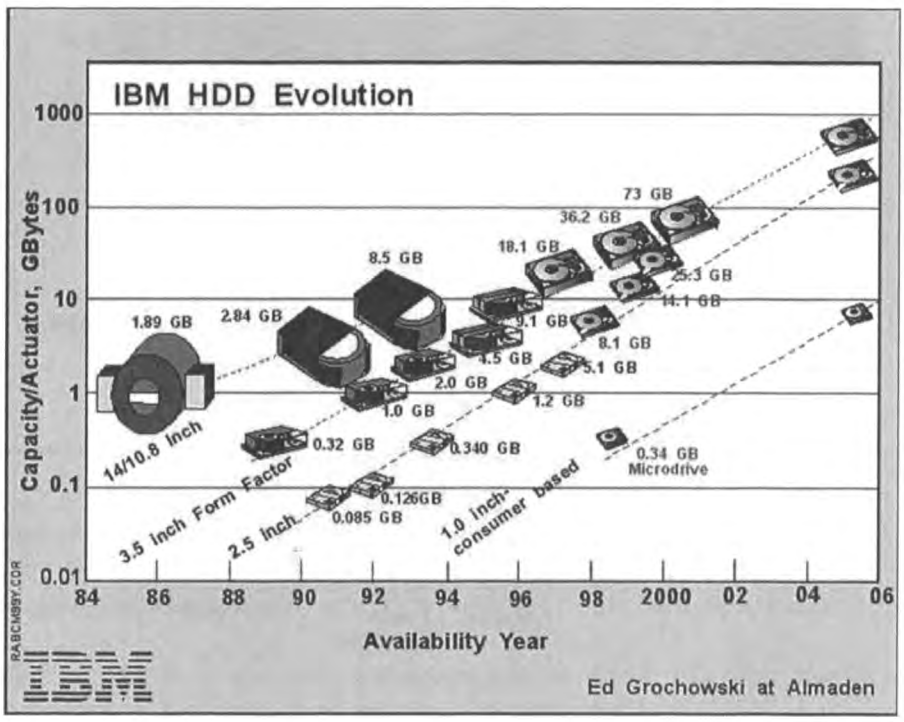

Fig. 2.1 IBM HDD evolution[①]

2.2 Structure of the HDD

Fig. 2.2 shows a photograph of a modern SCSI hard disk, with major components annotated. The platters are mounted by cutting a hole in the center and stacking them onto a *spindle*. The platters rotate at high speed, driven by a special *spindle motor* connected to the spindle. Special electromagnetic read/write devices called *heads* are mounted onto *sliders* and used to either record information onto the disk or read information from it. The sliders are mounted onto *suspension* and *arms*, all of which are mechanically connected into a single assembly and positioned over the surface of the disk by a device called *actuator*. A *logic board* controls the activity of the other components and communicates with the rest of the PC.

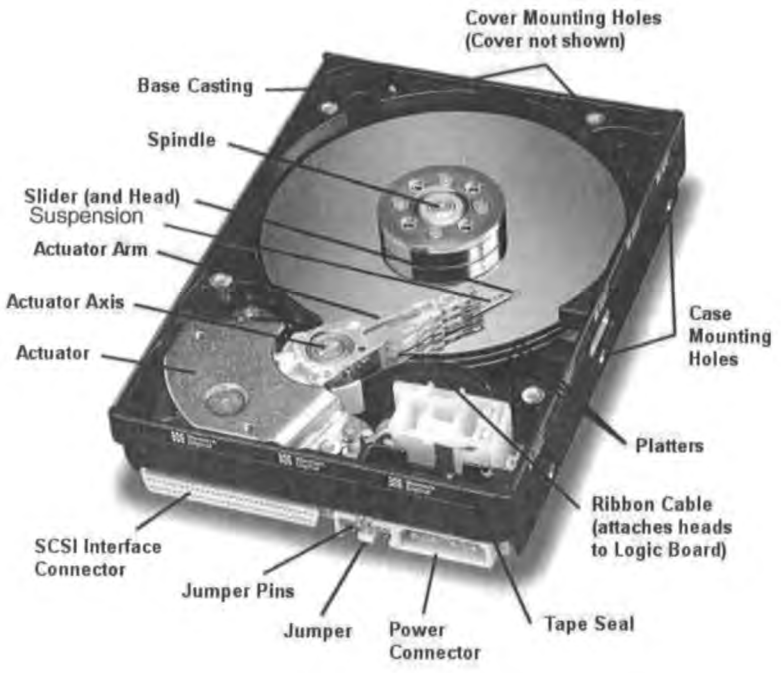

Fig. 2.2 Photograph of a modern SCSI hard disk[①]

- **Head Actuator Assembly**

The hard disk platters are accessed for read and write operations using the read/write heads mounted on the top and bottom surfaces of each platter. Obviously, the

read/write heads don't just float in space; they must be held in an exact position relative to the surfaces they are reading, and furthermore, they must be moved from track to track to allow access to the entire surface of the disk. The heads are mounted onto a structure that facilitates this process. Often called the *head actuator assembly*, it is comprised of several different parts, as shown in Fig. 2.3. The *head arm assembly* (HAA) includes all the parts excluding the actuator parts.

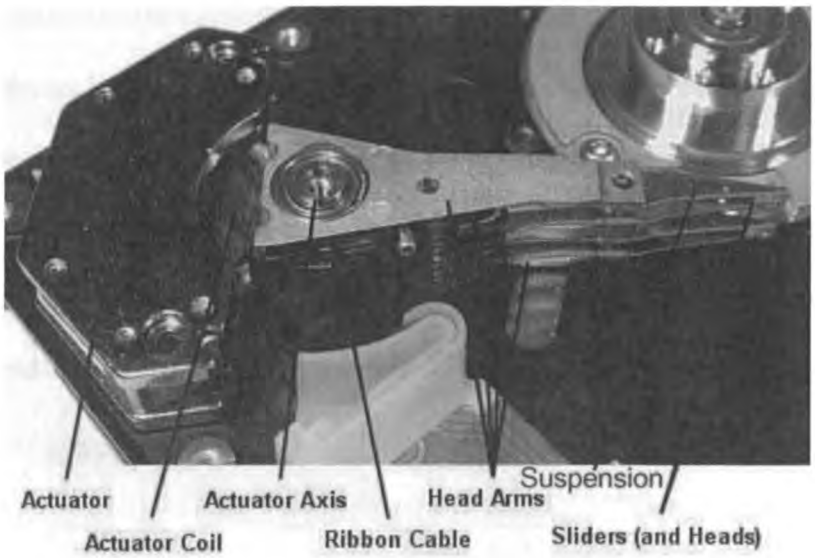

Fig. 2.3 Structure of a typical PC head actuator assembly[1]

- **Head actuator**

The actuator is the device used to position the head to different tracks on the surface of the platter. The actuator is a very important part of the hard disk, because changing from track to track is the only operation on the hard disk that requires active movement: changing heads is an electronic function, and changing sectors involves waiting for the right sector number to spin around and come under the head (passive movement). Changing tracks means the heads must be shifted, and so making sure this movement can be done quickly and accurately is of paramount importance. This

is especially so because physical motion is so *slow* compared to anything electronic--typically a factor of 1,000 times slower or more.

As shown in Fig. 2.4, the actuator in a modern hard disk uses a device called a *voice coil motor* (VCM) to move the head arms in and out over the surface of the platters, and a closed-loop feedback system called a *servo system* to dynamically position the heads directly over the data tracks. The VCM works using electromagnetic attraction and repulsion. A coil is wrapped around a metal protrusion on the end of the set of head arms. This is mounted within an assembly containing a strong permanent magnet. When current is fed to the coil, an electromagnetic field is generated that causes the heads to move in one direction or the other based on attraction or repulsion relative to the permanent magnet. By controlling the current, the heads can be told to move in or

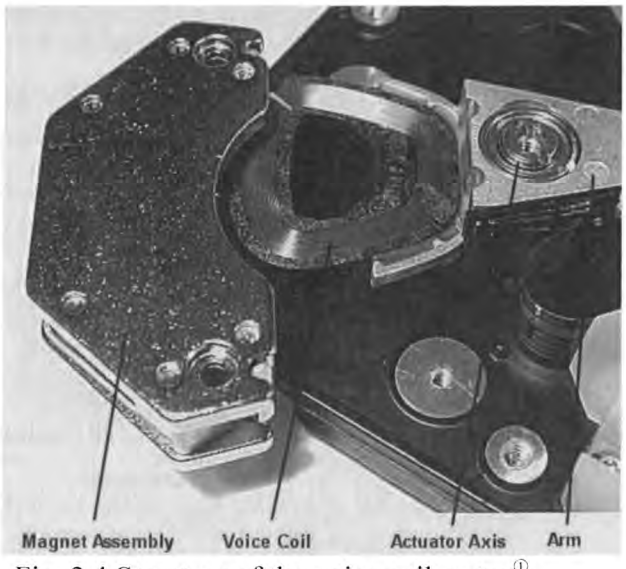

Fig. 2.4 Structure of the voice coil motor[①]

out much more precisely than using a stepper motor. All PC hard disk voice coil actuators are *rotary*, meaning that the actuator changes position by rotating on an axis.

- **Head Sliders**

Hard disk read/write heads are too small to be used without attaching them to a larger unit. This is especially true of modern hard disk heads. Each hard disk head is therefore mounted to a special device called a *head slider* or just *slider* for short. The function of the slider is to physically support the head and hold it in the correct position relative to the platter as the head floats over its surface.

Sliders are given a special shape to allow them to ride precisely over the platter. Usually they are shaped somewhat like a sled; there are two rails or runners on the outside that support the slider at the correct *flying height* over the surface of the disk, and in the middle the read/write head itself is mounted, possibly on another rail. As hard disk read/write heads have been shrinking in size, so have the sliders that carry them. The main advantage of using small sliders is that it reduces the weight that must be yanked around the surface of the platters, improving both positioning speed and accuracy. Smaller sliders also have less surface area to potentially contact the surface of the disk in the impact or drop leads the failure of the hard disk.

- **Suspension**

The suspensions are thin pieces of metal, usually triangular in shape onto which the head sliders (carrying the read/write heads) are mounted. There is one suspension per read/write head, and all of them are lined up and mounted to the head actuator to form a single unit. This means that when the actuator moves, all of the heads move together in a synchronized fashion. Heads cannot be individually sent to different track numbers. The suspensions are made of a lightweight, thin material, to allow them to be moved rapidly from the inner to outer parts of the drive. Newer designs have replaced solid arms with structural shapes in order to reduce weight and improve

performance. Newer drives achieve faster seek times in part by using faster and smarter actuators and lighter, more rigid head arms, allowing the time to switch between tracks to be reduced. Therefore, the shock resistance of the suspensions is reduced and should be treated carefully.

Fig. 2.5 shows a photograph of a one-inch small form factor HDD, S1, from Seagate Technology. The major components/assemblies are annotated, with its top cover removed. The drive consists of a one-inch disk rotated by a fixed-shaft spindle motor, two actuator arms that are driven by a voice coil motor, two suspension assemblies, a base plate and a cover. When power is applied, the disk rotates in a steady state at a speed of 3,600 RPM. The slider(s) fly over the surfaces of the disk on the air bearing, which is generated by the relative motion between the rotating disk and the stationary slider(s).

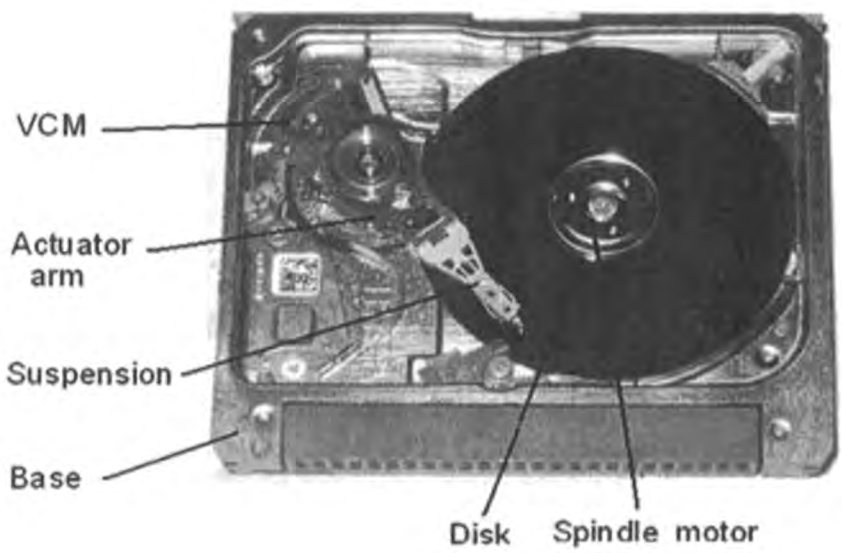

Fig. 2.5 One-inch small form factor HDD and its internal components

2.3 Experiments

2.3.1 Non-operational drop tests

Several investigations have been performed in the past concerning the non-operational drop tests, including the linear drop tests and the rotary drop tests.

In a previous study by Allen and Bogy [7], the effect of shock on the head-disk interface(HDI) was studied and the experimental shock data for the head-disk interface were compared with numerical results from a finite element model. The experimental apparatus was designed as shown in Fig. 2.6. The acceleration produced by free falls was measured by the accelerometer affixed to the hub. Corrugated cardboard was chosen as a cushioning material to produced shocks approximately 0.5 milliseconds in duration. A Spin Physics 2000 high speed video camera was used to

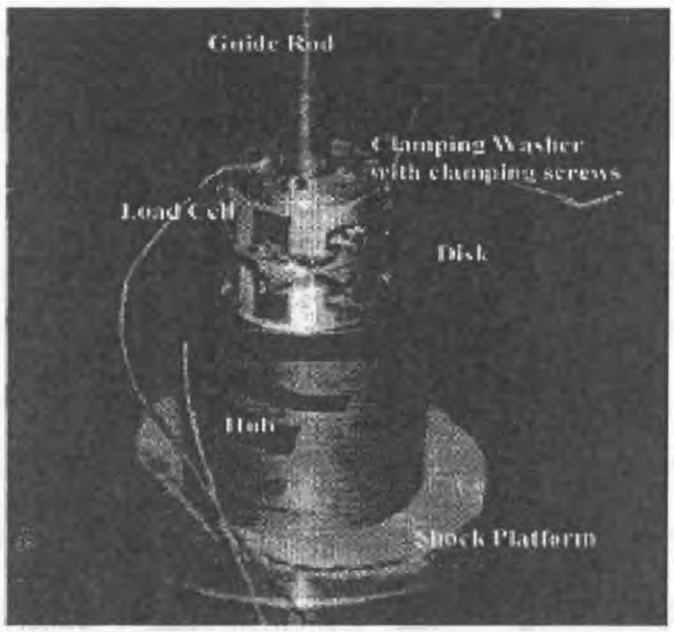

Fig. 2.6 The experimental apparatus [7]

record the motion of the slider, the suspension and the disk at 2000 frames per second. The suspension and the disk were electrically insulated except at the head-disk interface so that the voltage change resulting from their separation could be recorded and a time of separation established. The dynamic response of the numerical model was qualitatively similar to that of the experimental apparatus. This study is limited to the non-operating state of the drives and to the component level. The model considered only the effects of the disk and suspension arm on the magnetic head for the case of a linear shock where the impact surface is parallel to the disk. In the experiment, there were only a few data presented. The detailed shock response of disk and arm, such as displacement, velocity and acceleration, was not presented. The experimental apparatus can produce higher amplitude and shorter duration shocks. But it is difficult to produce a standard half-sine acceleration pulse.

Kumar *et al* [8] studied the mechanics at the hard disk interface caused by an input shock. Experimental results and a dynamic impact model were used to analyze the problem. The experimental setup was shown in Fig. 2.7. The disk was mounted on a rigid post and the HSA was mounted on a production arm which in turn was mounted on an insulating post. The entire unit was tilt dropped from various heights onto a smooth hard surface. Two sets of impact mechanics data were collected apart from the input acceleration pulse itself. The full body capacitance between the slider and the disk was measured during the impact process. This resulted in a measure of the slider separation from the disk. To enable a fine resolution measurement of the slider impact, the head-suspension assembly (HSA) was instrumented with four piezoelectric microsensors at the four corners of the slider. The sensors were designed to be sensitive to impacts normal to the disk. Their paper addressed the head disk

interface (HDI) damage in a drive designed for contact start stop (CSS), when expose to shock under non-operational conditions. The HDI failure occurs when the slider overcomes the preload and separates from the disk surface upon impact. Although this type of failure can be largely avoided through the use of a load-unload design [9], it may still be desirable to retain a CSS design to other considerations such as space and reliability. Kumar, *et al*'s results indicated that disk vibration becomes significant for narrow pulse width shocks. In such cases, the energy transfer from the disk to the slider can be larger enough to lift the slider even when it is on the top surface of the disk. Their analysis underscored the importance of all individual components toward a single failure mechanism, and highlighted the need to consider the entire drive as a single unit.

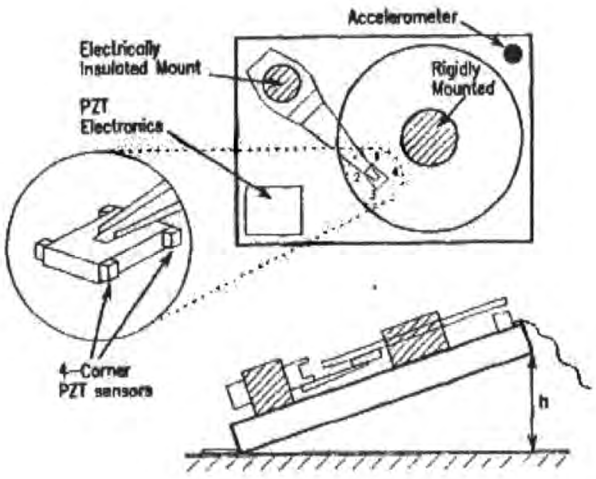

Fig. 2.7 The experimental setup [8]

Marek, *et al* [10] reduced the problem to a single degree of freedom (DOF) model, neglecting disk motion while focusing on the cantilever mode of the suspension. An experimental method that have been developed by Hutchinson Technology to assess shock performance of head suspensions were described in their article. The test consists of dropping preloaded suspension at various shock loads, recording and

measuring the slider travel using a high-speed video system, and then plotting the shock amplitude versus travel. Most of those methods are in the evolutionary stage.

The dynamic performance of three different suspensions during shock was studied by Jen *et al* [11] through both finite element simulations and experiments to determine the frequency responses function for in-plane and out-of –plane vibrations of different suspensions during shock. In the experiment, a random excitation is applied to the base plate of the cantilevered suspension with slider (no air bearing), and the velocity of a test point on the load beam in the Z-direction is measured with an LDV and an oscilloscope. The acquired signal is then transformed into the frequency domain to observe the first peak in the power spectrum.

Lee *et al* [12] built a theoretical model for prediction the shock behavior of the suspension in order to get a shock improved design. Their model consisted of a single DOF mass-spring system and a continuous system model with a single disk and spindle. A shock testing apparatus was constructed, tested and characterized. The apparatus consisted of a stationary platform, a dummy disk, and a jig for mounting the HSA. They used an electrical on/off switch between head and disk, which was one of the traditional methods to measure whether the head and the disk were in contact with each other. But the exact quantitative dynamic displacement of the head can not be measured by this experimental apparatus. The calculated results obtained from their model were compared with the results of finite element simulations and experimental data and found that the head lift-off entirely depended on dynamic behavior of the suspension at non-operation, the suspension geometry design was found to be very important to improve the shock performance of the HDI, especially the length of

suspension. On the other hand, the dynamic response of the head was fully controlled by shock response of the disk when the head was put on the middle or outer diameter of the disk.

Takahashi *et al* [13] investigated the 8 parameters of the suspension shape by using Taguchi method. A series of experiments were conducted to optimize the design of the suspension for high shock resistance. The thickness of the suspension was found the most sensitive factor. The effect of the actuator pivot unbalance on the track-following response of modern disk drives to external linear vibration and shock was investigated by Radwan *et al* [14].

Some researcher and engineers gave out some modifications to improve the shock durability through different ways. Kouhei *et al* [15] viewed the motion of the complete slider-suspension assembly using a still camera and a stroboscope under shock acceleration, and confirmed that the slider tilted when it collided with the disk. They proposed fitting a "Jump stop" over the slider to decrease tilt angle and collision velocity, they confirmed that this stopper enables shock durability up to 6 times larger than without it. However, add such a large component will cause many other problems.

During the shock (or impact) analysis of a structure, the input loading can be approximated by a half-sine pulse, with narrower shocks corresponding to impact on harder surfaces [16]. The extent of damage on the disk was highly dependent, not only on the shock pulse amplitude, but also on the pulse width. Narrow pulse width shocks caused much more damage than shock with wide pulse widths. It has been shown that

loading intensity is an important parameter to determine material or structural failure mechanism in addition to total pressure impulse, e.g., pressure-impulse diagram has been used frequently to assess structural damages and human injuries when subjected to blast pulses [17, 18]. Several methods have been suggested to consider loading shape effects on structural response [18].

The previously recognized industry shock specifications (half-sine pulse acceleration profiles of 100 to 300g amplitudes and 3 to 11 millisecond in duration) have proven to be insufficient for the identification of the mechanisms that cause damage to the components of small portable drives. Currently new standards are being developed to adequately test and evaluate the roughness of portable drives and their components. These new standards include higher shock amplitudes of 500-1000 g and shorter durations of 0.5 to 2.5 ms.

Ishimaru [19] also developed an experimental set-up to study an HDI subjected to half-sine shock acceleration during non-operation using a dummy drive. He measured the degradation of recorded signals to investigate the permanent damage to the disk surface due to the collision between head and disk. He found that the slap movement of the HAA is the dominant phenomenon governing the shock-proof performance of an HDI. This movement did not occur until the inertia force acting on the HAA exceeds the loading force. It is more violent as the magnitude of an acceleration increase. Higher load force, smaller equivalent mass of the HAA, low rigidity, and higher hardness of the disk contribute to better shock-proof performance. The duration of shock acceleration is not related to resonance frequency of the disk but to

the HAA. Therefore, it is possible to estimate the slap movement quantitatively from the loading force, the equivalent mass of the HAA, and the duration of acceleration.

Similar works also have been conducted by Sohn *et al* [20] and found that there are two important factors for the actuator to endure high shock level. One is shock transmissibility and the other is the beating between the arm and the suspension, and the first bending natural frequency of arm was found to be the most important factor for the low shock transmissibility. For the experimental analysis, experimental set-up shown in Fig. 2.8 was used. This set-up was composed of sensors, an analyzer and a drop tester. Accelerometer measured the input acceleration, and the LDV (Laser Doppler Vibrometer) measured the motion of arm blade, suspension and slider. The structure of the drop tester was similar to that of the tilt drop tester and its drop motion is tilting drop. But it imposed a half sine pulse to the actuator and simulates the linear drop motion.

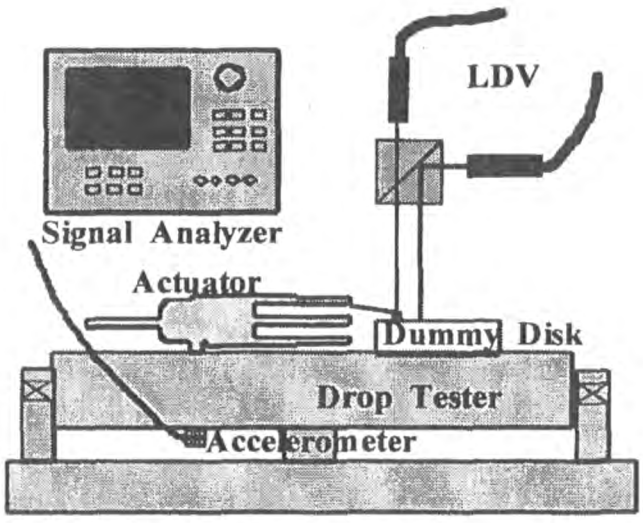

Fig. 2.8 The experimental set-up [20]

Through the high speed video camera, observation of a slider behavior after an external shock revealed that the slider jumps first and the re-contacts with the disks at its leading edge. Tokuyama *et al* [21] developed a suspension system that has a roof in the load beam that reduces the re-contact angle and the contact stress. They found that a magnetic disk device incorporating the system sustained no read errors for the external shocks up to 700 G.

Some new techniques were used by the researchers to identify and improve the shock characteristics when the hard disk drive is subject to external shock vibration. A 4-D shock-sensing and servo over-sampling scheme were presented and discussed by Chew K.K. [22]. This method was to maintain the data integrity when a drive is subjected to external shocks through re-design of the preamp, read channel and control software without additional cost of the drive. Lee *et al* [23] added a dynamic absorber in the actuator arm to assist in controlling the amplitude and acceleration of the actuator arm in disk drive so that it can improve the shock handling capability in both operation and non-operation condition.

A modification of the HDD based on the numerical analyses and experiments were introduced by Lee *et al* [24] to reduce the shock acceleration. The acceleration level was measured with a shock accelerometer in the perpendicular direction of rotational axis. The idea of this modification is changing the shock transfer path from shock input point to the points of interest. Although this modification has significant in mechanical modeling theoretically, it was hard to overcome the constraint of the given system and doesn't affect the shock behavior of the HDD. Therefore, they tried to change the impact environment in a viewpoint of contacting part in next turn. With

the proposed isolator attached system, contact force was decreased and it gave small amplitude of shock acceleration and longer time duration. They concluded that the most effective way to increase the shock resistance of the HDD was modifying the contacting part with attaching soft material to the base of the HDD.

Sanjeev et al [25] directly compare computational and experimental head slap data for a nonoperational hard disk drive. They subjected a nonoperational HDD to physical tilt-drop tests from drop angles of 10 and 45, representing a mild and a substantial shock input, respectively. They measured velocity responses with a laser Doppler vibrometer (LDV) at two points on the HDD. In the FE studies, the base plate velocity histories measured during the tests were used to prescribe input motions at the corresponding base plate nodes. They compared computed and measured head velocity histories directly.

2.3.2 Operational drop tests

As non-traditional application of hard disk drives emerges, their mechanical robustness during the operating state is of greater concern. But there is relative little published work related to the experiments on drop test of operational HDDs.

One work by Harrison and Mundt [26] focused on the air bearing, which maintains the physical separation between magneto-resistive (MR) recording heads and disks. The suspension and slider were modeled as a lumped multiple degree-of-freedom (DOF) spring-mass system. The air bearing was modeled by the usual Reynolds equation, and it was solved by a numerical method. They measured the disk's

response at the point under the slider and the arm's response at the end of the arm. Then they used this measured data as input into the air bearing simulation code, and they obtained the dynamic fly height. In the experiment, an electromagnetic vibration exciter ("shaker") was used to apply 2 ms, half sinusoidal acceleration pulses to the disk drive under test, with peak amplitudes of 30 g, 60 g, and 90 g. The shaker was instrumented with an accelerometer in order to measure the amplitude and duration of the administered acceleration pulses. The disk and E-block arm motions were measured by using the laser Doppler vibrometry and used as inputs for the numerical solution of air bearing response. This complementary experimental and numerical study of fly height response to applied mechanical shock during disk drive operation showed that the effects of disk motion on fly height response were significant. Another consequence of this was that fly height response to operational shock was expected to be worse at the disk OD than at the disk ID. But it is inconvenient to apply their method because it required the measurement data for each case of interest. Furthermore, they didn't describe how to obtain the lumped spring-mass model of the arm-suspension, and they didn't show the effect of this simplification on the result. The result from simulation did not be verified by the experiment.

In the study by Glen Tunstall *et al* [27], resonance phenomenon was focused on when the HDD subjected to vibration. Operational drives have been vibrated over large frequency ranges in order to characterize their data-transfer performance and to ascertain which component is failing. In order to observe the cause of the problems, a drive has been modified with integral sensors to identify internal system failures and the results of these investigations were presented. These sensors have enabled the first unobtrusive tests of the drives' mechanical frequency response while the drive

was in operation with sensors. To measure the bending of the suspension arm, a thin (28 m) sheet of poly vinylidine flouride, PVdF, piezo material was bonded to the suspension arm to measure the average strain. This study presented unobtrusive tests of the operational HDD with integral sensors. But it is very difficult to avoid disturbing the system response when bonding these sensors on the small form factor HDD. On the other hand, the test rig can only produce low accelerations of up to 50 g.

Kuwajiama *et al* [28] reported a new actuator design incorporated with the balanced-type suspension for 0.85-in hard disk drive. Its performance on external shock resistance during read/write operations was investigated. Experimental drop impact test results confirmed that the 0.85-in drive equipped with the new suspension structure was durable over 2000G (1.0 ms duration) of external shock, ensuring no head slider and/or disk surface damage. According to computer simulation and experimental results, potential shock resistance of more than 2000 G may also be possible with the head actuator itself, which points to its application in cellular phones.

Zhao et al [29] used thermal asperity (TA) sensor to investigate head disk interface dynamics during operational shock. The output of TA sensor is a function of shock acceleration and back off level. The mechanisms and exciting sources of head-disk contact were explored by analyzing the TA sensor signal.

2.4 Numerical Simulations

Due to its complexity in structure, numerical modelling such as the finite element (FE) method and simplified models have been used in analysis of the drop dynamics of HAA/HDI and HDDs.

2.4.1 Dynamics of Head Actuator Assembly

Early finite element analyses in hard disk drives are mainly focused on the dynamic behaviour of the individual components such as suspension or arm [30]. Jeans [31] developed a FE model of the Type 4 suspension, and calculated the sensitivity of modal frequencies to design parameters of the load beam. The dynamic characteristics of various suspension designs have been studied by modal analysis and finite element modelling [32-35].

However, it is more important to analyse the entire HAA dynamic characteristics. Aruga, *et al* [36] established two finite element models of actuator without suspension and slider respectively. Jiang and Miles [37] built an HAA FE model in which the VCM was not included. Radwan, *et al* [38] presented an HAA FE model including VCM, suspension and slider. These finite element models have linearized spring constant of ball bearings.

A finite-element analysis of a Seagate Bali II disk drive actuator assembly was reported by Aristegui and Geers [40]. In this paper, two finite-element computer programs, MARC and LS-DYNA, were employed to perform static, modal and transient-response calculations. The preloaded state of the suspension was determined, and modeling verifications was secured through the comparison of calculated and measured nature frequencies and mode shapes. Shock-response calculations were performed for two dropping heights and two impacting surfaces. Their results showed that arm-assembly response was sensitive to drop height and surface stiffness. It was found that a detailed model of the head gimbal is required, as the slider often impacts

the disk at its edges. Finally, they found that the suspension itself was quite shock resistant.

Shi, *et al* [51] investigated dynamic properties of the head arm assembly (HAA) of a micro-drive using both experimental and numerical techniques. A finite element model for studying the dynamic property of the HAA was created and modified according to the experimental results. Good correlation between the experimental results and those by finite element simulation was achieved.

Some simplified models were also be used together with the FEM to study the dynamic characteristics of the HAA. Zeng *et al* [39] used a simplified beam model of the HAA together with the numerical simulations and experiments to propose a method for minimizing track seeking residual vibrations of the HDD. They found that the residual vibration of the HAA depends strongly on the waveform and the time duration of the driving impulse force.

Shi, *et al* [3-5] investigated the pulse shape effects in a shock analysis of an actuator arm of a hard disk drive by using the finite element method and its simplified model as an single degree of freedom system. The SDOF system was shown in Fig. 2.9. The equation of motion of the system was:

$$m\ddot{x}_2 + c(\dot{x}_2 - \dot{x}_1) + k(x_2 - x_1) = 0 \qquad (2.1)$$

The theoretical solution of the SDOF system subjected to single half-sine pulse loading is then derived by the Laplace transform and the inverse Laplace transform.

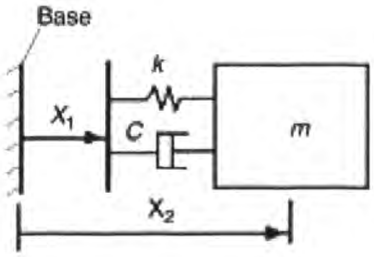

Fig. 2.9 A SDOF system of the actuator arm

Marek, *et al* [10] also reduced the problem to a single degree of freedom (DOF) model, neglecting disk motion while focusing on the cantilever mode of the suspension. The suspension was represented by a lumped parameter system characterized by an effective suspension mass (m), suspension stiffness (k), damping (c), and preload (gram) force (Fg). The equation of motion was:

$$m\ddot{x}_2 + c(\dot{x}_2 - \dot{x}_1) + k(x_2 - x_1) + F_g = 0 \tag{2.2}$$

In 2000, Sheng *et al* [49] developed a theoretical model to simulate the slider suspension during the unloading process. For simplification, the roll modes of the slider and suspension were ignored in their model. The load beam was modeled as a lumped parameter system that was characterized by an effective load beam mass and effective load beam stiffness. The effective stiffness was calculated by using the effective mass and the bending frequency of the load beam. Similar simplified were done to the slider.

2.4.2 Dynamics of Head Disk Interface

The preload acting at the slider stabilizes the sliding air bearing and prevents the slider lifting off and slapping on the disk surface to lead the failure of the head mode during operating state. There exists a vertical reaction between the head and the disk to support the HAA. The amplitude of the reaction is determined by the stiffness of the air bearing during the head did not touch the disk and the contact stiffness between the head and the disk while the head contacts the disk due to the HDD subject to a external shock or vibration. The stiffness between the head and the disk is a very important factor to determine the dynamic characteristics of the HAA and should be studied carefully to obtain the accuracy results of the HAA impact problem. It is a pity that very little literature studies the contributions of it to the HAA dynamic response under impact. However some researchers investigated the effects of the head-disk contact in load/unload process and damage of the disk induced by the head-disk contact stresses [45, 46].

Kumar *et al* [8] studied the mechanics at the hard disk interface caused by an input shock. Experimental results and a dynamic impact model were used to analyze the problem. The simplified model is shown in Fig. 2.10

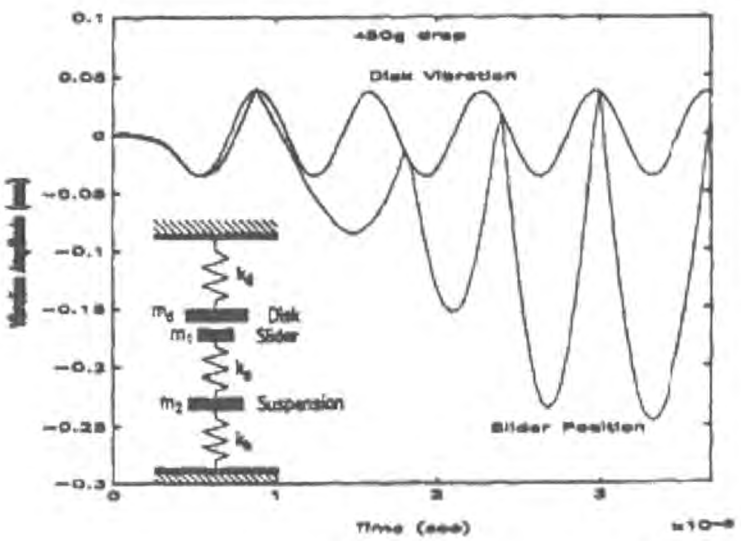

Fig. 2.10 Dynamic simulation of HDI mechanics [8]

The equations of motion of the system are summarized as

$$\ddot{x}_d + 2\varsigma_d \omega_d \dot{x}_d + \omega_d^2 x_d = (\frac{F_p}{m_d}) + A(t) \tag{2.3}$$

$$\begin{bmatrix} I_1 & 0 \\ 0 & I_2 \end{bmatrix} \begin{Bmatrix} \ddot{\theta}_1 \\ \ddot{\theta}_2 \end{Bmatrix} + \begin{bmatrix} b_{11} & b_{12} \\ b_{21} & b_{22} \end{bmatrix} \begin{Bmatrix} \dot{\theta}_1 \\ \dot{\theta}_2 \end{Bmatrix} + \begin{bmatrix} k_{\theta_1} + k_{\theta_2} & -k_{\theta_2} \\ -k_{\theta_2} & k_{\theta_2} \end{bmatrix} \begin{Bmatrix} \theta_1 \\ \theta_2 \end{Bmatrix} = \begin{Bmatrix} T_1 \\ T_2 \end{Bmatrix} \tag{2.4}$$

$$\begin{Bmatrix} x_l \\ x_s \end{Bmatrix} = \begin{bmatrix} L_{e_1} & 0 \\ L_{e_1} & L_{e_2} \end{bmatrix} \begin{Bmatrix} \theta_1 \\ \theta_2 \end{Bmatrix} \tag{2.5}$$

$$\begin{Bmatrix} T_1 \\ T_2 \end{Bmatrix} = \begin{bmatrix} L_{e_1} & 0 \\ 0 & L_{e_2} \end{bmatrix} \begin{Bmatrix} m_{e_1} A(t) \\ m_{e_1} A(t) - F_p \end{Bmatrix} \tag{2.6}$$

On impact:

$$x_s^+ - x_d^+ = v(x_s^- - x_d^-), \quad x_d^+ = x_d^- \tag{2.7}$$

where, x_d is disk position, ω_d is disk umbrella mode frequency, ς_d is disk damping, F_p is preload, $A(t)$ is input acceleration, x_s is slider position, I_1, I_2 are HSA moment of inertia, L_{e_1}, L_{e_2} are load beam lengths, b_{ij} is HSA damping, T_1, T_2 are torques on HSA, x_l is load beam position, θ_1 is hinge angle, θ_2 is load beam angle, k_{θ_1} is hinge stiffness, k_{θ_2} is load beam stiffness, m_{e_1} is load beam root mass, m_{e_2} is load beam tip mass, -/+ indicate before/after impact, v is coefficient of restitution

This model showed excellent agreement with the experimental data. However, This model can only predict gross motions of the slider and the air bearing between the slider and disk was not considered.

Kouhei *et al* [15] estimated the stress in the disk from the slider collision by using Hertz's contact stress with energy conservation. The energy dissipation was ignored during deformation. The maximum shearing stress of the disk was described by

$$\frac{1}{2}mv^2 = \int f(\delta)d\delta \tag{2.8}$$

$$\tau_{\max} = cE'^{4/5}R^{-3/5}v^{2/5}m^{1/5} \tag{2.9}$$

where, m : mass of slider

v : relative velocity between slider and disk

$f(\delta)$: reaction force

δ : deformation depth

τ : shearing stress

E' : combined Young's modulus

R : radius of slider's edge

c : constant

The pressure distribution exerted by the air bearing on the slider surface is governed by gas lubrication equation (compressible Reynolds equation) shown as

$$\frac{\partial}{\partial x}\left(ph^3Q\frac{\partial p}{\partial x}\right)+\frac{\partial}{\partial y}\left(ph^3Q\frac{\partial p}{\partial y}\right)=6\mu U\frac{\partial}{\partial x}(ph)+6\mu V\frac{\partial}{\partial y}(ph)+12\mu\frac{\partial}{\partial t}(ph) \tag{2.10}$$

where, p is pressure acting on slider surface

h is spacing between disk and slider

μ is dynamic viscosity

U and V are local disk velocity in the x and y direction

Jayson, *et al* [2, 50] developed a finite element model of an HDD to investigate the transient response of an operational HDD subject to shock and vibration. In their model, the air bearing stiffness of the head disk interface was determined from a finite element solution of the Reynolds equation and approximated with linear springs. However, the air bearing stiffness is nonlinear when the flying height of the slider is

high. Therefore, the air bearing should be modeled as nonlinear spring in the numerical simulation.

The action of the air bearing throughout contact was simulated as a set of four identical translational springs placed on the center lines of the two slider rails and one quarter of the untapered slider length away from the untapered ends by Leo and Sinclari [47] to estimate how hard did a head hit a disk. Sheng, *et al* [48] proposed a theoretical model of one-degree-of-freedom-system for the head-disk contact vibration study, and gave out a bilinear model of the system restoring force.

The shock responses of a disk-suspension-slider air bearing system were studied by Zeng and Bogy [6], they found that the air bearing had different responses of upwards and downward shocks and the slider-asperity contacts occurred when a strong shock is applied.

The ramp LUL technology has proved to be a historic breakthrough because of the advantages of increasing the disk storage areal density, greater durability, more efficient power utilization and superior non-operational shock resistance. The dynamic characteristics of head/disk interface and lift-tab/ramp interface in hard disk drives subject to an external shock were modeled by Ao et al [52]. Dynamic performance of the suspension slider and its status during loading and unloading process was studied.

Rai and Bogy [53] proposed a method in which both the structural components including the disk, ramp, suspension and the air bearing were modeled in detail and were coupled with each other. However, the ramp was modeled as a rigid body that

was fixed. Li and Bogy [54] developed a reduced model of a deformable ramp and implemented it into a multi-body operational shock (op-shock) model. Numerical analyses using three different ramp models (no-ramp, rigid ramp and deformable ramp) were carried out to study the HDD's failure dependence on the different ramp models.

2.4.3 Dynamics of HDD

Edwards [41] attempted to evaluate the HDD system as a whole, his finite element model in ANSYS includes models of the HDD enclosure base and cover, the HAA, the disk pack/spindle motor assembly and the voice coil motor assemble (VCM). He studied the shock response of a hard disk drive dropped from a height onto a surface with a specific contact stiffness. In each simulation the HDD model was dropped from a 25.4 mm height, but the contact stiffness of the impact surface was varied for each simulation. His simulations demonstrated the effect the surface stiffness characteristics have on both the magnitude and the pulse width of the impact shock received by the HDD and the dramatic changes in the response of the internal components of the HDD to these different shocks. His study also showed that the acceleration amplification factors experienced by key components can be many times the values expected of single DOF systems due to the combined effect of multiple modes of vibration and that in particular the head stack assembly will experience the highest acceleration amplifications when subjected to shock with pulse widths in the 0.5 to 1.0 ms range due to the frequencies of the modes of vibration excited in this assembly. This sensitivity of the HAA to short duration shocks is a key factor in the resultant head-disk interface response leading to head-disk separation and subsequent

head slaps. His experimental results showed good agreement to the analytical results that the frequencies of the modes of vibration excited in the diskpack/spindle motor and the HAA as well as with respect to their acceleration amplification factors.

In Lin's work [42], the finite element studies of HDD under a non-operational were presented. A complete finite element HDD model was built in ANSYS package. Shock pulses with different amplitude and pulse width were applied to the HDD. Transient analysis was performed to calculate the deflections of the nodes at critical locations during and after the shock. The minimum shock amplitude required to lift off the head from the disk was determined for different shock pulse width. The effects of drive base stiffness, disk thickness, actuator arm stiffness, and bearing stiffness on HDD shock performance were investigated.

A finite element model of a hard disk drive was developed by Jayson, *et al* [43] to investigate the response of the HDD to a shock impulse. Two types of shock were of interest in their model, a linear shock and a rotary shock. The linear model corresponds to an HDD being dropped flat onto an impact surface. The rotary model was constrained to rotate about an axis and simulated an HDD standing on one edge that was allowed to drop and impacted the opposite edge. The transient solution was performed using a finite element solver (LS-DYNA). Comparison of the simulation results for the two models was used to develop a correlation between the linear and rotary shock tests.

Jang, *et al* [55] presented a method for analyzing the free vibration of a spinning flexible disk-spindle system in a HDD considering the flexibility of complicated

supporting structure by using FEM and substructure synthesis. Finite element equations of each component of a HDD spindle system from the spinning flexible disk to the flexible base plate were consistently derived by satisfying the geometric compatibility in the internal boundary between each component. The rigid link constraints were also imposed at the interface area between the shaft and supporting structure to describe the physical motion at this interface. A global matrix equation obtained by assembling the finite element equations of each substructure was transformed to a state-space matrix-vector equation, and the associated eigen-value problem was solved. The validity of this research was verified by comparing the numerical results of the natural frequencies and mode shapes with the experimental ones. This research shows that the supporting structure which includes the stator, housing and base plate plays an important role in determining the natural frequencies and mode shapes of a HDD spindle system.

In another research by Jang, *et al* [56], a finite element method to analyze the free vibration of a flexible HDD composed of the spinning disk–spindle system with fluid dynamic bearings (FDBs), the head– suspension–actuator with pivot bearings, and the base plate with complicated geometry was presented. The spinning disk, hub and FDBs were modeled by annular sector elements, beam elements and stiffness and damping elements, respectively. It developed a 2-D quadrilateral 4-node shell element with rotational degrees of freedom to model the thin suspension efficiently as well as to satisfy the geometric compatibility between the 3-D tetrahedral element and the 2-D shell element. The base plate, the arm, the E-block and the fantail were modeled by tetrahedral elements. Pivot bearing of an actuator and air bearing between spinning disk and head were modeled by stiffness elements.

Finite element analysis is often used to investigate the shock problem. However, this method consumes a great amount of time and is difficult to perform design parameter studies. Gao, *et al* [44] presented a flexible multi-body dynamics formulation to analyze the shock problem of non-operating HDDs. By introducing constraint equations between the slider and the disk surface, the shock response of the whole HDD system has been obtained. Numerical results showed that the method is reasonable and the acceleration amplitude which makes the slider lift off can be determined in a significantly shorter time than by the conventional approach. Finally, the effect of drive parameters on shock resistance, such as shock duration and slider resting location were analyzed. Liu, *et al* [57] developed this flexible multi-body dynamics formulation by taking into account nonlinearity and discontinuity caused by the contact between the dimple and flexure. The air bearing force was obtained by solving the Reynolds equation using the finite volume method and considering Intermolecular force.

Notes:
① www.pcguide.com

CHAPTER 3

BASIC PRINCIPLES FOR THE DROP TEST OF HDDS

3.1 Introduction

The basic principles for the drop test of HDDs will be summarized in this chapter. The mechanical loadings applied to HDDs can be classified into shock and vibration. Vibration loadings can excite natural frequencies in components of the head/disk interface. Shock is the mainly concerned loading in the drop test of HDDs. In section 3.2, two typical shock models — linear drop test and rotary drop test will be expatiated. The finite element method (FEM) including the four modeling stages and the FEM algorithm of LS-DYNA will be reviewed in section 3.3.

3.2 Linear and Rotary Drop Test

Shock is an important consideration in drives during manufacturing, shipping and operation. Shock is most relevant to applications in portable computers and other mobile products with an HDD. Desktop computers also need to withstand shock due to shipping and mishandling. Dropping, striking or bouncing a drive against a hard surface can damage it internally with no external evidence of damage. A drive that is subjected to this type of shock may fail on initial use. Or, the damage could simply cause the reliability of the drive to degrade over time. When an HDD is subjected to a high level of acceleration shock, the head suspension system lifts off the disk and lands on it in a very short time, and the impact during this slap often leads to failure of

the magnetic head and disk.

The previously recognized industry shock specifications (half-sine pulse acceleration profiles of 100 to 300g amplitudes and 2 millisecond in duration) have proven to be insufficient for the identification of the mechanisms that cause damage to the components of small portable drives. Currently new standards are being developed to adequately test and evaluate the roughness of portable drives and their components. These new standards include higher shock amplitudes of 500-1000 g and shorter durations of 0.5 to 2 ms.

Shock is relevant in both operational and non-operational drives states. Linear drop test and rotary drop test are two typical shock models. A linear drop test, as shown in Fig. 3.1, can be simulated by giving the HDD an initial velocity corresponding to a particular drop height. A rotary drop test, as shown in Fig. 3.2, can be simulated by giving the HDD an initial angular velocity corresponding to a particular drop angle. The drop angle is the angle between the base-plate and the impact surface at the moment the HDD is dropped.

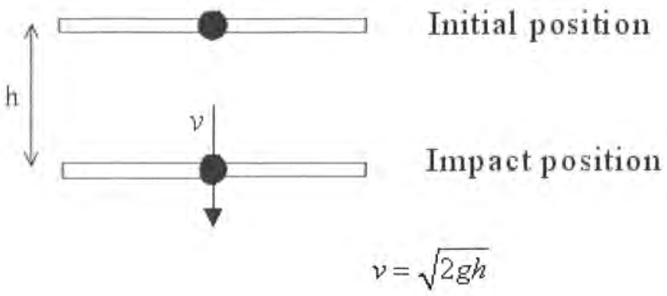

Fig. 3.1 A linear drop simulation

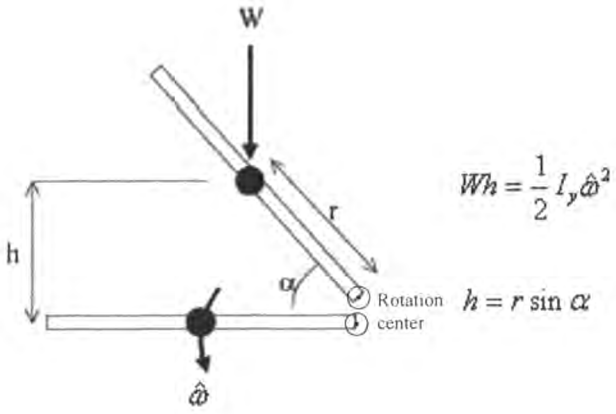

Fig. 3.2 A tilt drop simulation

In the linear drop test the drop height and initial velocity are related using eq. (3.1),

$$v = \sqrt{2gh} \tag{3.1}$$

where, v is the velocity,

g is the acceleration of gravity,

h is the drop height.

The initial velocity is applied to each HDD component and the impact surface is constrained in all degrees of freedom.

In the rotary drop test the initial angular velocity is related to the drop angle using a conservation of energy approach shown in eq. (3.2),

$$Wh = \frac{1}{2} I_y \hat{\omega}^2 \tag{3.2}$$

where, W is the weight of the disk drive,

h is the distance from the HDD center of gravity to the impact surface,

I_y is the moment of inertia about the axis of rotation,

$\hat{\omega}$ is the angular velocity of the drive at impact.

The potential energy prior to release is equal to the kinetic energy at impact as demonstrated in Fig. 3.2. Thus we observe the drop angle α is related to the height of the HDD center of gravity prior to release by eq. (3.3).

$$h = r\sin\alpha \tag{3.3}$$

3.3 Finite Element Method

3.3.1 Four Modeling Stages

The finite element modeling of HDD structure usually consists of four stages:

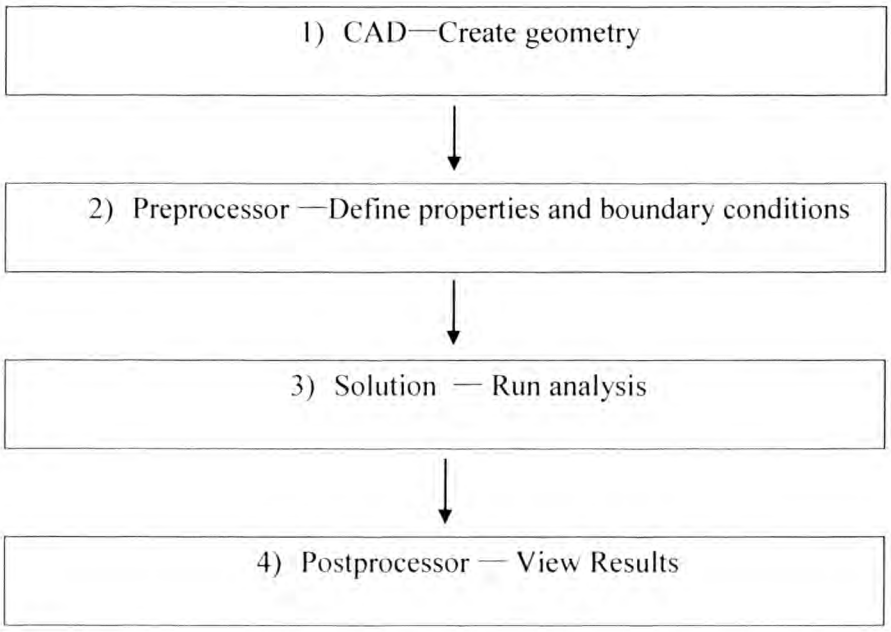

In the first stage, the geometry of HDD can be created using CAD modeling packages

such as Ideas, AutoCAD, HyperMesh and ProE etc. The geometry of HDD should make some simplifications and the connections between components are neglected at this stage. The geometry is usually exported in a form containing information about the points, the lines and the surfaces in the model.

The model created in the first stage can be imported to pre- and/or post-processor such as ANSYS and Hypermesh *et al* which are compatible with many finite element solvers. The geometry can be meshed, creating the nodes and elements for each component. Once meshed, the components can be connected using coupling, spotwelds and/or rigid links. The boundary conditions and initial conditions can be defined in the second stage.

In the last two stages, numerical simulation results can be obtained by the finite element software, ANSYS/LS-DYNA. The simulation results can then be processed/viewed by data-processing functions of ANSYS/LS-DYNA, Matlab and/or Excel etc.

3.3.2 FEM Algorithm of LS-DYNA

A Lagrangian formulation is considered, thus the time-dependent deformation can be expressed in terms of the convected coordinates X_α and the time t as shown in eq. (3.4).

$$x_i = x_i\left(X_\alpha, t\right) \tag{3.4}$$

The governing equation to be solved is the Cauchy momentum equation shown in eq. (3.5).

$$\sigma_{ij,j} + \rho b_i = \rho \ddot{x} \tag{3.5}$$

where, σ_{ij} is the Cauchy stress,

ρ is the density,

b_i is the body force ,

$\ddot{x}$ is the acceleration.

Equation (3.5) must satisfy the traction boundary conditions and displacement boundary conditions shown in eqs. (3.6) and (3.7), respectively.

$$\sigma_{ij} n_i = T_i(t) \tag{3.6}$$

$$x_i(X_\alpha, t) = D_i(t) \tag{3.7}$$

where, n_i is the outward normal to the body,

T_i is the traction on the body,

D_i is the defined displacement.

Manipulating the momentum equation and the boundary conditions we can develop the weak form of the equilibrium equations as shown in eq. (3.8). This equation is also known as the principle of virtual work.

$$\int_V \rho \ddot{x}_i \delta x_i dv + \int_V \sigma_{ij} \delta x_{i,j} dv - \int_V \rho b_i \delta x_i dv - \int_S l_i \delta x_i ds = 0 \tag{3.8}$$

where, V denotes a volume integral,

s denotes a surface integral.

We superimpose a mesh of the finite elements and connecting nodes over the body as stated in eq. (3.9).

$$x_i(X_\alpha, t) = x_i(X_\alpha(\xi, \eta, \zeta), t) = \sum_{j=1}^{n} \phi_j(\xi, \eta, \zeta) x_i^j(t) \tag{3.9}$$

where, ϕ_j are the shape functions of the parametric coordinates (ξ, η, ζ),

n is the number of nodes defining the element,

x_i^j is the displacement of the jth node in the ith direction.

Summing over n elements one may write eq. (3.10).

$$\sum_{m=1}^{n}\left\{\int_{v_m}\rho\ddot{x}_i\Phi_i^m dv+\int_{v_m}\sigma_{ijij}^m\Phi_{i,j}^m dv-\int_{v_m}\rho b_i\Phi_i^m dv-\int_{s_m}l_i\Phi_i^m ds\right\}=0 \tag{3.10}$$

where,

$$\Phi_i^m=\left(\phi_1,\phi_2,\cdots,\phi_k\right)_i^m \tag{3.11}$$

In matrix notation eq. (3.10) leads to the relationship shown in eq. (3.12). The dynamic finite element solver can be used to carry out the simulation.

$$\sum_{m=1}^{n}\left\{\int_{v_m}\rho N^T N a dv+\int_{v_m}B^T\sigma dv-\int_{v_m}\rho N^T b dv-\int_{s_m}N^T l ds\right\}=0 \tag{3.12}$$

where, N is an interpolation matrix,

σ is the stress vector,

B is the strain-displacement matrix,

a is the nodal acceleration,

b is the body force load vector,

l is the applied traction loads.

Eq. (3.12) can be written in matrix form as eq. (3.13)

$$M\ddot{x}(t)+F(x,\dot{x})-P(x,t)=0 \tag{3.13}$$

where, M is the structural mass matrix, formed of element lump mass matrices,

$\ddot{x}(t)$ is the nodal acceleration vector,

$\dot{x}$ is the nodal velocity vector,

P is the load vector of the structure, composed of the nodal loads, surface loads and body loads,

F is constituted of equivalent nodal force vector.

The hourglass viscous damping force H must be introduced for the use of one-point GAUSS integration method. Considering damping and force H, we can obtain

$$M\ddot{x}(t) = P - F - C\dot{x} + H \tag{3.14}$$

To solve this equation, the explicit central difference method is used. The main Equations are as following

$$\ddot{x}(t_n) = M^{-1}[P(t_n) - F(t_n) + H(t_n) - c\dot{x}(t_{n-\frac{1}{2}})] \tag{3.15}$$

$$\dot{x}(t_{n+\frac{1}{2}}) = \dot{x}(t_{n-\frac{1}{2}}) + \frac{1}{2}(\Delta t_{n-1} + \Delta t_n)\ddot{x}(t_n) \tag{3.16}$$

$$x(t_{n+1}) = x(t_n) + \Delta t_n \dot{x}(t_{n+\frac{1}{2}}) \tag{3.17}$$

$$t_{n-\frac{1}{2}} = \frac{1}{2}(t_n + t_{n-1}) \tag{3.18}$$

$$t_{n+\frac{1}{2}} = \frac{1}{2}(t_{n+1} + t_n) \tag{3.19}$$

$$\Delta t_{n-1} = (t_n - t_{n-1}) \tag{3.20}$$

$$\Delta t_n = (t_{n+1} - t_n) \tag{3.21}$$

Eq. (3.15) to (3.21) are uncoupled for the use of lump mass matrix. So the structural mass matrix needs not to be formed. However, some conditions must be satisfied to ensure the central difference method is stable. In LS-DYNA program, the time step size at any time is controlled by the stability of current time. After calculation the critical time step size of every current element, that is the maximal time step size which is stable in explicit central difference method, the program will choose the minimum of them to calculate the next time step.

CHAPTER 4

NUMERICAL ANALYSIS OF THE SHOCK RESPONSE OF HARD DISK DRIVES

4.1 Introduction

Areal density of hard disk drives (HDDs) has been increasing steadily in the last decade. Highly stable head-disk interface at ultra-low flying height has been required to meet the challenge of high-density magnetic recording technology towards multi terabit per square inch areal densities [58], [59]. As the flying height of the head/disk interface has been reduced to the sub-10 nm flying height regime, the mechanical robustness of HDDs under shock during operational states is of a greater concern. One approach for dealing with the shock problems is to design a robust mechanical system and slider/disk interface. One important damage mode of the HDD is the "head slap" behavior and should be strictly avoided.

There have been several groups working on the experimental and numerical simulation on shock response of the mechanical system and its effects on the head-disk interface. Many of these studies were focused on the numerical and theoretical aspects of the problem [60]-[64]. Bhargava and Bogy investigated the dynamic response of small form factor hard disk drives and found that a disk system is more robust to downward shock than upward shock [60]. Murthy et al. investigated the shock performance of two form factor HDDs, 3.5 and 2.5 in, respectively [61]. The displacement of the actuator arm, the suspension, and the disk due to linear shock loads was studied experimentally for both non-operating and operating states of the

HDDs. Shu et al. performed a drop test simulation of a head actuator assembly subjected to half-sine acceleration pulses. A pseudo-resonance phenomenon was observed and investigated by finite element simulation and a single-degree-of-freedom (SDOF) model [62]. Liu et al. found that softer material can be used at the dimple-flexure position to increase the shock tolerance of HDD [63]. Shi et al. conducted operational shock simulation with a finite-element model, and investigated the pulse width effect of a half sine shock pulse on the shock response [64]. But the air bearing was modeled with linear springs, which were not able to capture the true behavior of the air bearing.

In this chapter, a numerical analysis is conducted here to investigate the real boundary condition and the shock response for the disk of S1 drive by using the finite element method. The effects of disk clamping conditions and shock pulse amplitude and width on the operational shock response of the head disk assembly (HDA) are further investigated. The non-operational linear and rotary drop tests of the whole hard disk drive (HDD) are also simulated.

4.2 Numerical Analysis on The Influnce of The Clamping Condition of The Disk

4.2.1 Introduction

Head slap happens between sliders and the disk due to the severe shock. The vibration of the disk during the shock has a great influence on the head slap. In the previous works by Luo *et al* [65], the influence of the boundary condition of the disk on the

head slap was studied. It was found that when the disk is more tightly clamped, it's more difficult for the head slap to take place. Only two simplified boundary conditions, i.e., simply supported and clamped for the non-operational drive were considered in their study. However, the discussion in section 4.2.2 shows that the real boundary condition of the disk is neither simply supported nor clamped. In order to improve the shock resistance of the disk and to avoid the head slap, the real boundary condition for the disk of S1 drive is investigated further here.

Although an extensive literature exists on the vibration of thin , circular disks [66-74], the boundary condition of the disks in these works was just simplified as being clamped in the clamping region and free at the outer edge. Such simplification of the boundary condition is rather reasonable for the clamping condition of the disks being studied before. Because in the hard disk drive, the disk is usually sandwiched between a thick annular clamping ring and a mating annular clamping ring, and the assembly is firmly bolted together as shown in Fig. 4.1. The thick clamping rings and bolts can be assumed rigid and the disk is unable to deform in the clamping region. Therefore, the disk can be seen as being clamped in the clamping region.

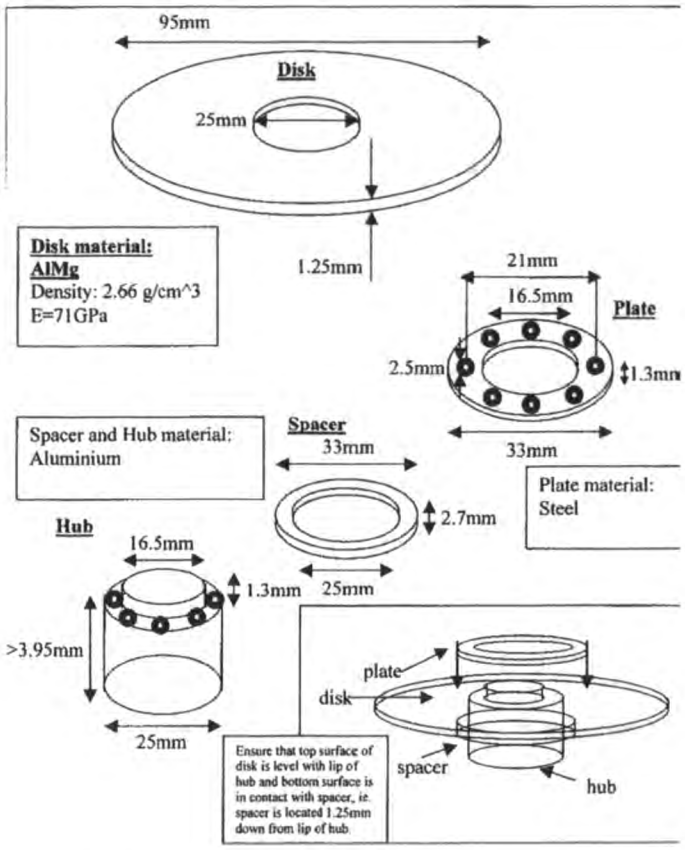

Fig. 4.1 Disk clamped in the clamping region [27]

For the small form factor hard disk drive, S1, a one-screw-clamp is designed to clamp the disk as shown in Fig. 4.2. The clamp and the hub are firmly bolted together by the screw at the center of the clamp and hub. When the screw is tightened to produce the clamping force, the clamp compresses appreciably and presses the disk on the hub tightly. This one-screw-clamp design makes the boundary condition of the disk more complex than that of the disk in Fig. 4.1.

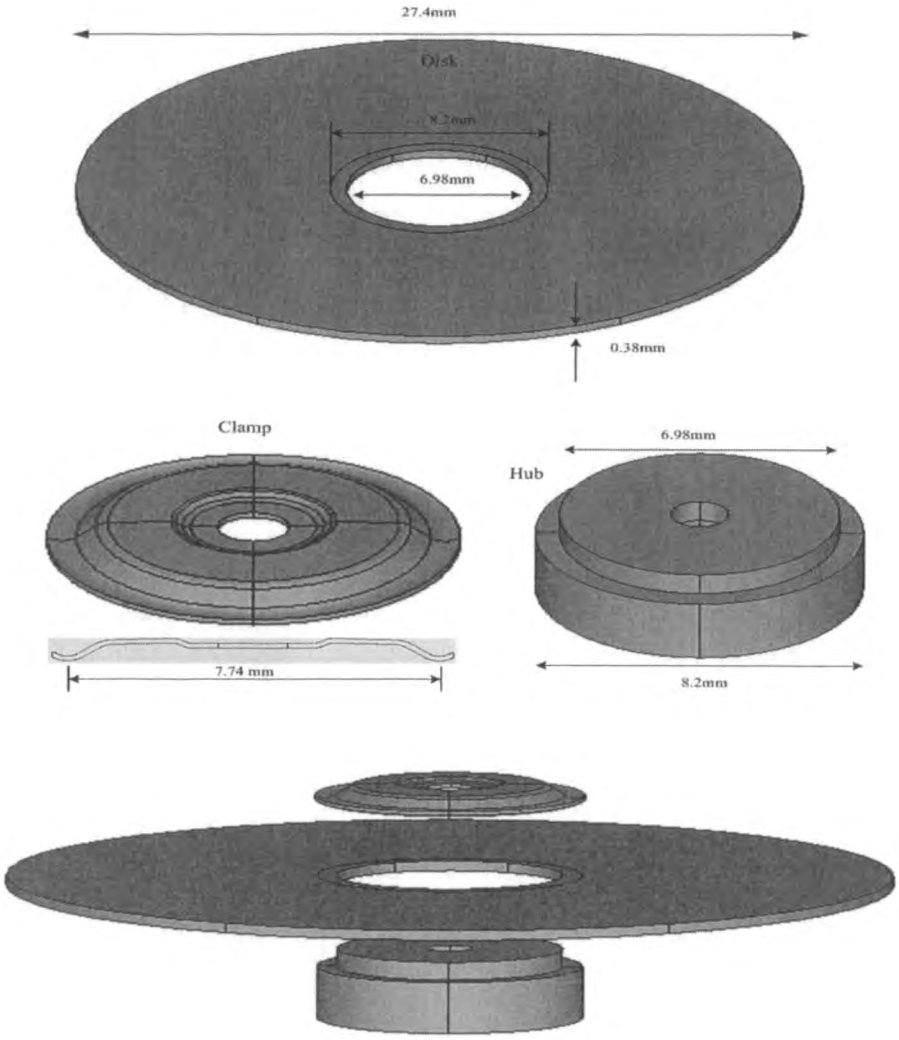

Fig. 4.2 Clamping design of S1 disk

A numerical analysis is conducted here to investigate the real boundary condition and the shock response for the disk of S1 drive by using the finite element method. The real boundary condition of the disk is assumed to be axisymmetric in this work.

4.2.2 Linear Analysis with Simplified FE Models

Firstly, we study the boundary conditon of the disk with simplified FE models. The disk is assumed to be constrained with a proper boundary condition on an annular area

at the center. The geometry of the disk is illustrated in Fig. 4.3. The material property of the disk is given in Table 4.1.

Table 4.1 Material properties of the disk

Young's modulus	density	Poisson's ratio	Thickness
83.5Gpa	2.55e-6kg/mm^3	0.33	0.38mm

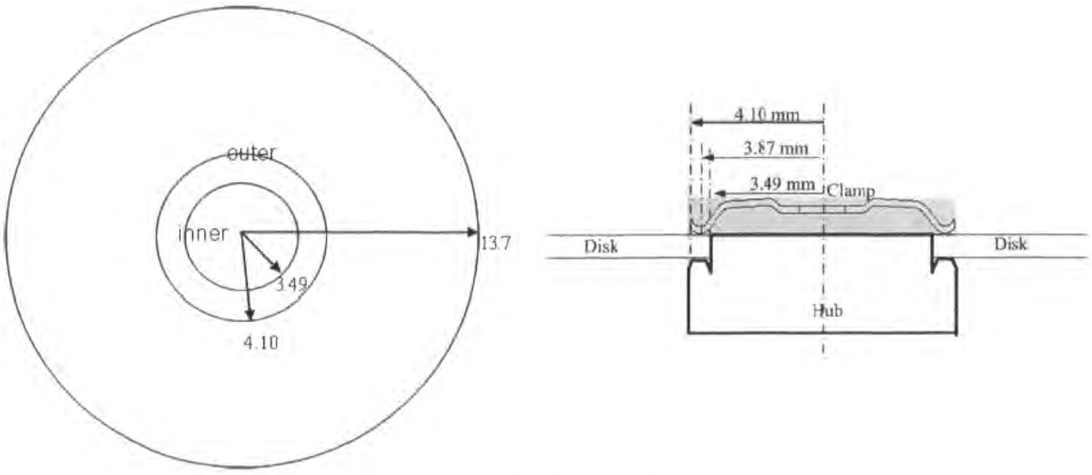

Fig. 4.3 Geometry of the disk

The disk is meshed with shell elements. Here we define the simply supported and clamped boundary condition as: simply supported boundary condition means only the translational degrees of freedom are constrained; clamped boundary condition means all the degrees of freedom are constrained. The following boundary conditions are studied:

B1: outer circle simply supported

B2: inner and outer circle simply supported

B3: outer circle clamped

B4: the eighth annual strip area from the inner circle simply supported after the annual area between inner and outer circle was meshed into 21 annual strips with more elements

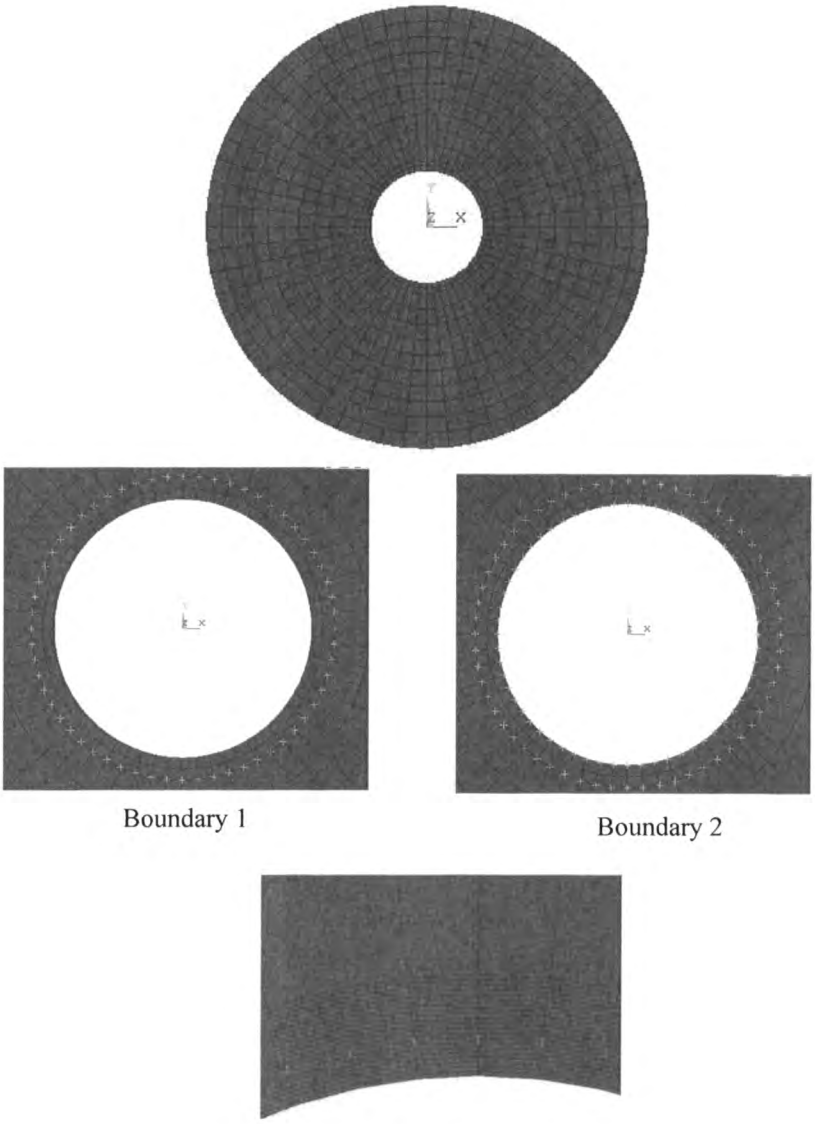

Fig. 4.4 Simplified boundary conditions of the disk

4.2.2.1 Modal Analysis

It is well known that a disk has three types of modes in vibration. The first type is the symmetric modes with m nodal circles and no nodal diameters, i.e., (m, 0). These

modes are also referred to as the 'umbrella' modes of vibration (Fig. 4.5a). The second type is the asymmetric modes with zero nodal circles and n nodal diameters i.e., (0, n) (Fig. 4.5b). These modes have no response to symmetric excitations. The third type is the coupled asymmetric modes i.e., (m, n) (m>0, n>0) (Fig. 4.5c), which are higher frequency modes, and their responses are much smaller than the responses from the low frequency modes for ordinary shocks (e.g., 1 ms half-sine acceleration pulse).

Table 4.2 Modal analysis results of the disk

Boundary conditions	(0,0) Mode /Hz	(0,1) Mode /Hz	(0,2) Mode /Hz
B1	2080	2206	3657
B2	3604	3505	4259
B3	3790	3710	4437
B4	2908	2753	3705
Experiment [75]	2913	2469	3950

Table 4.2 shows the modal analysis results of the disk modeled by shell elements with different simplified boundary conditions. As a comparison, the corresponding experimental results by Hendri [75] are also listed in this table. Comparison between the numerical results and the experimental results shows that the real boundary condition of S1 disk is between B1 and B2. The results from B4 match the experimental results best, especially for the (0, 0) umbrella mode shape, which dominates the shock response according to the discussion in section 4.2.2. Therefore, B4 can be approximated as the real boundary condition of the disk initially.

a) Umbrella mode

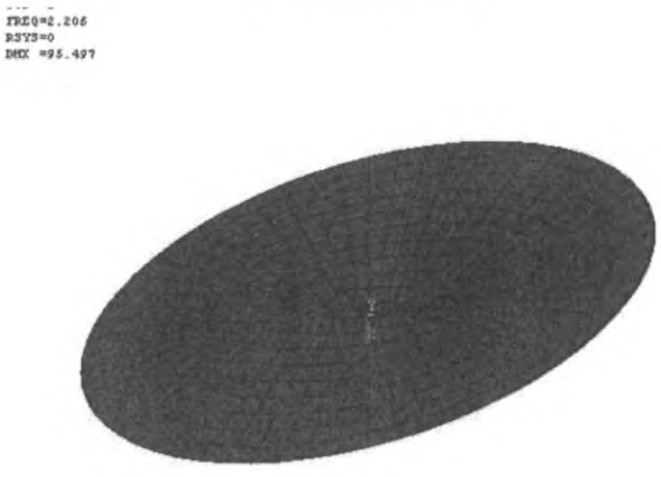

b) Radial mode

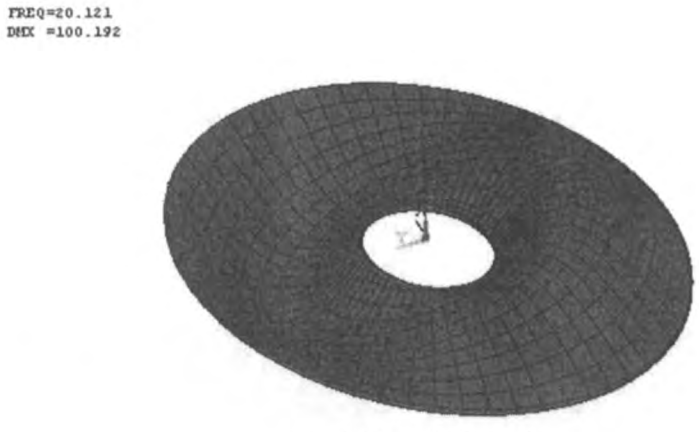

c) Coupled mode

Fig. 4.5 Modes of vibration of the disk: Umbrella mode, radial mode, coupled mode

4.2.2.2 Shock Response

The shock response of the disk with simplified boundary conditons and corresponding loading conditions are computated. Shock is modeled as a Z-direction half sine

acceleration pulse to the FE model as shown in Fig. 4.6. The pulse width is 1 ms and the applitude of the shock pulse is 400 g.

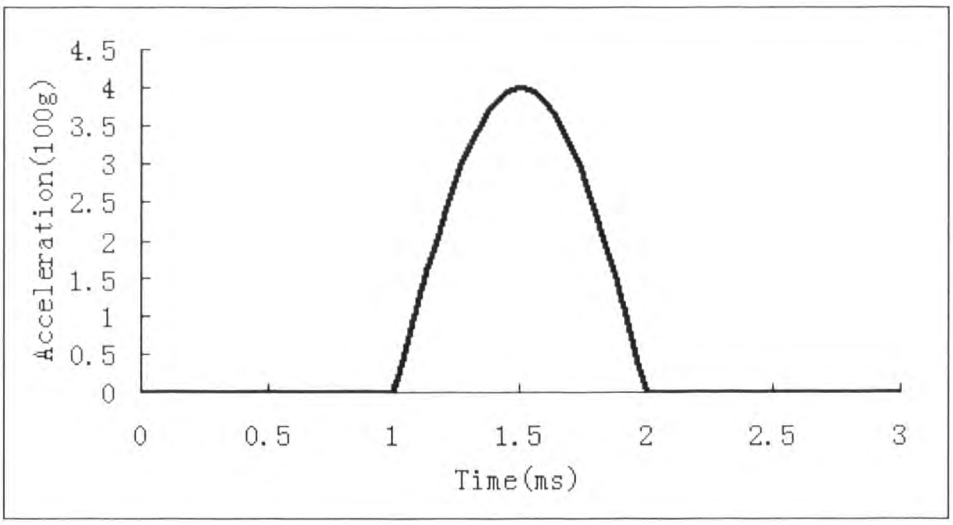

Fig. 4.6 The shock pulse of 400g with 1 ms

For the boundary condition B1, the shock pulse is applied on the nodes of outer circle of the clamping area. For the boundary condition B2, the shock pulse is applied on the nodes of outer circle and inner circle. For the boundary condition B3, the shock pulse is applied on the nodes of outer circle and these nodes' rotational degree of freedom are all constrained. For the boundary condition B4, the shock pulse is applied on a small area between inner and outer circle. Fig. 4.7 and Fig. 4.8 show the loading conditions of B1 and B2, respectively.

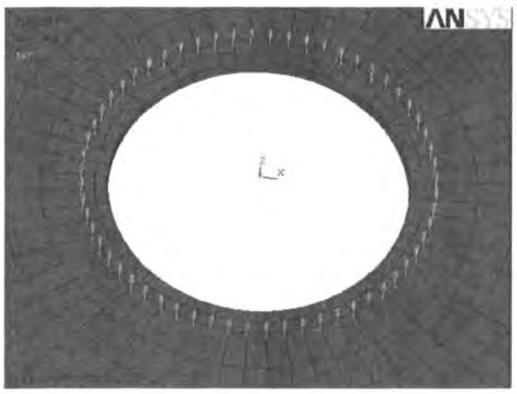

Fig. 4.7 Load condition of B1

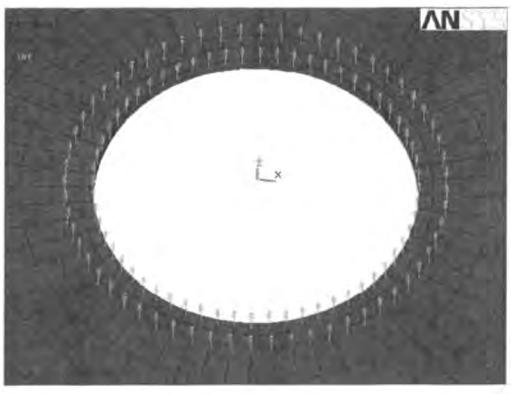

Fig. 4.8 Load condition of B2

Fig. 4.9 shows the relative Z-displacement of the disk at the outer edge to the Z-displacement of the nodes where the acceleration pulse is applied. The boundary conditon B1 with corresponding load condition shows the greatest shock response. The boundary condition B3 with corresponding load condition has the lowest relative Z-displacement and can be seen as the perfect clamping condition. The shock response of boundary conditon B2 with corresponding load condition is a little higher than the perfect clamping condition. The shock response of boundary conditon B4 with corresponding load condition is between B1 and B2 and is supposed to be close to the shock response of the disk with real boundary condition and corresponding load condition.

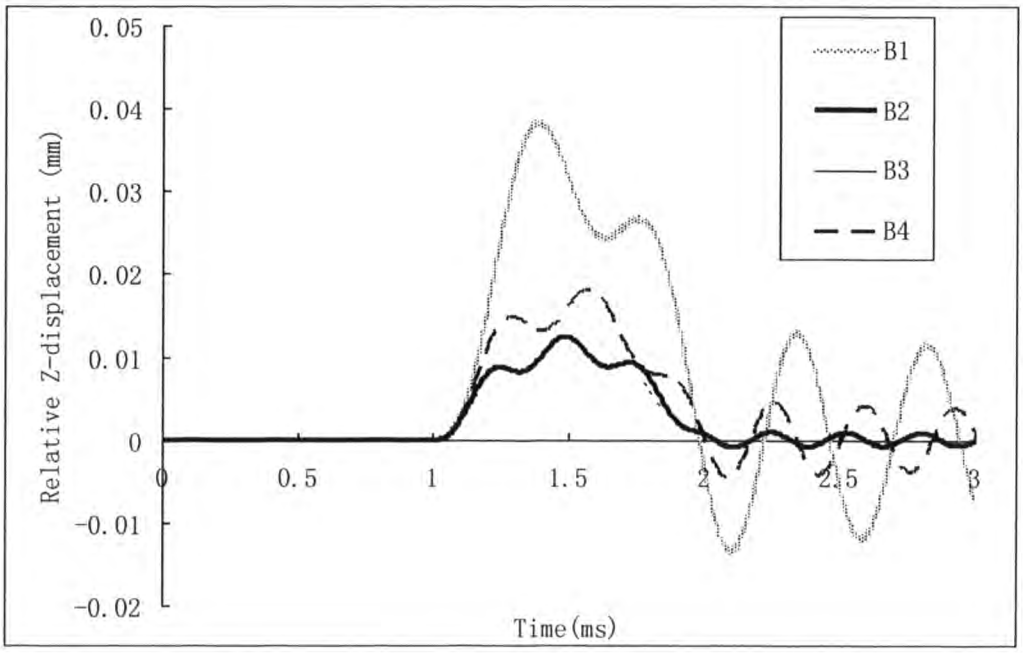

Fig. 4.9 Shock response of disk under different load conditions

A power spectrum analysis is performed on the shock response of the disk. Fig. 4.10 shows the response spectra of the shock response of the disk with boundary conditions B1, B2, B3 and B4. In each curve, the obvious peak is observed. The peaks correspond to the (0, 0) umbrella mode of vibration of the disk for each boundary

conditions. For example, B1 has the peak around 2 kHz, which close to its frequency of (0, 0) mode, 2080 Hz in Table 4.2. B4 has the peak around 3 kHz, which close to its frequency of (0, 0) mode, 2908 Hz in Table 4.2. The other small peak corresponds to radial modes of vibratons of the disk, but the related power is relatively small. Thus we can see that the disk response is dominated by the umbrella mode when the shock is applied axisymmetrically.

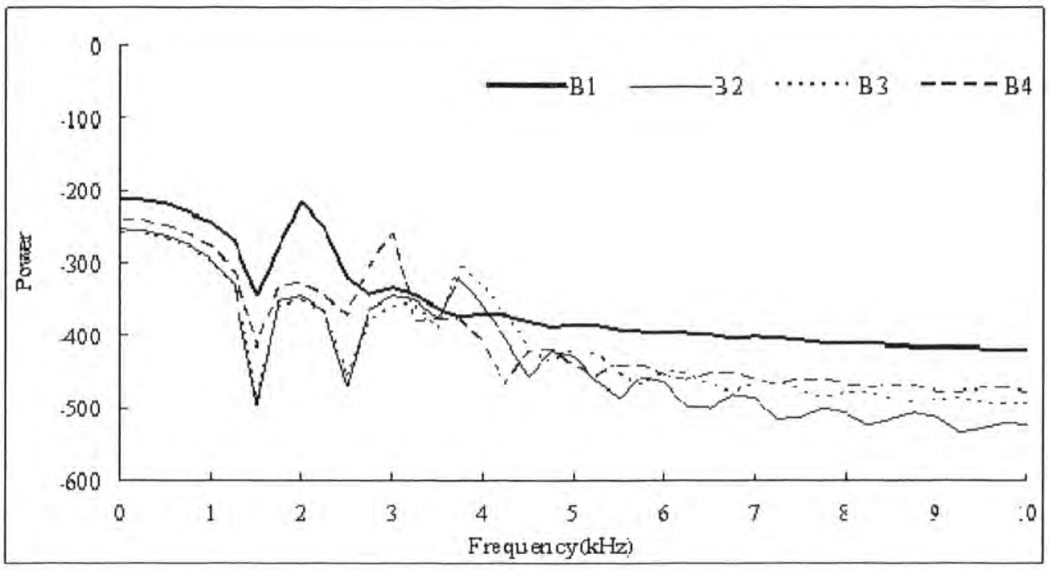

Fig. 4.10 Power spectra of the shock response of the disk

4.2.2.3 Transverse Stiffness of the Disk as an Index

Here we define the transverse stiffness of the disk from the solution of the static-state deflection of the disk under a uniformly distributed unit load along its outer edge. The total load F=1 N. The length of the outer edge is L. So the distribution of the load along the edge will be 1/L (N/mm). If the deflection of the outer edge is w, we define the transverse stiffness of the disk as

$$K_t = 1/w \tag{4.1}$$

There are totally 72 nodes along the outer edge of the disk in the finite element model shown in Fig. 4.4. The deflection of the outer edge is caculated when an axisymmetric load of 0.0139 N is applied at any node of the outer edge of the disk. Table 4.3 shows the transverse stiffness of the disk under simplified boundary conditions.

Table 4.3 Transverse stiffness of the disk

Boundary conditions	Transverse stiffness of the disk K_t (kN/m)
B1	39.17
B2	97.64
B3	105.33
B4	70.38

The relation between the transverse stiffness of the disk and the natural frequencies of the three mode shape is summarised in Fig. 4.11. It appears that all the natural frequncies of the three mode shapes increase with the increasing of the transverse stiffness of the disk, especially the (0,0) mode.

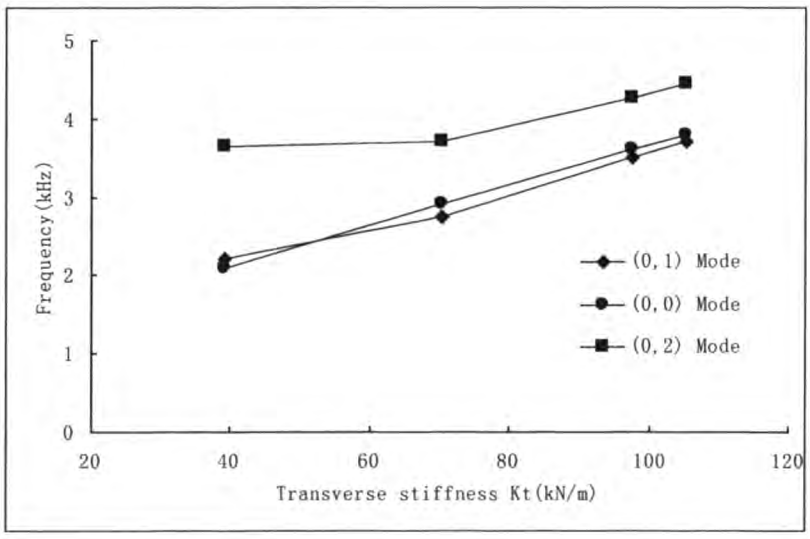

Fig. 4.11 Natural frequencies vs. Transverse stiffness

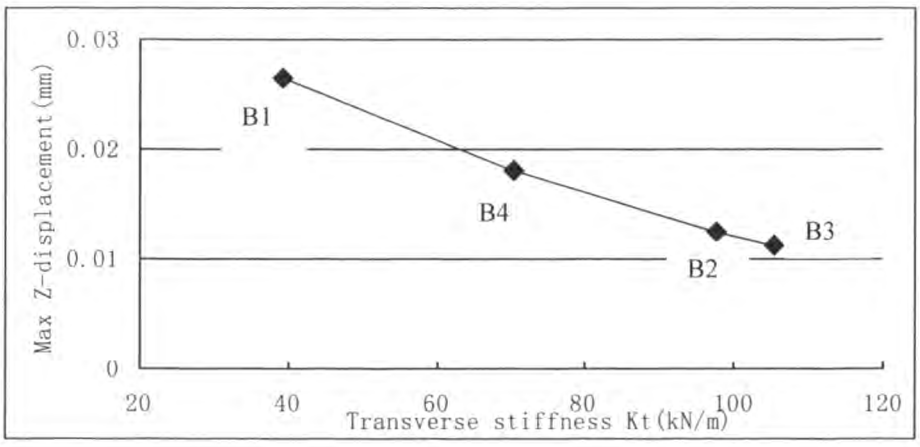

Fig. 4.12 Shock response vs. Transverse stiffness

Fig. 4.12 shows the maximum relative Z-displacement shown in Fig. 4.9 corresponding to the transverse stiffness of each simplified model. It appears that the shock response of the disk decreases with the increasing of the transverse stiffness.

From above discussion based on the simplified models of the disk, we can draw some conclusions as follow:

1. The real boundary condition of S1 disk is between simplified boundary condition B1 and B2. Boundary condition B4 can be approximated as the real boundary condition due to the close natural frequencies of (0,0) mode shape. So is the shock response.
2. The shock response of the disk is dominated by the umbrella mode when the shock is applied axisymmetrically
3. When the disk is more tightly clamped, the transverse stiffness of the disk will increase. The lower natural frequencies of the mode shape increase as well. The shock response of the disk will decrease accordingly. This will help to avoid the head slap behavior. In the disk design, the objective is to maximize the lower

natural frequency. We can take the transverse stiffness as the index of the natural frequency and the shock response of the disk.

4.2.3 Nonlinear FE Analysis with Surface-to-Surface Contact

In section 4.2.2, the influence of the boundary condition of disk on shock response is investigated with simplified FE models. Such study gives us a direct insight of the problem. In order to better understanding the real boundary condition of the disk, a more complicated FE model with surface-to-surface contact is created here.

Fig. 4.13 shows the overall FE model, which includes the disk, clamp and hub. The disk and clamp are modeled with shell elements and the hub is modeled with solid element. The hub and clamp are made of stainless steel with the density, Young's modulus, Poisson's Ratio being 8.08e-6 kg/mm^3, 190 Gpa, and 0.32 respectively. The disk is clamped between the clamp and the hub. The contact between the clamp and the disk, the disk and the hub are both modeled by using *'surface_to_surface_contact'* in ANSYS/LS-DYNA [76]. The disk is parallel with the X-Y plane. The clamp and the hub are assumed to be firmly bolted together by a screw at the center of the clamp and hub. The clamp is compressed onto the disk. So the disk is held in place by a clamping pressure. The shock pulse is assumed to apply on the hub and the center of the clamp at the same time.

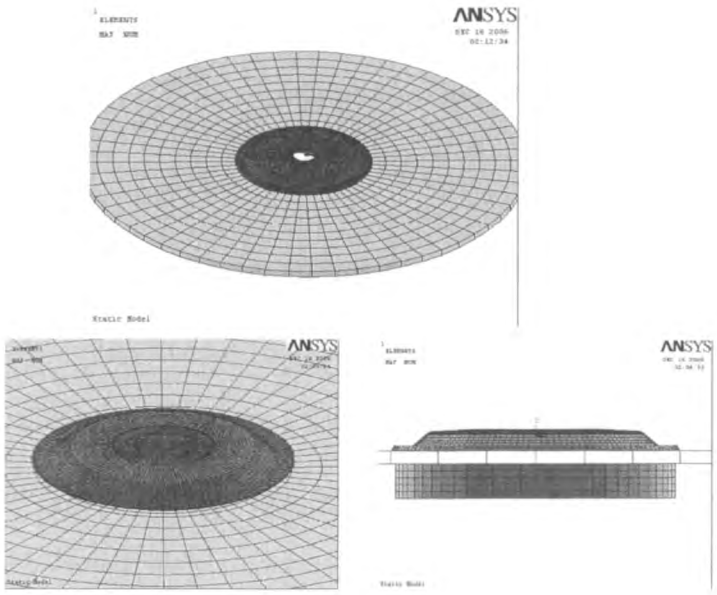

Fig. 4.13 The overall FE model

Due to the axisymmetry of the model and the load, the shock response of the disk is expected to be dominated by the umbrella mode according to the discussion in section 4.2.2. So only a quarter of the whole FE model is used in the simulation to save the computational time and the disk space. Symmetric constraints are applied on the symmetric surfaces. The quarter of the model is shown in Fig. 4.14..

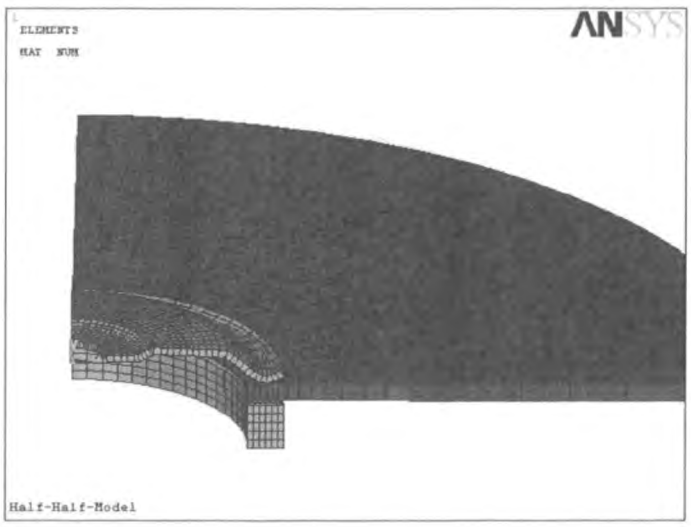

Fig. 4.14 Quarter of the FE model

4.2.3.1 Static Analysis with Preloading and Transverse Stiffness

In order to apply the clamping force before the transient analysis in LS-DYNA, an implicit nonlinear static analysis is conducted in ANSYS. A negative Z-direction displacement $-\tilde{D}$ is applied on the center of the clamp to make the clamp to deform. The clamp will contact the upper surface of the disk and press the disk on the static hub with a prescribed clamping force $\tilde{F}$. The design parameters, $\tilde{D}$ and $\tilde{F}$ are provided by the Seagate. The model after preloading is illustrated in Fig. 4.15.

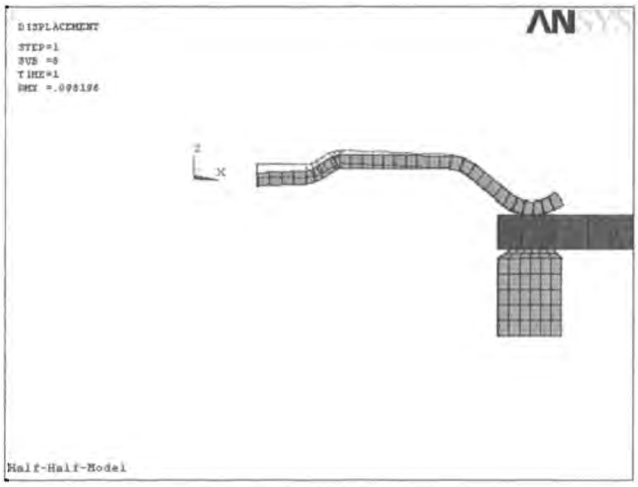

Fig. 4.15 Preloading of the clamping force

This static FE model becomes nonlinear with the involvement of the contact behaviour. It is difficult to do modal analysis to obtain the mode shapes and natural frequencies for this nonlinear model. Thus, according to the discussion in section 4.2.2, we can calculate the transverse stiffness of the disk, which can be used as the index of the natural frequency and the shock response of the disk.

After the application of the clamping force, we apply a positive and a negative Z-direction load of 0.25 N along the outer edge of the disk in the quarter model, respectively. The upward and downward deflection of the outer edge, as well as the

transverse stiffness of the disk are shown in Table 4.4. It is noted that the upward transverse stiffness is smaller than the downward transverse stiffness. The disk appears to be able to deflect upward more easily. It is due to the asymmetric clamping on the upper and lower disk surface caused by this one-screw-clamp design.

Table 4.4 The deflection and transverse stiffness of the disk

Total load (N)	Deflection of the outer edge (mm)	Transverse stiffness of the disk K_t (kN/m)
-0.25	-0.0112	89.2
0.25	0.0123	81.3

Comparison between Table 4.4 and Table 4.3 shows the downward and upward transverse stiffness of the nonlinear model are between that of the boundary condition B1 and B2 as shown in Table 4.3, but are greater than that of the boundary condition B4. The transverse stiffness of this nonlinear model may be overestimated due to the neglecting of the screw's deformation and neglecting of the relative displacement between the center of the clamp and the hub. Also in the experiment [75], the effects of spindle and FDB (fluid dynamic bearing) are both included, which are not modeled here.

4.2.3.2 Transient Analysis

After the application of the clamping force, the model is transfered into LS-DYNA to conduct the transient analysis. The shock pulse is applied on the hub and the center of the precompressed clamp. So their relative Z position does not change during the loading process. The *surface_to_surface_contact* between disk and hub, clamp and

disk are well defined. Fig. 4.16 shows the positive Z-direction half sine pulse shown in Fig. 4.6 is applied on the model. A negative Z-direction shock pulse is applied as well. Note here, the acceleration is applied at 1 ms. A 1 ms time delay is adopted to let the preloading stress inside the explicit FE model redistribute. The stress redistribution process will cause residual vibration in the model, which is cancelled by applying a high damping ratio to the model.

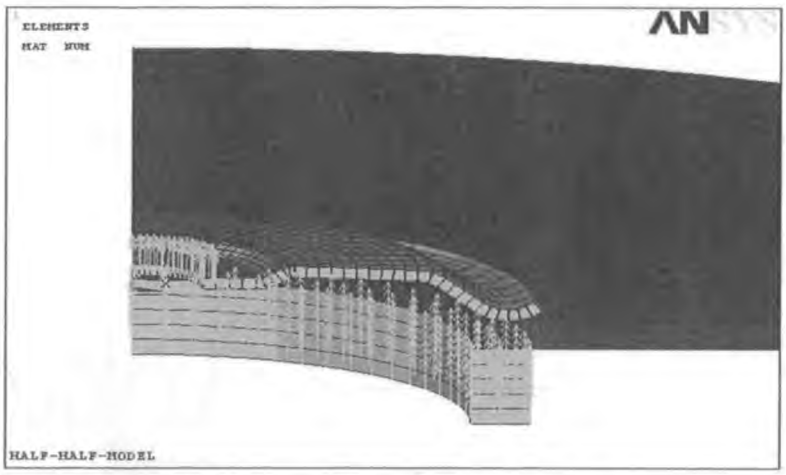

Fig. 4.16 Quarter model with shock applied

Fig. 4.17 shows the relative Z-displacement between the outer edge of the disk and the nodes where the acceleration pulse are applied. The shock response of the disk to the neagative shock and to the positive shock are plotted. It appears that the disk deflects upward under the negative shock and deflects downward under the positive shock. The upward deflection is greater than downward deflection as shown in Fig. 4.17. This is agreeable with the discussion in the static analysis: the transverse stiffness of downward deflection is greater than that of upward. But compare with the shock response of simplified boundary condition B4, both the upward and downward shock responses are relatively smaller. This is also indicated in static analysis by that their transverse stiffness are greater than that of boundary condition B4.

Fig. 4.18 shows the power spectra of the shock response. It shows both curves are close to each other and have close peaks which are around 3230 Hz. The frequency at peak is higher than the frequency of (0,0) mode in experimental results. This can be explained by the overestimation of the transverse stiffness caused by the neglecting of the screw's deformation as well as the effects of spindle and FDB, which are not included in this model.

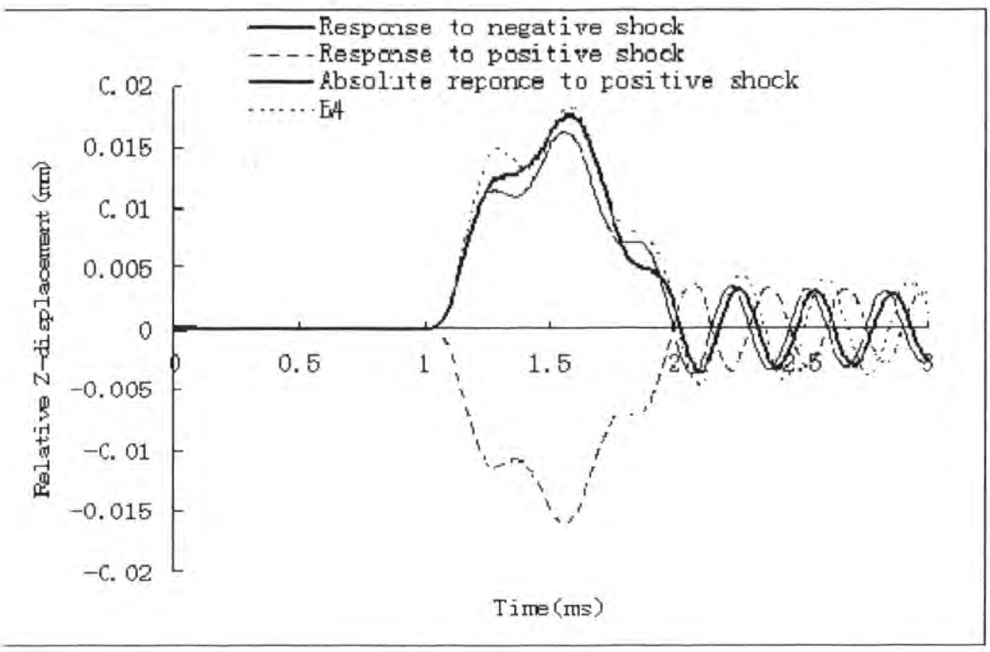

Fig. 4.17 Shock response of the disk

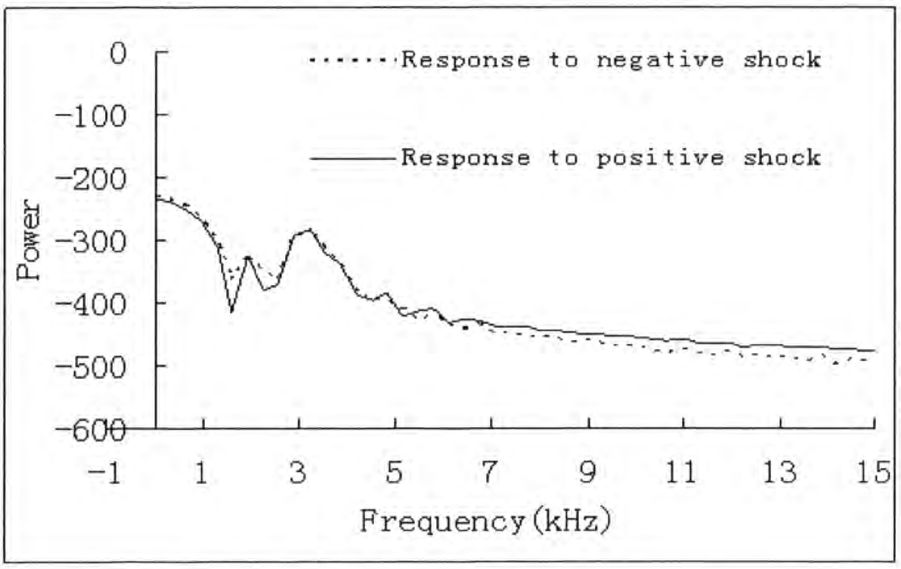

Fig. 4.18 Power spectra of shock responses

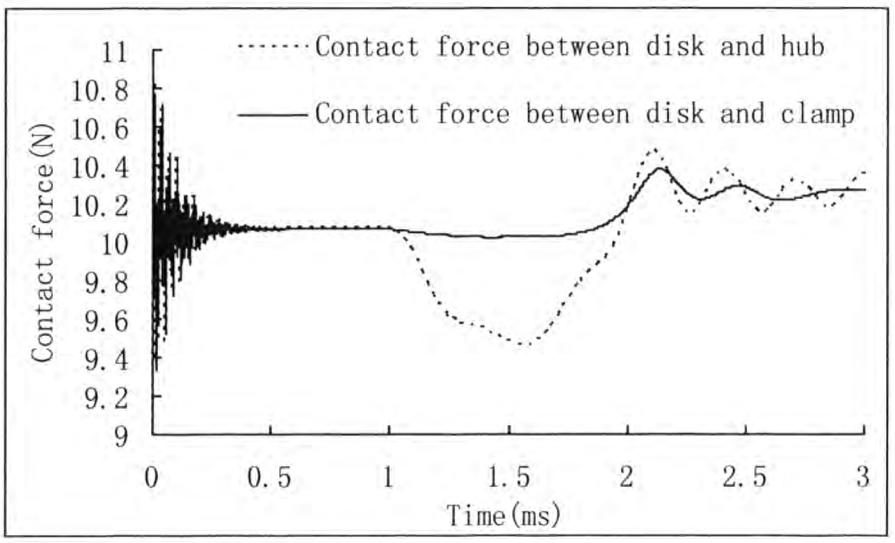

Fig. 4.19 Z-direction contact force during negative shock

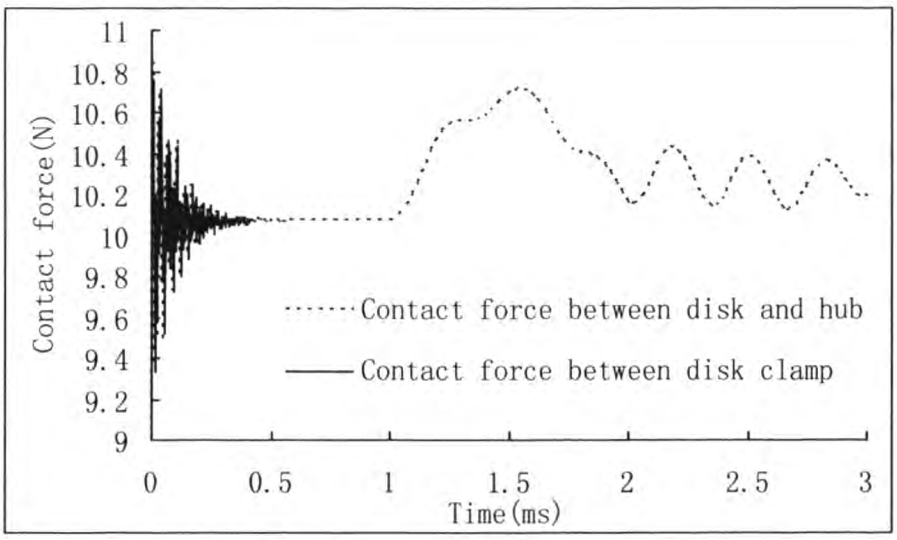

Fig. 4.20 Z-direction contact force during positive shock

Fig. 4.19 and Fig. 4.20 show the change of Z-direction contact force during negative shock and positive shock. It appears that the contact force between clamp and disk shows almost no change while the contact force between hub and disk shows a great change from 1 ms to 2 ms when the shock is applied. This can be explained by the simplified model shown in Fig. 4.21.

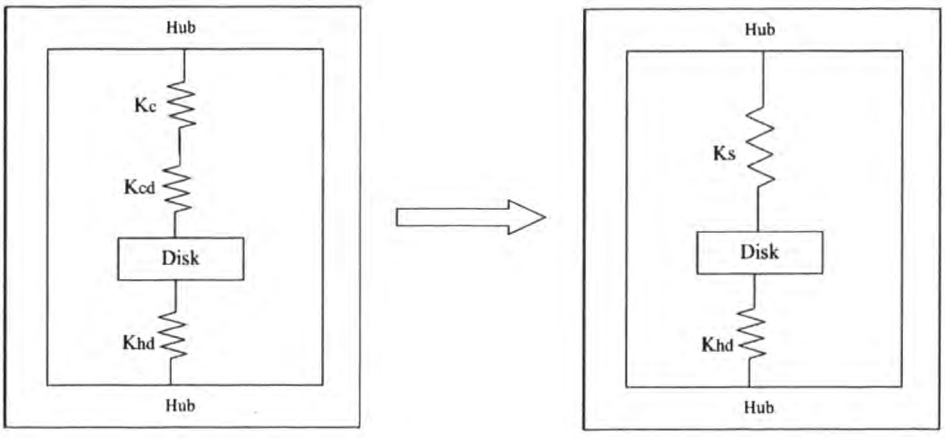

Fig. 4.21 The simplified one-degree-freedom model

For simplification, we only consider the rigid body movement of the disk. The mass of the clamp is also neglected. The clamp is modeled as a spring with a constant K_c.

The penalty method is used to model the contact. The contacts between clamp and disk, hub and disk are represented by linear springs between them. The stiffness of the springs, K_{cd} and K_{hd} determines the contact force when the average mutual approach of distant points, which is represented by the compression of the springs, is known. The spring constant K_c can be estimated from the prescribed clamping force $\tilde{F}$ and displacement $\tilde{D}$ as:

$$K_c = \frac{\tilde{F}}{\tilde{D}} \approx 400\text{N/mm} \tag{4.2}$$

The hub is made of steel and shows very small deformation in contact and is assumed as rigid body here. The contact stiffness between hub and disk can be estimated as [77]:

$$K_{hd} = \frac{A_d E_d}{H_d} = \frac{11.18\text{mm}^2 \times 83.5 \times 10^3 \text{N/mm}^2}{0.38\text{mm}} = 2.45 \times 10^9 \text{N/mm} \tag{4.3}$$

Here, A_d is the contact area between hub and disk. E_d is the Young's modulus of the disk. H_d is the thickness of the disk. It appears $K_{hd} >> K_c$.

The spring K_{cd} and K_c are in series and can be represented by a spring with a constant K_s. It is easy to see that $K_{hd} >> K_s$.

After the application of the clamping force, both spring K_{hd} and K_s will compress and exert balanced contact forces on the disk before the loading of shock as shown in Fig. 4.19 and Fig. 4.20. When the disk is subjected to the acceleration shock, it will move from the balance position due to inertial effect, causing spring K_{hd} and K_s compress or elongate the same distance $\delta(t)$ from the balance position. The change of the contact force between hub and disk ($K_{hd} \times \delta(t)$) is much greater than that between

clamp and disk ($K_s \times \delta(t)$) as shown in Fig. 4.19 and Fig. 4.20 due to the spring constant $K_{hd} >> K_s$. The total external force which exerts on the disk during the shock is $F_e(t)$. So we have:

$$F_e(t) = M_{disk} a_{disk}(t) \approx K_{hd} \delta(t) \tag{4.4}$$

We can see the change of clamping force between the hub and the disk plays an important role in providing the external force to balance the inertia force of the disk caused by the shock. According to equation (4.4), if we decrease the contact stiffness K_{hd} when the disk is subjected to the same shock pulse, the displacement of disk $\delta(t)$ is expected to grow bigger to satisfy the equation. Thus, the shock response of the disk is supposed to be greater when the contact stiffness K_{hd} is decreased.

Based on above, the disk component will be simplified as a SDOF system as shown in Fig. 4.22 by considering the rigid body movement only.

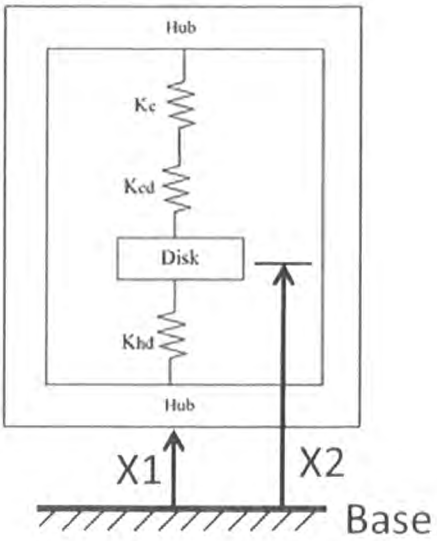

Fig.4.22 A simplified model of disk component as an SDOF system

Where,

x_1 is the hub input displacement,

x_2 is the absolute rigid body displacement of the disk,

Then $x = x_2 - x_1$ is the relative rigid body displacement of the disk.

The equation of motion of the system is

$$m\ddot{x}_2 + k_1(x_2 - x_1) = 0 \tag{4.5}$$

where, k_1 is the equivalent stiffness and satisfy

$$k_1 = k_{hd} + \frac{k_{cd} \times k_c}{k_{cd} + k_c} \tag{4.6}$$

Consider a single half-sine acceleration pulse as given by equation (4.7).

$$\ddot{x}_1(t) = \begin{cases} A_0 \sin\left(\dfrac{\pi t}{\mathrm{T}}\right), & 0 \le t \le \mathrm{T} \\ 0, & t > \mathrm{T} \end{cases} \tag{4.7}$$

Where T is the duration of the half-sine acceleration pulse, A_0 is the amplitude of the acceleration pulse.

By convention, let $k_1 / m = \omega_1{}^2{}_n$. Where, $\omega_1{}^2{}_n$ is the natural frequency in (radians/sec).

And let

$$\omega = \frac{\pi}{\mathrm{T}} \tag{4.8}$$

$$x = x_2 - x_1 \tag{4.9}$$

The equation of the motion then becomes

$$\ddot{x} + \omega_{1n}^2 x = -A_0 \sin(\omega t), \quad 0 \le t \le T \tag{4.10}$$

4.2.4 Effects of Contact stiffness and Clamping Force

In this section, the effect of the contact stiffness between the hub and the disk and the effect of the clamping force are discussed based on the nonlinear FE model.

4.2.4.1 Contact Stiffness between Hub and Disk

From the disscusion based on the simplified model shown in Fig. 4.22, if the contact stiffness between the hub and disk decreases, the disk is supposed to have a greater shock response under the same shock pulse.

Here we verify the effect of contact stiffness between the hub and disk in transient analysises. In ANSYS-LSDYNA, penalty method is used to model the contact. A default contact stiffness is determined automatically by the ANSYS-LSDYNA program taking account of the size of elements and material properties of the contact parts. In the next transient analysises, we change the contact stiffness between hub and disk from default value K to 0.3K and 3K by multiflying factors 0.3 and 3.0, respectively. Fig. 4.23 and Fig. 4.24 show the effect of the contact stiffness on the shock reponce. The shock response decreases considerably when the contact stiffness become greater. In order to increase the contact stiffness, according to formula (4.3), we can increase the clamping area between the disk and hub or increase the hardness of the contacting surface of the disk. Decreasing the thickness of disk in clamping area is not recommeded. This method will get a smaller transverse stiffness and frequencies for the disk according to the study by Renshaw [78].

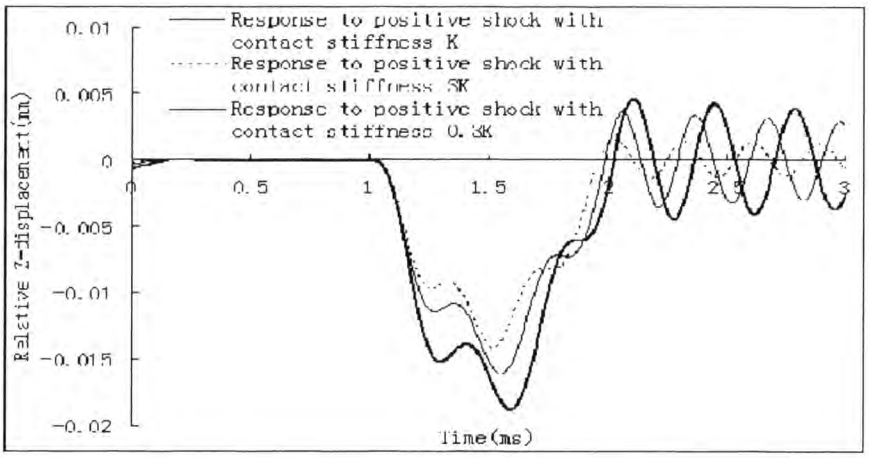

Fig. 4.23 Effect of the contact stiffness on the positive shock

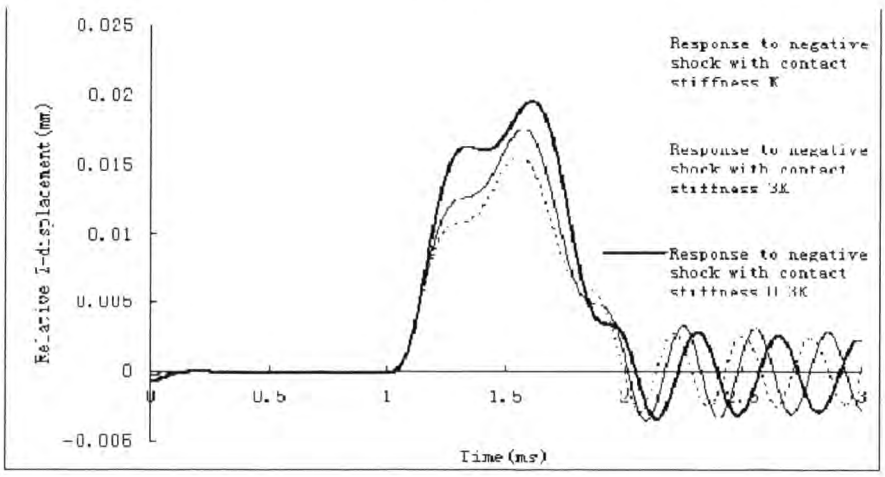

Fig. 4.24 Effect of the contact stiffness on the negative shock

However, it is noted that the effect is not as large as expected; e.g. by increasing the contact stiffness for 3 times, the Z-displacement is only reduced by about 10%. The reason is that contact stiffness only affects the disk rigid body displacment, which only contributes a small portion of the disk relative displacement. Most of the disk relative displacement is from the disk deflection caused by disk bending.

Based on above, the disk component will be further simplified as a SDOF system as shown in Fig. 4.25 by considering the disk bending.

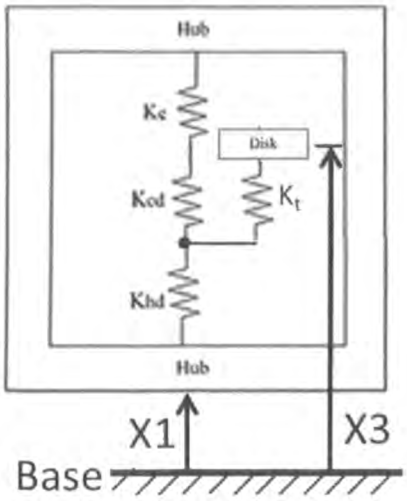

Fig.4.25 A simplified model of disk component as an SDOF system

Where,

x_1 is the hub input displacement,

x_3 is the absolute displacement of the disk,

k_t is the transverse stiffness of the disk,

$z = x_3 - x_1$ is the relative displacement of the disk.

The equation of motion of the system is

$$m\ddot{x}_3 + k(x_3 - x_1) = 0 \tag{4.11}$$

where, k is the total equivalent stiffness and satisfy

$$k = \frac{k_1 \times k_t}{k_1 + k_t} \tag{4.12}$$

Same precedures as Eq. (4.5),

The equation of the motion is obtained

$$\ddot{z} + \omega_n^2 z = -A_0 \sin(\omega t), \quad 0 \le t \le T \tag{4.13}$$

Because $k_1 >> k_t$, the total equivalent stiffness k is close to k_t. The disk relative displacement is controlled by transverse stiffness of the disk.

4.2.4.2 Clamping Force

The next parameter we discuss about is the clamping force. In secton 4.2.3, the preloaded clamping force is $\tilde{F}$ by applying a negative Z-displacement $-\tilde{D}$ to the clamp center. Now we make the displacement to $-1.5\tilde{D}$. So the clamping force becomes $1.6\tilde{F}$ accordingly. Fig. 4.26 and 4.27 show that the disk shock response decreases when the clamping force increases from $\tilde{F}$ to $1.6\tilde{F}$. It is help to decrease the disk shock response by increasing the clamping force. But if the clamping force is too high, it may crack the glass disk. The maximum of the clamping force should be carefully determined by the strength of the disk .

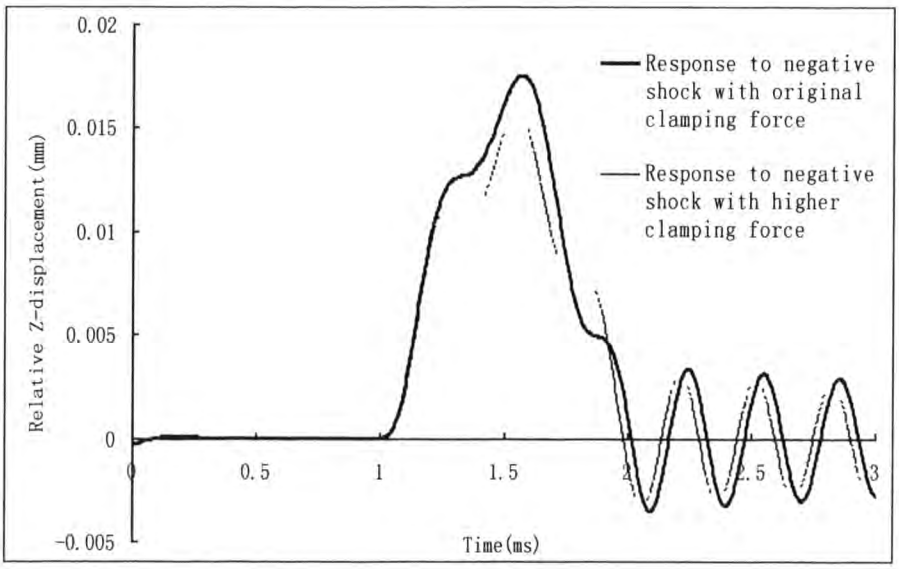

Fig. 4.26 Effect of the clamping force on the positive shock

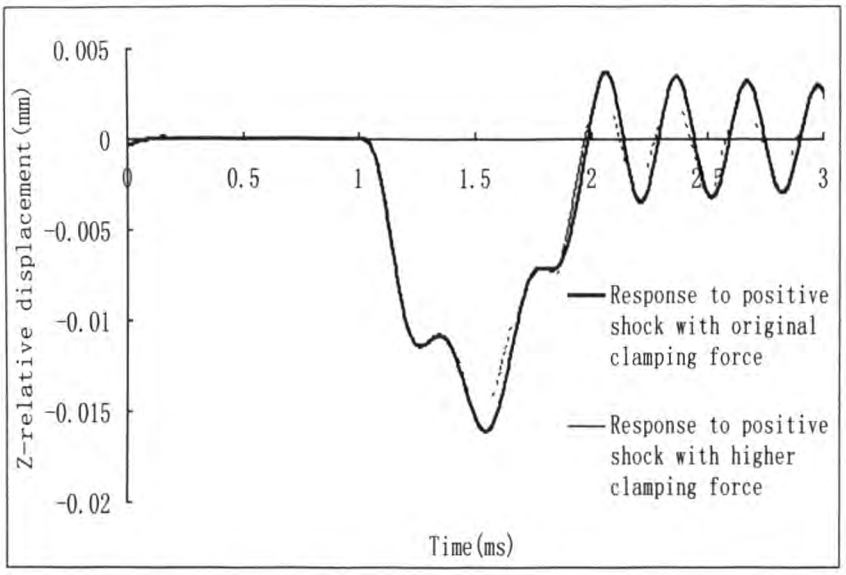

Fig. 4.27 Effect of the clamping force on the negative shock

4.2.5 Summary

The influence of the boundary condition of disk and corresponding load condition is investigated by finite element analysis method. Modal analysis is conducted with simplified models and shock responses are also obtained. The comparison with experimental results shows the real boundary condition of the disk is neither simply supported nor clamped. Power spectrum analysis shows the shock response of the disk is dominated by the umbrella mode when the shock is applied axisymmetrically. The transverse stiffness of the disk is defined. It can be taken as the index of the natural frequencies as well as the shock response of the disk.

The real boundary condition of the S1 disk is simulated with a FE contact model considering the preloading of the clamping force and contact behavior. The shock response is obtained. The results show a good agreement with the results from the simplified models and the experiments. Based on the nonlinear FE model, the effect

of the contact stiffness between the disk and the hub and the effect of the clamping force are discussed. Results show it help to mitigate the shock response of the disk by increasing contact stiffness between disk and hub and the clamping force.

4.3 FEA Simulation of the Non-operational Linear and Rotary Drop Test of A HDD

In this section, the non-operational shock response for the S1 drive from Seagate is investigated. A finite element model of the hard disk drive was developed in the commercially available finite element package, ANSYS. The overall model includes the HDD enclosure base, the HAS, the pivot bearing and the disk. The non-operational linear drop test and rotary drop test are simulated using the implicit to explicit analysis function of ANSYS. In the linear drop test, a half-sine acceleration pulse is applied to the edges of the enclosure base. In the rotary drop test, a half-sine acceleration pulse is applied to the impact edge. The translational freedom of the opposite edge, which acts as the rotating axis, is constrained. The rotary model is derived from proposed experiment as shown in Fig. 4.28. HDD base is constrained to rotate about one edge and is allowed to drop and impacted the opposite edge.

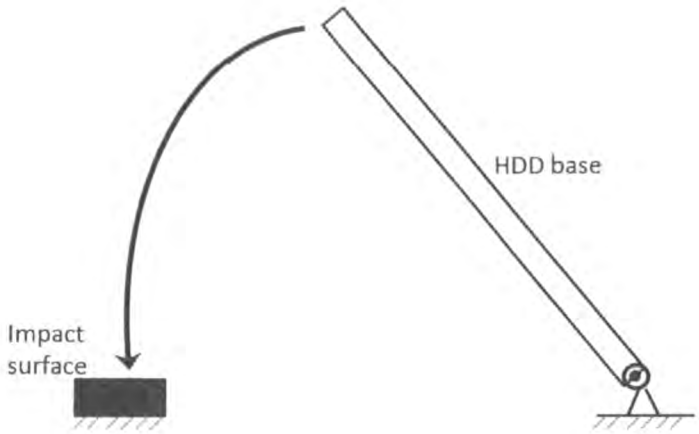

Fig. 4.28 Rotary drop test of HDD

The linear drop test with different amplitude and duration of the half-sine acceleration pulse are simulated. The rotary drop test with different combinations of rotary axis and amplitude and duration of the half-sine acceleration pulse are also simulated.

The objective of the present work is to investigate and compared the head slap behavior in these simulations and to identify the most vulnerable drop condition for the HDD. In section 4.3.1, the finite element model with the base plate is illustrated. The linear drop test and rotary drop test are simulated by using finite element package, ANSYS/LSDYNA in section 4.3.2. Some conclusions are shown in the last section 4.3.3.

4.3.1 The Finite Element Model With The Base Plate

The finite element method (FEM) has been successfully used to study the dynamic responses of assemblies in HDDs. In this section, a finite element model of S1 HDD

was created using the commercially available finite element software package, ANSYS version 9.1. The overall model includes the HDD enclosure base, the head stack assembly (HSA), which includes the over mold with inlaid coil and two arms with two head suspension assemblies, the pivot bearing and the disk. The details of the head gimbal assembly are also modeled. The over mold, pivot shaft, screw, shim, arm, slider are meshed with solid elements while the hinge, load beam, gimbal, disk and the enclosure base are meshed with shell elements. The pivot bearing is simulated with 36 spring elements. Fig. 4.29 shows the FE model of head disk assembly.

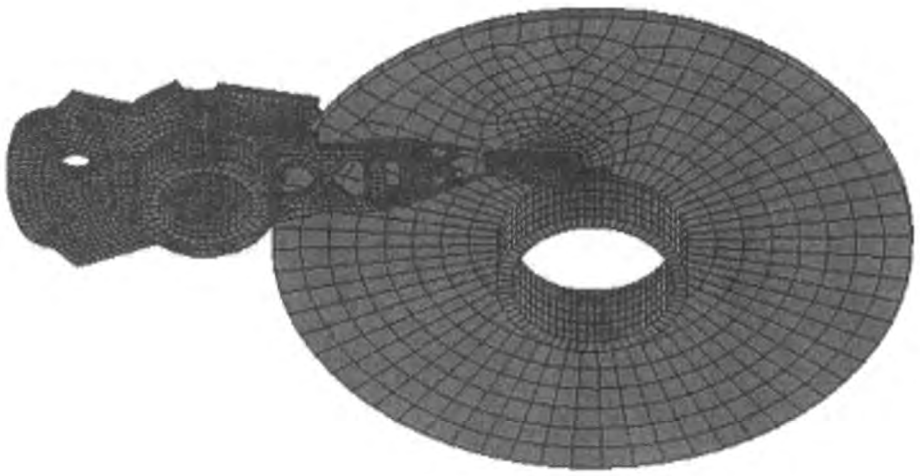

Fig. 4.29 FE model of HDA

In order to get valid transient analysis results, the FE model needs to be carefully verified. Modal analysis is conducted on the HSA for the verification of the FE model. As the acceleration is applied in the z- direction, it mainly excites the vertical modes of the suspension. In the verification, we select several vertical modes (bending modes) to compare with the modal testing results. The selected modes are: the first and the second free bending mode (obtained from the modal analysis of the free-state one-head HSA); the first and the second bending mode of the two-head HSA with the preloading force considered. The modal analysis and modal testing results are shown

in Table 4.5. As there are two suspensions for the two-head HSA, two similar resonant modes exist for each characteristic mode. The resonant frequencies for the same characteristic mode are only slightly different from Table 4.5, we can see the modal analysis results coincide very well with the modal testing results.

Table 4.5 Comparison of the mode frequencies between simulation and experiment

Main Modes	Simulation (Hz)	Experiment (Hz)
1st free bending	258	255
2nd free bending	3680	3766
1st bending	3520/3622	3700
2nd bending	9980/11830	10080

The shaft, screw, shim, gimbal, arm and suspension, enclose base are made of stainless steel with the density, Young's modulus, Poisson's Ratio being 8.08e-6 kg/mm^3, 190 Gpa, and 0.32 respectively. Fig. 4.30 shows a view of the HDD model before preloading.

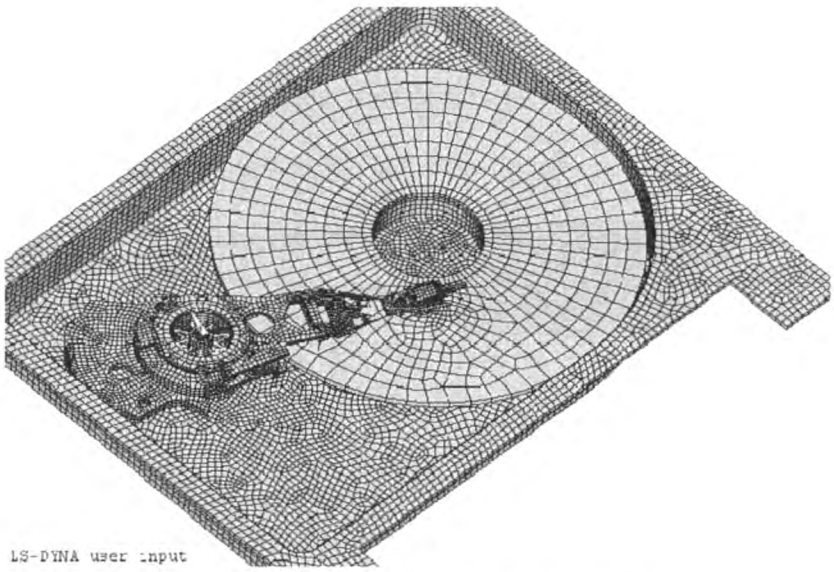

Fig. 4.30 HDD FE model before preloading

The Cartesian coordinate, X, Y, Z are parallel to the directions of the drive length, width, and thickness respectively. The whole FE model includes 10117 solid elements and 12722 shell elements. The suspension is formed with an initial bending angle to produce prescribed preloading force of 0.012 N as Fig. 4.31 shows. A displacement loading is applied to the four corner of the slider. The displacement loading pulls the suspensions to the proper z-height and lets the two sliders rest on the upper and lower surface of the disk respectively. Fig. 4.32 shows the positions of the sliders after the preloading. This preloading process is simulated with an implicit nonlinear static analysis in ANSYS. After the implicit static analysis, the implicit FE model is converted to an explicit FE model. Before the explicit transient analysis, the locations of the nodes of the whole model are updated with the static analysis results and the preloading stress is retained in the FE model. 'Automatic surface to surface contact' is defined between the bottoms of the two sliders with the disk.

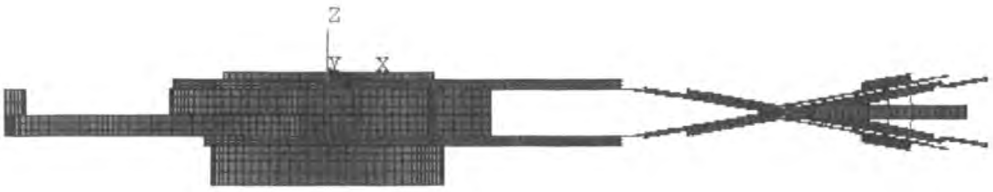

Fig. 4.31 The position of the sliders before preloading

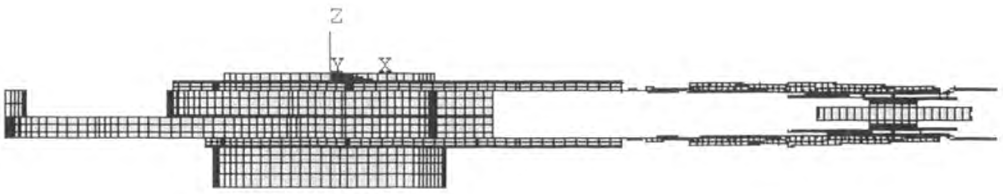

Fig. 4.32 The position of the sliders before preloading

4.3.2 FEA Simulation of Linear and Rotary Drop Test

Based on the Finite Element Model illustrated in section 4.3.1, the FEA simulation of linear and rotary drop tests was conducted. Fig. 4.36 shows the three Z-negative shock pulses applied in the drop test simulations. Shock pulse 1, 2 and 3 represent the acceleration of the -300 g (1 g=9.8 m/s^2) and 1 ms half sine shock pulse, -300 g and 0.5 ms half sine shock pulse and -600 g and 1 ms half sine shock pulse, respectively. The shock pulse is applied on the two short edges of the base in the simulation of the linear drop test as Fig. 4.37 shows. This is to simulate the up-side-down drop test condition-the two short base edges of HDD are clamped onto the drop table. The drop

table drops from a range of different heights onto a surface with different stiffness. Thus, the half sine shock pulses with different amplitude and pulse width are produced. Fig. 4.38 shows the shock pulse is applied on the short base edge in the vicinity of the disk. The Z-displacement of the end of the opposite edge is constrained, which acts as the axis of rotation. This is to simulate the up-side-down rotary drop test condition.

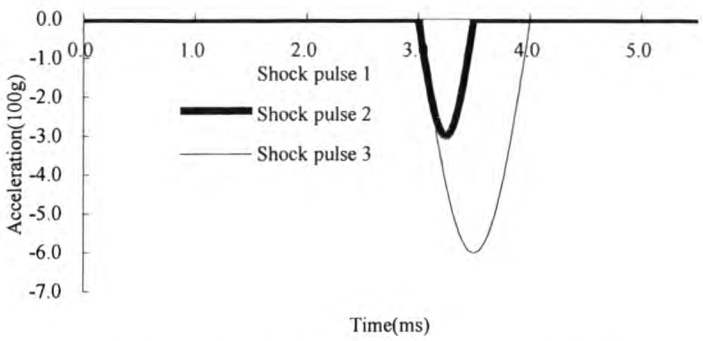

Fig. 4.33 Z-negative half sine shock pulses

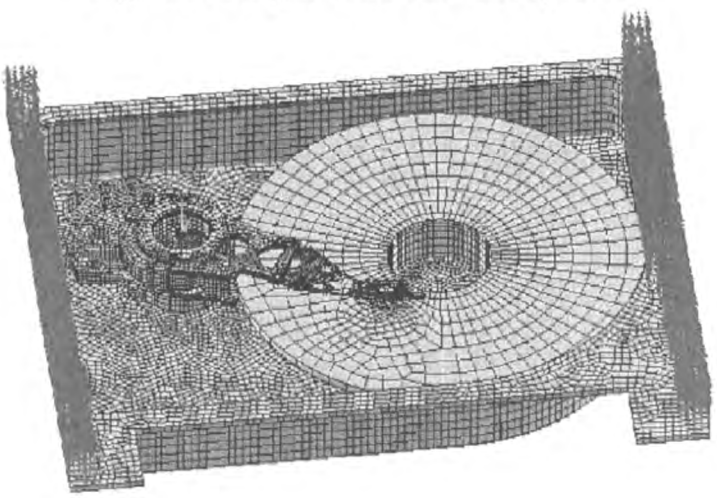

Fig. 4.34 Model of linear drop test with acceleration pulse on edges

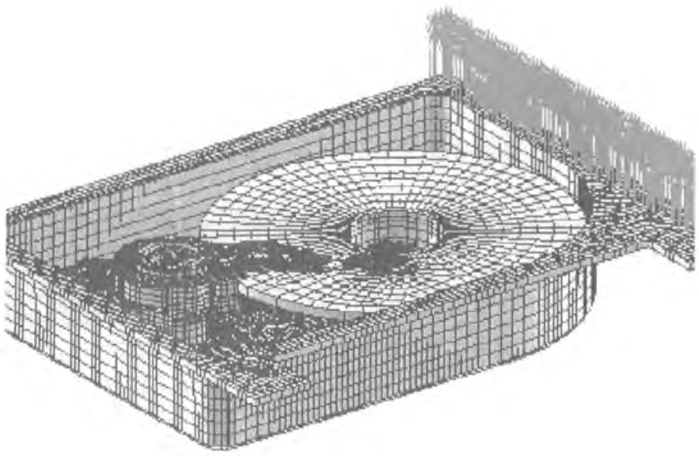

Fig. 4.35 Model of rotary drop test with acceleration pulse on one edge

Note here, the acceleration is applied at 3 ms. This time delay is adopted to let the preloading stress inside the explicit FE model redistribute. The stress redistribution process will cause residual vibration in the HSA, which is cancelled by applying a damping ratio to the model.

Fig. 4.36 shows the shock response when HDD is under -300 g and 1 ms shock pulse in the linear drop test simulation. Fig. 4.36(a) shows the relative displacement in z-direction of the upper slider and the lower slider centres. Fig. 4.36(b) shows the velocity of the slider centres and the disk at the slider centre location. The displacement of the sliders in the figure is relative to the displacement of the disk at the slider centre location. In Fig. 4.36(a), the upper slider lifts off and the lower slider shows a rather small separation from the disk. From Fig. 4.36, we can see how the head slap of the upper slider takes place. The shock acceleration starts to act on the HDD at point 1. From point 1 to 2, the sliders and disk have the same velocity and displacement. From point 2 to 3, the absolute velocity of the disk is greater than that of the upper slider. Thus, the upper slider starts to lift off from the disk. The lift-up height reaches maximum at point 3 when the disk and the upper slider get the same

velocity again. After point 3, with the increasing of the absolute velocity of the slider and the decreasing of the absolute velocity of the disk, they approach. Then at point 4, the upper slider starts to slap on the disk. According to the animation of the result, the edge of the slider hits the disk first due to the pitch and roll of the slider. Then the point 4 is ahead of the point 5 when the upper slider centre contacts the disk.

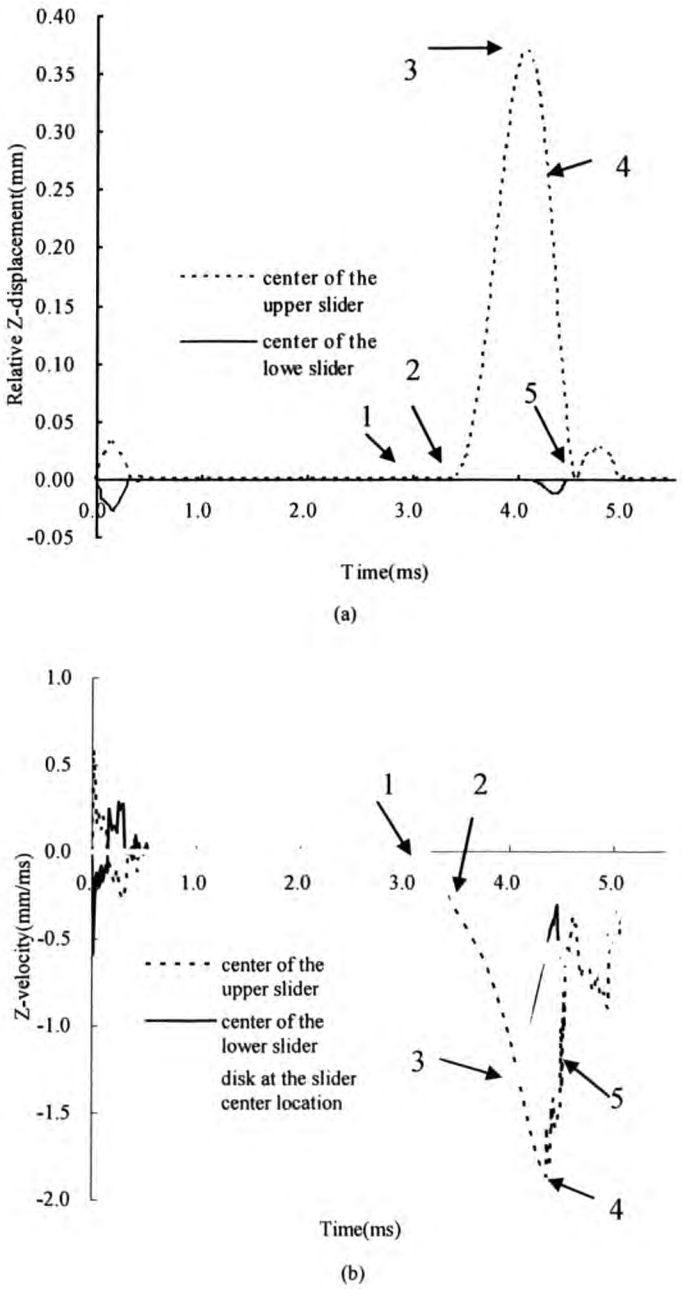

Fig. 4.36 The shock response in the linear drop test when HDD is under -300g and 1 ms shock pulse

Fig. 4.37 and Fig. 4.38 show the relative displacement in z-direction of the upper and lower sliders in the linear drop tests when HDD is under -300 g and 0.5 ms shock pulse, -600 g and 1 ms shock pulse respectively. Fig. 4.39, Fig. 4.40 and Fig. 4.41 show the relative displacement in z-direction of the sliders in the rotary drop tests when HDD is under -300 g and 1 ms shock pulse, -300 g and 0.5 ms shock pulse and -600 g and 1 ms shock pulse respectively. In each figure, the relative displacement pulses at the beginning represent the residual vibration caused by the stress redistribution.

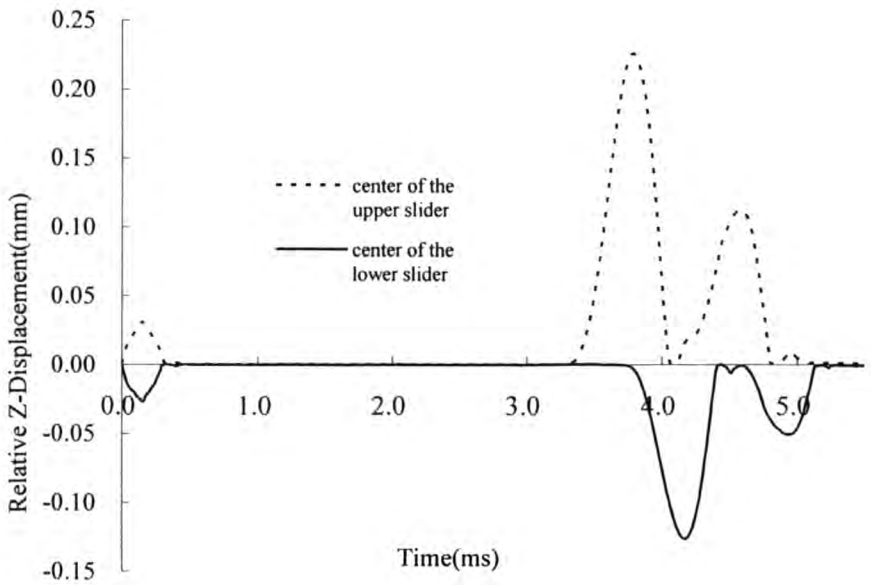

Fig. 4.37 The relative Z-displacement in the linear drop test when HDD is under -300g and 0.5 ms shock pulse

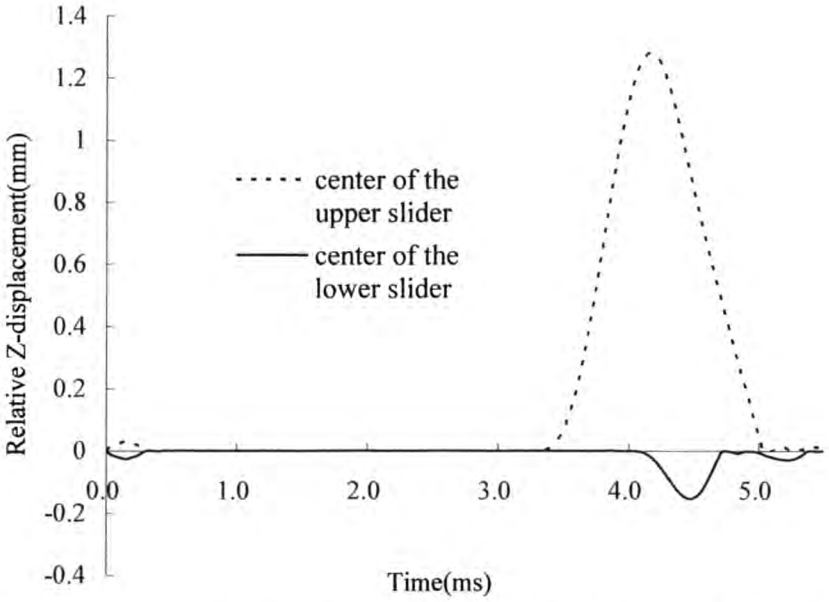

Fig. 4.38 The relative Z-displacement in the linear drop test when HDD is under -600g and 1 ms shock pulse

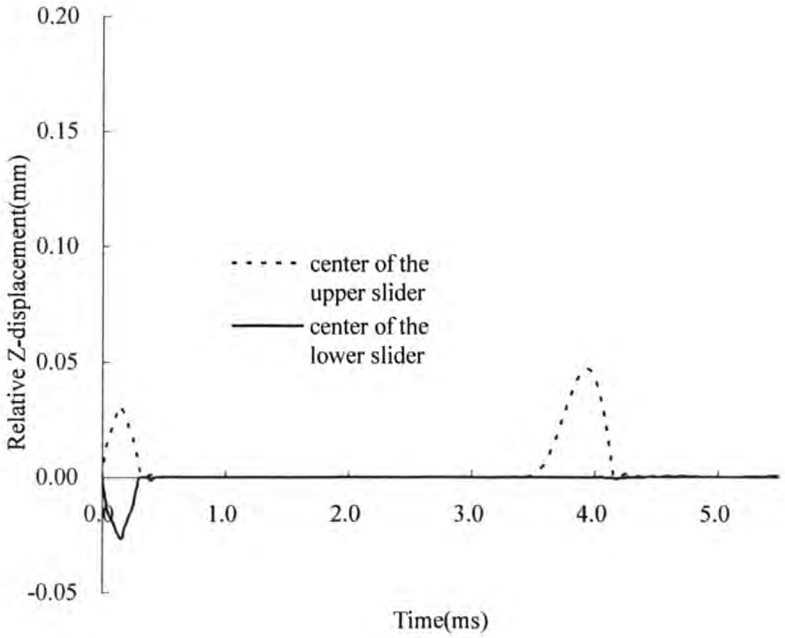

Fig. 4.39 The relative Z-displacement in the rotary drop test when HDD is under -300 g and 1 ms shock pulse

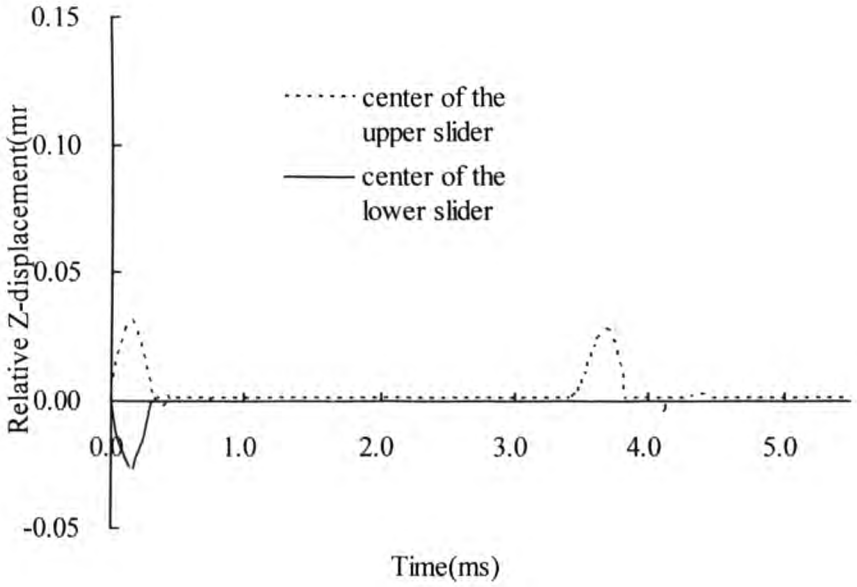

Fig. 4.40 The relative Z-displacement in the rotary drop test when HDD is under -300 g and 0.5 ms shock pulse

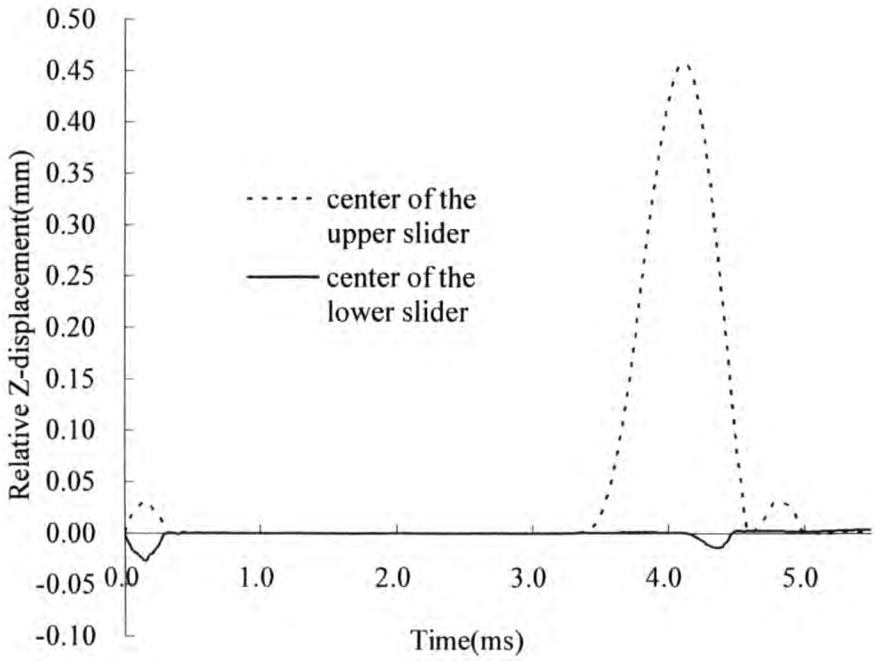

Fig. 4.41 The relative Z-displacement in the rotary drop test when HDD is under -600 g and 1 ms shock pulse

In Fig. 4.36(a), the upper slider starts to lift off at time t = 3.32 ms and reaches the maximum lift-up height of 0.37 mm at time t = 4.08 ms. In Fig. 4.37 both the upper slider and the lower slider lift off under the -300 g and 0.5 ms shock pulse. The upper slider starts to lift off at time t = 3.25 ms and reaches the maximum lift-up height of 0.23 mm at time t = 3.79 ms. The lower slider also starts to lift off at time t = 3.72 ms and reaches the maximum lift-up height of 0.13 mm at time t = 4.17 ms. It can be seen that the maximum lift-up height in Fig. 4.36(a) is higher than that in Fig. 4.37. This can be explained by that the 1 ms shock applies more energy to the HDD than the 0.5 ms shock does. But on the other hand, the lower slider in Fig. 4.37 shows head slap and more head slaps for both sliders are observed than in Fig. 4.36(a). It suggests that the head slap is more likely generated in short duration shock. In this FE model, the disk is clamed and the sliders locate at the ID of the disk. The disk dominant umbrella mode is 3800 Hz and the first HSA bending mode is 3520 Hz. The HDD is more sensitive to the shorter duration shock. Fig. 4.38 shows both slider lift off significantly when the HDD is under -600 g and 1 ms shock pulse. The maximum lift-up heights of the upper and lower slider are 1.28 mm and 0.15 mm respectively, which is very higher than the maximum heights in Fig. 4.36(a) and Fig. 4.37.

In Fig. 4.39, the upper slider lifts off in the rotary drop test when the HDD is under -300g, 1 ms shock pulse. However, the maximum lift-up height is much smaller than that in linear drop test, which is under the same shock pulse. Fig. 4.40 shows both sliders separate from disk but the maximum lift-up height is very small. In Fig. 4.41, both sliders lift off and the upper slider lifts up much higher compared with Fig. 4.39 and 4.42. It is showed the HDD is also sensitive to short duration shock in the rotary drop test. The lift-up height will also increase significantly in the rotary drop test when the HDD is under greater amplitude of shocks. But under the same shock pulse

the magnitude of the slider lift-up height in linear drop test is much greater than that in rotary drop tests.

4.3.3 Summary

In both linear drop tests and rotary drop tests there are head slap events present and HDD shows more sensitivity to the shorter duration shock. And the magnitude of the slider lift-up height grows significantly when HDD is under greater amplitude of shocks. Moreover, comparison between linear drop tests and rotary drop tests shows that under the same shock pulse the slap behavior in linear drop tests is more significant than in rotary drop tests in view of the slider lift-up height. Thus, we conclude that in the model, drives under linear drop test with greater amplitude and shorter duration shock were more vulnerable in consideration of the head slap behavior. But this should be verified experimentally further.

4.4 FEA Simulation of The Shock Response of An Operational Disk Drive

Shi et al. [64] conducted operational shock simulation with a finite-element model, and investigated the pulse width effect of a half sine shock pulse on the shock response. But the air bearing was modeled with linear springs, which were not able to capture the true behavior of the air bearing. In this section, the air bearing between the disk and the slider is modeled by nonlinear springs. The contact between the disk and the slider is also considered. The effect of disk clamping conditions on the operational shock response of HDDs is investigated. The shock pulse amplitude and width effects on the shock response of an operational HDD are also studied numerically.

4.4.1 FE Model

Fig. 4.42 shows the finite element (FE) model of the head disk assembly (HDA), including those of the disk and the head arm assembly (HAA), as well as the air bearing between the disk and the slider. The FE model of the HDA has 4861 nodes and 3642 elements, including 1601 solid elements, 2036 shell elements and 5 spring elements. To produce a prescribed preloading force between the slider and the disk, the HAA is preformed with an initial bending angle at the middle line of the hinge. The disk is parallel to the slider surface and will rotate the same angle simultaneously

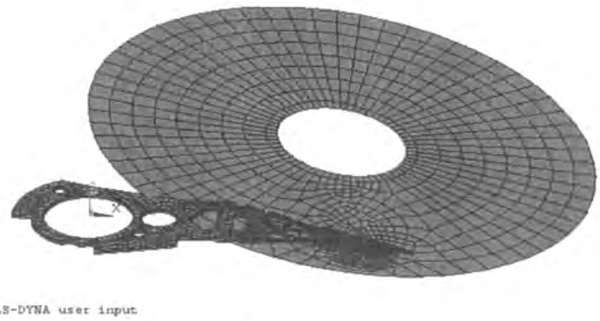

Fig. 4.42. Finite element model of the HDA.

after a displacement loading is applied to the disk. Due to spring elements between the disk and the slider, the displacement loading pushes not only the disk but also the HAA to the proper z-height. This preloading process is simulated with an implicit nonlinear static analysis in ANSYS. After the implicit static analysis, the implicit FE model is converted to an explicit FE model. Before the explicit transient analysis, the locations of the nodes of the whole model are updated with the static analysis results and the preloading stress is retained in the FE model. After updating, the disk surface is parallel to X-Y coordinate. To consider the contact between the disk and the slider, 'automatic surface to surface contact' is defined between the disk (target part) and the bottom of the slider (contact part) in LS-DYNA. Contact force between the disk and

the slider is obtained through the simulation results. Shocks are simulated as half sine acceleration pulses which are applied at the center of the disk and the arm in negative Z direction.

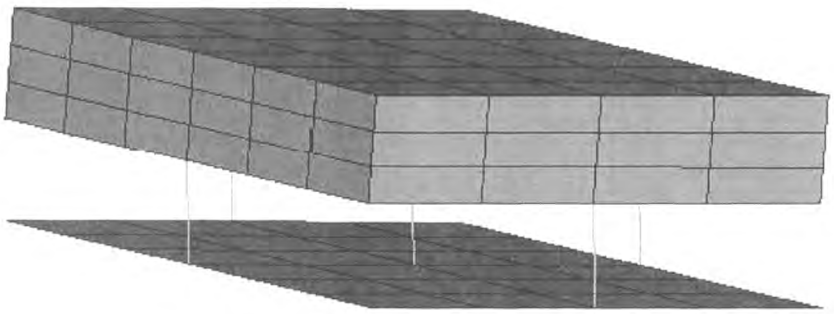

Fig. 4.43. Spring elements for air bearing.

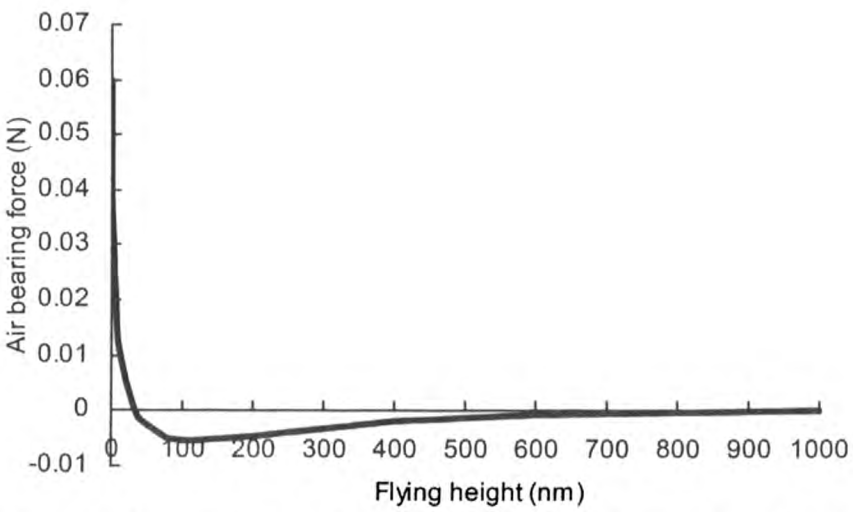

Fig. 4.44. Nonlinear relationship between the air bearing force and the flying height.

Five spring elements are located at the center and side rails of the slider to simulate the vertical stiffness, pitch stiffness and roll stiffness of the air bearing as shown in Fig. 4.43. In Ref. 64, linear spring elements with constant stiffness were used. However, the air bearing was able to support a negative load and retained the slider on the disk even for a rather high amplitude shock such as 600 G. This is not true for a real HDD. The air bearing behavior is nonlinear [79-81]. The vertical stiffness was a

function of flying height [80], [81]. Additionally, the air bearing force also behaves nonlinearly with respect to pitch angle and roll angle. In this paper, only the nonlinearity of the vertical stiffness is considered. The air bearing stiffness of a particular slider design is determined by the geometry of the air bearing surface (ABS). The pressure of the air bearing is described using the compressible Reynolds equation including a slip correction factor Q as following,

$$\frac{\partial}{\partial x}\left(ph^3 Q\frac{\partial p}{\partial x}\right)+\frac{\partial}{\partial y}\left(ph^3 Q\frac{\partial p}{\partial y}\right)=6\mu\left[U\frac{\partial(ph)}{\partial x}+V\frac{\partial(ph)}{\partial y}\right]+12\mu\frac{\partial(ph)}{\partial t}. \qquad (4.14)$$

Where p is the pressure, h is the flying height distribution, μ is the viscosity of air, U and V are the local disk velocity in the x and y direction, respectively. By using CML code which numerically solving Reynolds equation using finite volume method, the nonlinear relationship between the air bearing force and flying height for the HDD modeled in this project is obtained as shown in Fig. 4.44. The pitch angle and roll angle are fixed at 80 μ radians and 0 radians. Based on Fig. 4.44, the nonlinear spring elements are described with force/elongation relation as shown in Fig. 4.45.

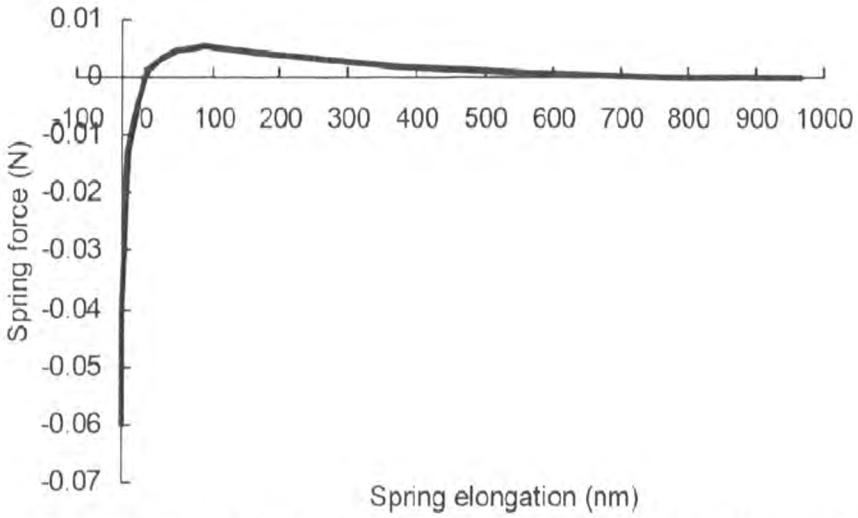

Fig. 4.45. Nonlinear relationship between the spring force and the spring elongation.

4.4.2 Disk Clamping Condition Effect

To investigate the disk clamping condition effect, as shown in Fig. 4.46, the acceleration pulse is applied to nodes along the outer circle of the clamped zone of the disk when the disk is simply supported; the acceleration pulse is applied to nodes along both the inner and outer circles of the clamped zone when the disk is fully clamped. As shown in Fig. 4.47, the pulse width is kept at 1 ms and the amplitude of the shock pulse is varied from negative 200 G to negative 400 G.

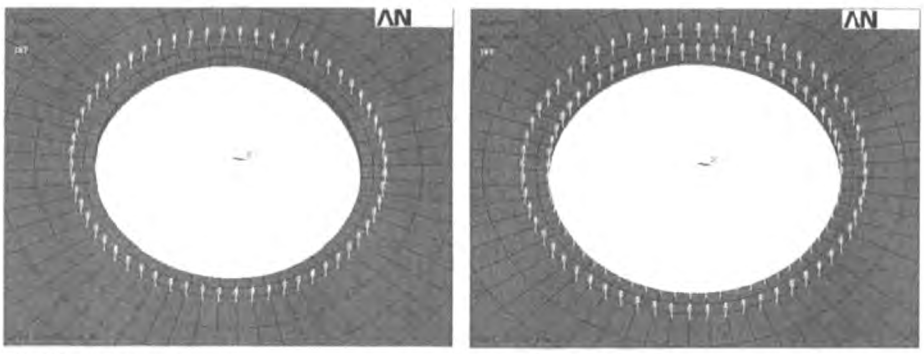

(B1) Simply supported (B2) Fully clamped

Fig. 4.46. Disk clamping conditions.

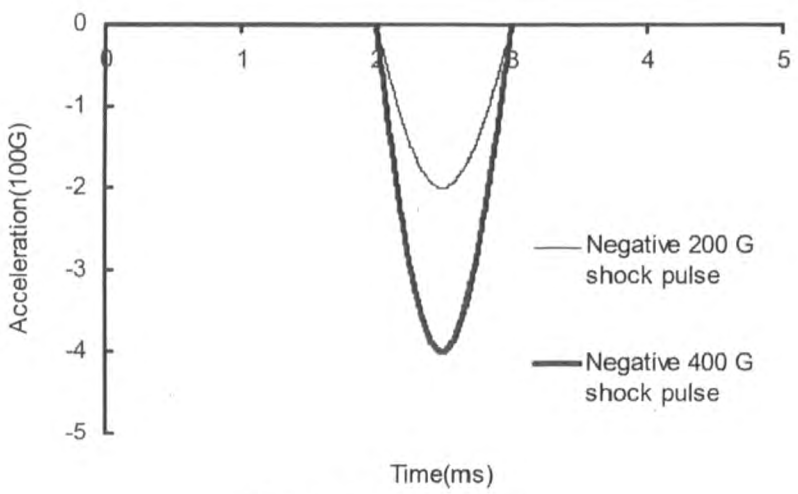

Fig. 4.47. Shock pulses.

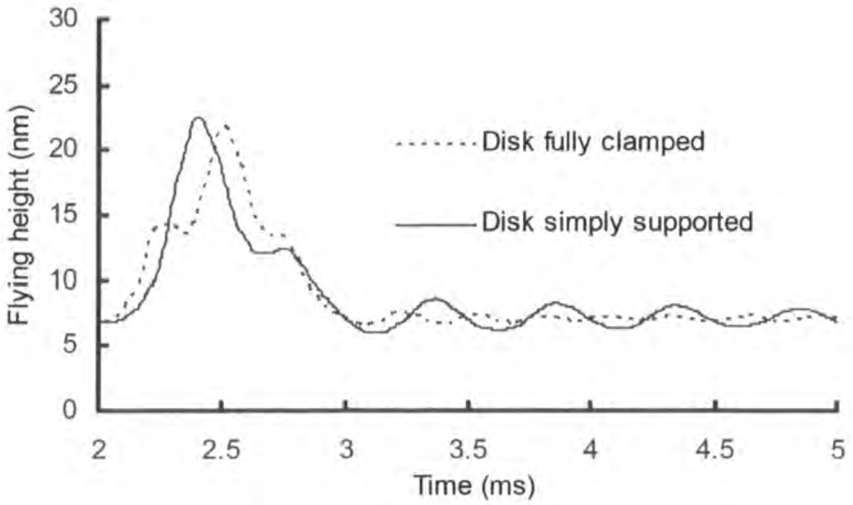

Fig. 4.48. Flying height during negative 200 G.

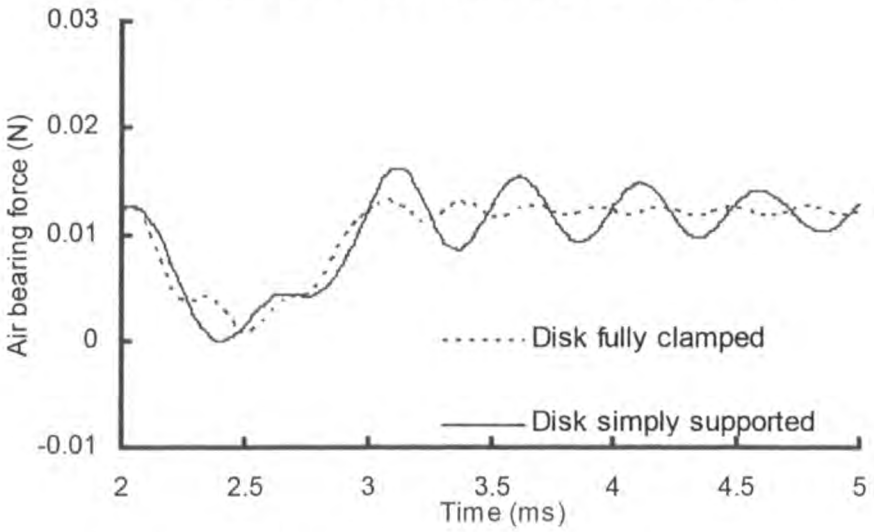

Fig. 4.49. Air bearing force during negative 200 G.

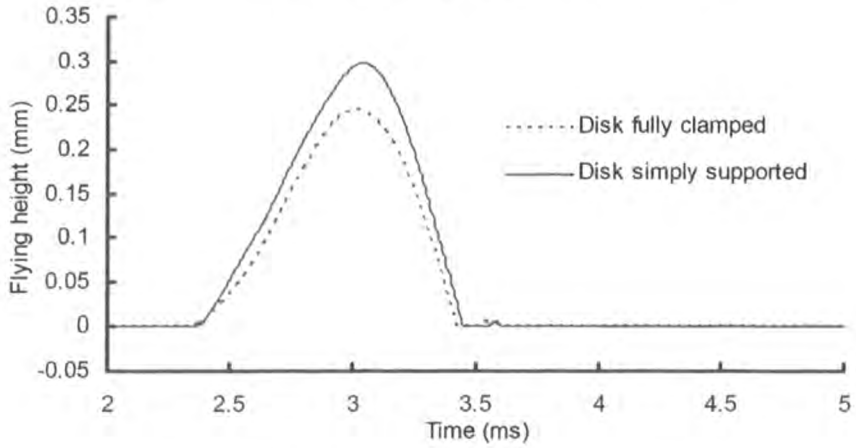

Fig. 4.50 Flying height during negative 400 G.

Figures 4.48-4.52 show the shock response for negative 200 G and 400 G shocks when the disk is fully clamped or simply supported. In Fig. 4.48, it can be seen that during the negative shock, the flying height increases from the steady flying height of 7 nm to reach a peak. This is because both the disk and the suspension bend up due to the negative shock, but the suspension being more flexible than the disk, has a tendency to lift off the disk. The lift-off of the slider causes the air bearing force decrease as shown in Fig. 4.49. Compare with the disk simply supported condition, both the maximum flying height and the amplitude of the oscillation of the flying height after the shock decrease for the disk fully clamped condition. For negative 200 G shock, the air bearing is able to support the negative load and retain the slider on the disk for both conditions. But for negative 400 G, as shown in Figs. 4.50-4.52, the air bearing is no longer able to support the negative load, so the slider lifts off from the disk and then slap on the disk for both conditions. Severe impacts between the disk and the slider are observed in Fig. 4.52. Compare with simply supported condition of the disk, both the flying height and the impact force decrease for the disk fully clamped condition as shown in Figs. 4.50 and 4.52. It is concluded that it helps to

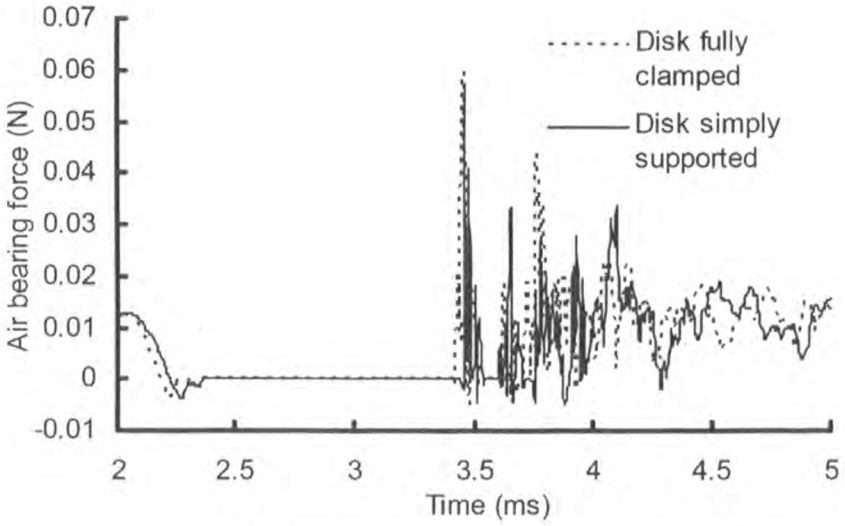

Fig. 4.51 Air bearing force during negative 400 G.

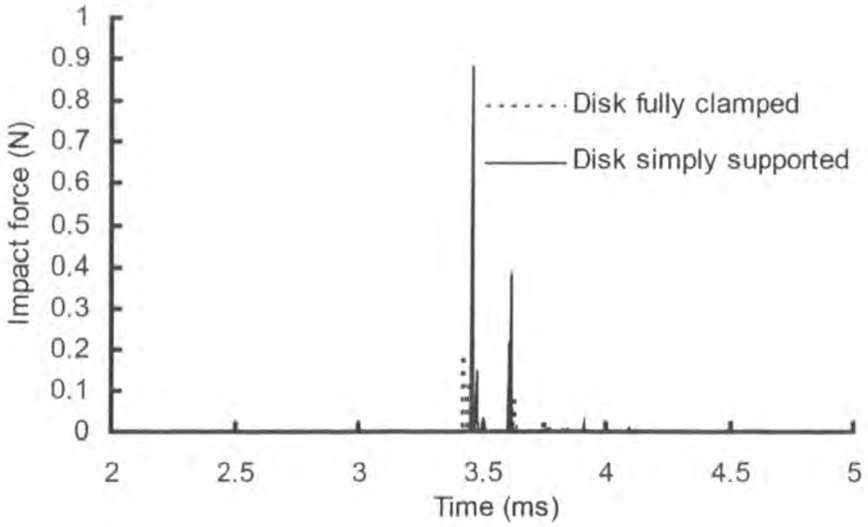

Fig. 4.52 Impact force between the disk and slider during negative 400 G.

decrease the shock response of the drive when the disk is more tightly clamped.

4.4.3 Shock Pulse Amplitude and Width Effects

To investigate the shock amplitude effect, the pulse width is kept at 1 ms and the amplitude of the shock pulse is varied from negative 200 G to negative 600 G. To investigate the shock width effect, the pulse amplitude is kept at negative 200 G and the width of the shock pulse is varied from 1.0 ms to 0.2 ms.

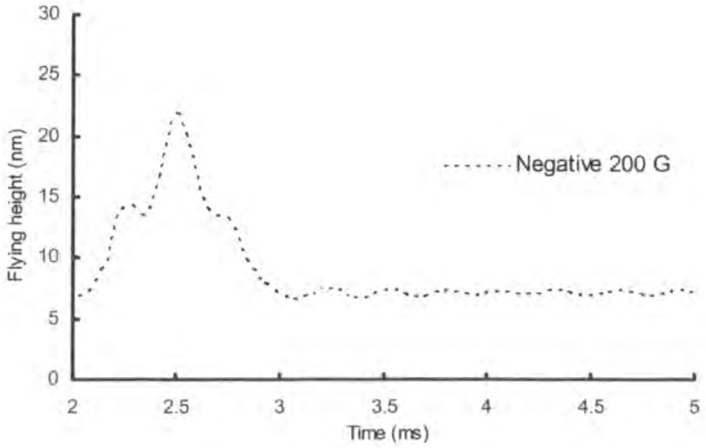

Fig. 4.53 Flying height during negative 200 G, 1 ms shock.

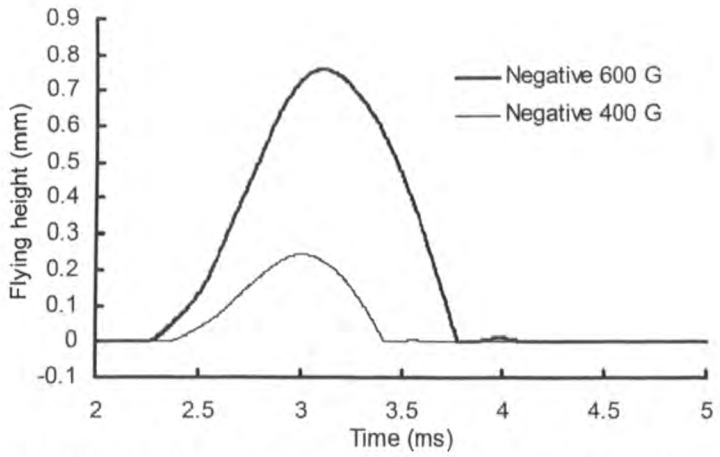

Fig. 4.54 Flying height during negative 400 G and 600 G shock.

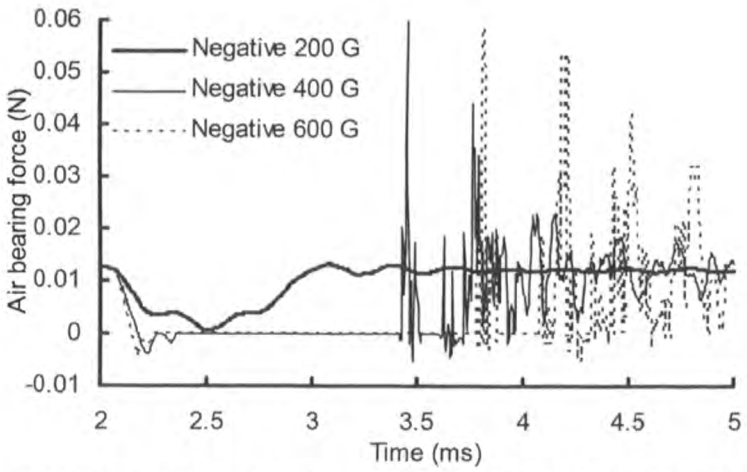

Fig. 4.55 Air bearing force during negative 200 G, 400 G and 600 G shock.

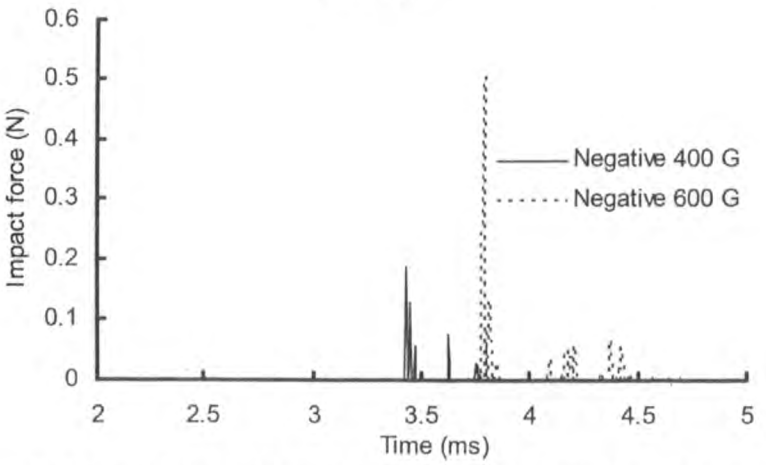

Fig. 4.56 Impact force between the disk and slider during negative 400 G and 600 G shock.

Figures 4.53-4.56 show the shock response for 200 G, 400 G and 600 G

shocks when the shock pulse width is fixed at 1.0 ms. In Figs. 4.53 and 4.54, it can be seen that during the negative shock, the flying height increases from the steady flying height of 7 nm to reach a peak. This is because both the disk and the suspension bend up due to the negative shock, but the suspension being more flexible than the disk, has a tendency to lift off the disk. The lift-off of the slider causes the air bearing force decrease as shown in Fig. 4.55. For negative 200 G shock, the air bearing is able to support the negative load and retain the slider on the disk. But for negative 400 G and 600 G shocks, as shown in Figs. 4.54-4.56, the air bearing is no longer able to support the negative load, so the slider lifts off from the disk and then slap on the disk. Head slap behaviors take place. Severe impacts between the disk and the slider are observed in Fig. 4.56. Compare with negative 400 G shock, both the flying height and the impact force during negative 600 G shock increase.

Figures 4.57-4.62 show the shock response for 1.0 ms, 0.6 ms and 0.2 ms shocks when the shock amplitude is fixed at negative 200 G. Fig. 4.57 shows that both the maximum flying height and the amplitude of the oscillation of the flying height after the shock increase with the decreasing of the shock pulse width from 1.0 ms to 0.6 ms.

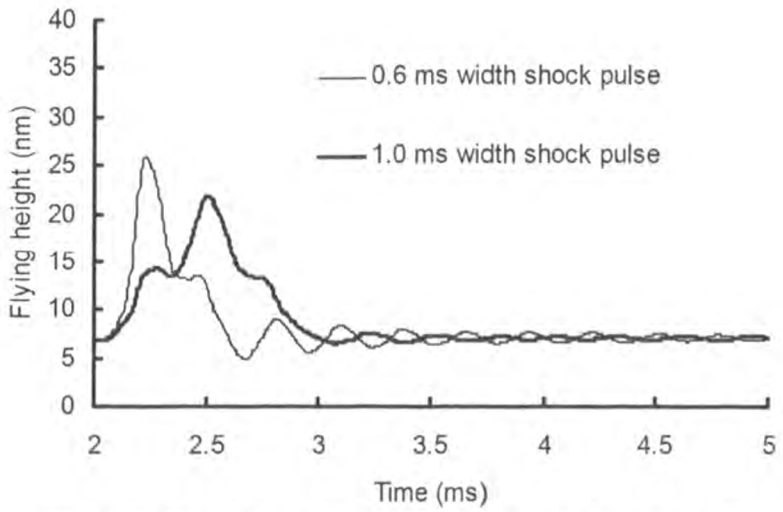

Fig. 4.57 Flying height during 1.0 ms and 0.6 ms shock.

Fig. 4.58 shows that the minimum air bearing force decreases and the amplitude of the oscillation of the air bearing force after the shock increases with the decreasing of the shock pulse width. The air bearing force achieves a minimum value of -0.0005 N for 0.6 ms shock in Fig. 4.58, which does not cause the air bearing to break. The air bearing is able to retain the slider on the disk. On the other hand, the air bearing is able to prevent the impact between the slider and the disk. The minimum flying height

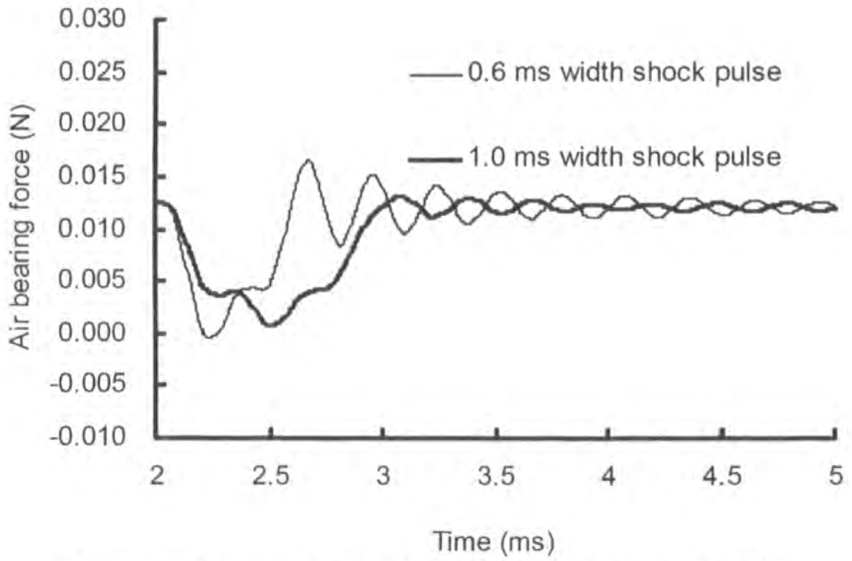

Fig. 4.58 Air bearing force during 1.0 ms and 0.6 ms shock.

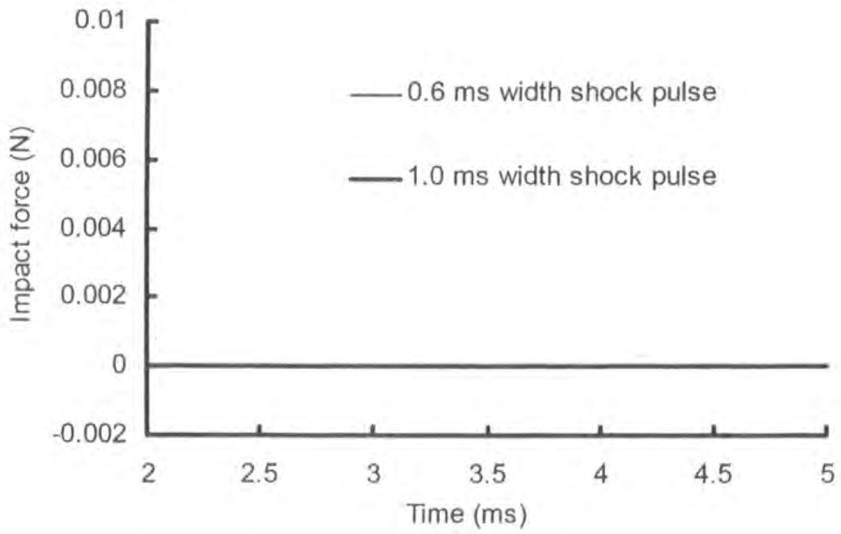

Fig. 4.59 Impact force during 1.0 ms and 0.6 ms shock.

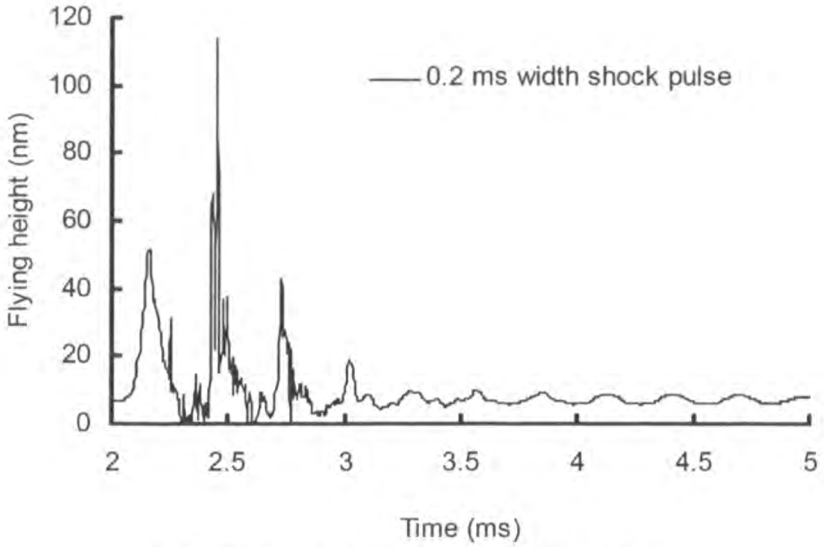

Fig. 4.60 Flying height during 0.2 ms shock.

for 0.6 ms shock in Fig. 4.57 goes beyond 5 nm. Therefore, there is no impact force exist as shown in Fig. 4.59 for 1.0 ms and 0.6 ms shock pulses.

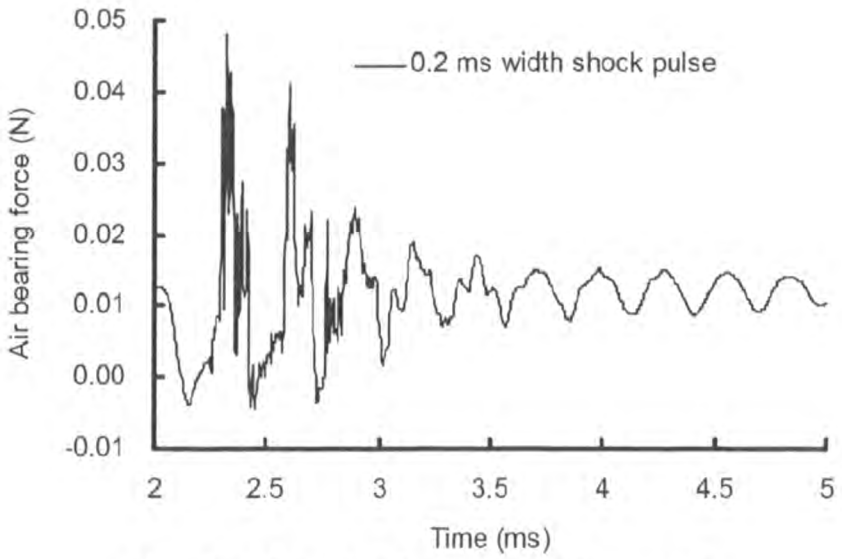

Fig. 4.61 Air bearing force during 0.2 ms shock.

Comparison between Fig. 4.57 and Fig. 4.60 shows that both the maximum flying height and the amplitude of the oscillation of the flying height after the shock increase much greater for 0.2 ms shock. In Fig. 4.59, the maximum air bearing force grows much bigger than that in Fig. 4.58 for 1.0 ms and 0.6 ms shock. The air bearing force

achieves a minimum value of -0.0045 N, which does not cause the air bearing to break. The air bearing is able to retain the slider on the disk. But the air bearing is not able to prevent the impact between the slider and the disk in this case. The minimum flying height for 0.2 ms shock in Fig. 4.60 goes below 0 nm. The impacts are observed as shown in Fig. 4.62.

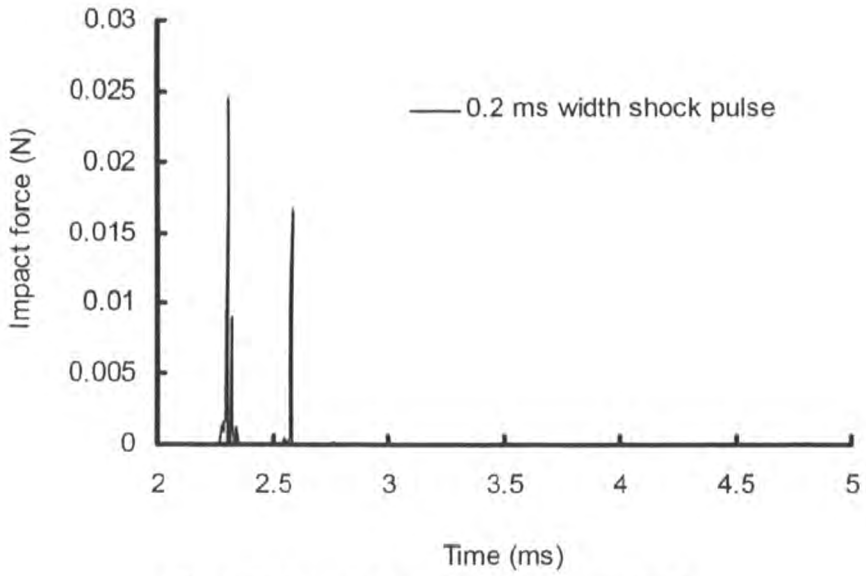

Fig. 4.62 Impact force during 0.2 ms shock.

4.4.4 Other Forces Affecting the Air Bearing

As the flying height is less than 6 nm, it has been shown experimentally that the air bearing may be affected by two forces: intermolecular forces (IMF) and electrostatic forces [88-90].

The intermolecular forces consist of a relatively short range repulsive force and a long range attractive force. They can generally be modeled by the Lennard-Jones' equation below.

$$F(r) = \left(-\frac{A}{6\pi r^3} + \frac{B}{45\pi r^9} \right) \Delta x \Delta y \qquad (4.15)$$

A and B are the effective Hamaker constants between the slider and the disk. r is the distance between the particles/molecules. $\Delta x\Delta y$ is the effective area of element on which the slider and the disk interact. From Eq. (4.15) it can be seen that Hamaker constant A determines the attrative components of intermolecular force. A typical range of this attractive force is about 10 nm [89] while the range of the repulsive force is around 0.05 nm.

The second force is the electrostatic force. It is an attractive force due to the electrostatic interaction between the disk and the slider [90]. It can be calcaulated as

$$F_{elec}(D) = -\frac{\varepsilon_0 k_e V^2 \Delta x \Delta y}{z^2} \tag{4.16}$$

Where ε_0 is permittivity constant (8.85 x 10^{-12} F.m^{-1}), k_e is dielectric constant (1 for air), V is potential difference between the slider and the disk.

4.4.5 Summary

In this section, the effect of disk clamping conditions on the operational shock response of HDDs is investigated numerically. It is found that the flying height grows when HDD is under greater amplitude of shocks. When the shock amplitude exceeds the shock tolerance, which is between 200 G and 400 G according to the results, the air bearing is unable to retain the slider on the disk. The slider flies off from the disk and then slaps on it. Moreover, it is found that the real clamping condition of disk is between simply supported and fully clamped and the shock response of the drive will decrease when the disk is more tightly clamped. So it helps to avoid the head slap with a more tightly clamped disk.

The shock pulse amplitude and width effects on the shock response of an operational HDD are also investigated numerically. A finite element model of the hard disk drive

is developed in ANSYS/LSDYNA. The sub-10 nm air bearing between the disk and the slider is modeled by nonlinear springs. The contact between the disk and the slider is also considered. The shock responses to shock pulses with varying amplitude from negative 200 G to negative 600 G and varying width from 1.0 ms to 0.2 ms are obtained. It is found that the shock response of the drive is sensitive to both the shock pulse amplitude and the shock pulse width. The flying height grows when HDD is under greater amplitude of shocks. Moreover, when the shock amplitude exceeds the shock tolerance, which is between 200 G and 400 G according to the results, the air bearing is unable to retain the slider on the disk. The slider flies off from the disk and then slaps on it. The head slap can generate particles on the disk medium and cause pollution problems. The actual shock tolerance for this HDD is measured in drop test. The slider head is programmed to scan the disk for hard error after each test. It is observed that the disk damages mostly at 300 G amplitude. So this numerical model can be applied to predict the shock tolerance during the design stage. It is also found that both the maximum flying height and the amplitude of the oscillation of the flying height after the shock increase with the decreasing of the shock pulse width. During the short width shock pulse, even though the air bearing is able to retain the slider on the disk and prevent the head slap behavior, the impact between the slider and the disk is still likely to happen. This may attribute to the disk's vibration and will be investigated further. In order to prevent such impact to increase the shock resistance of the HDD further, the short width shock pulse should be avoided by providing padding or isolation system for the HDD.

CHAPTER 5

EXPERIMENTAL STUDIES ON SHOCK RESPONSE OF HDDs

5.1 Introduction

In this chapter, section 5.2 investigated the head slap behaviors of an HDD in the linear drop tests. The effect of inclination angle on the head slap for the small form factor drive is studied in section 5.3. The effect of clamping condition on the shock response of the disk in the small form factor HDD S1 is evaluated experimentally and numerically in section 5.4. A new way of measuring the shock response of HAA of small form factor HDD by using strain gauge is proposed in the section 5.5.

5.2 Fragility Test on Head Slap in The Linear Drop Tests

In the tests, the shock tester and high speed camera are used. The Lansmount shock tester with dual mass shock amplifier (DMSA) is capable of producing up to 10000 g half sine acceleration pulses. The HDD is subjected to the shocks of half-sine pulse with different durations and amplitudes. The head slap behaviors are monitored and captured by using the high speed video camera. The head slap of HDD is sensitive to both amplitude and duration of the half-sine acceleration pulse as the experimental results show.

5.2.1 Experimental Set-up of Linear Drop Test on HDDs

For the linear drop test of HDDs, experimental set-up shown in Fig. 5.1 will be used. This set-up is composed of drop tester, LDV, high speed video camera and

accelerometers. Accelerometers measure the input accelerations, and LDV (Laser Doppler Vibrometer) measures the motion of arm, suspension. Through the high speed video camera, observation of the slider behavior after an external shock can be achieved.

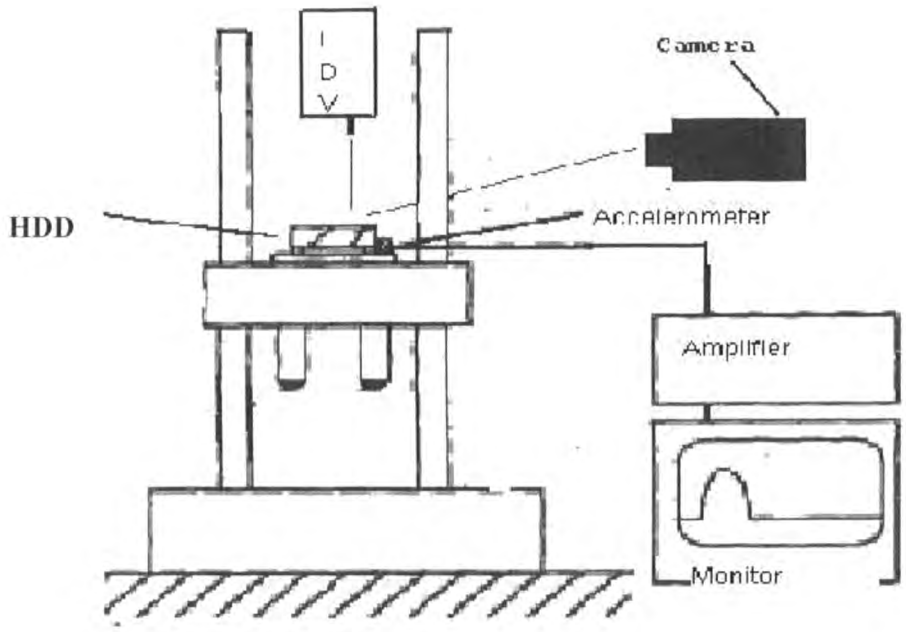

Fig. 5.1. The experimental set-up on linear drop test

Model 65/81 Dual Mass Shock Amplifier (DMSA) is used for programming very high acceleration, short duration shock pulses into lightweight specimens. It is shown in Fig. 5.2. It consists of a closely guided secondary shock table and a base, which is bolted to the drop table of the 65/81 shock tester machine. The test specimen is mounted on the secondary shock table and programming material is placed between the secondary table and its base. An appropriate trapezoid pulse is programmed into the shock tester machine by the impact between the table plunger and trapezoid programmer, causing the secondary table to impact the programming material on its base, producing the desired results. Specimen mounting area is 30.4 cm x 30.4 cm,

maximum test specimen weight is 25 lbs, maximum acceleration is about 10,000g. The DMSA includes the mounting hardware to secure it onto the shock machine table. It works together with the shock machine to generate a Half Sine Shock Pulse and Duration range of 0.1 to 2.0 msec. Fig. 5.3 showed one piece of the programming material for DMSA.

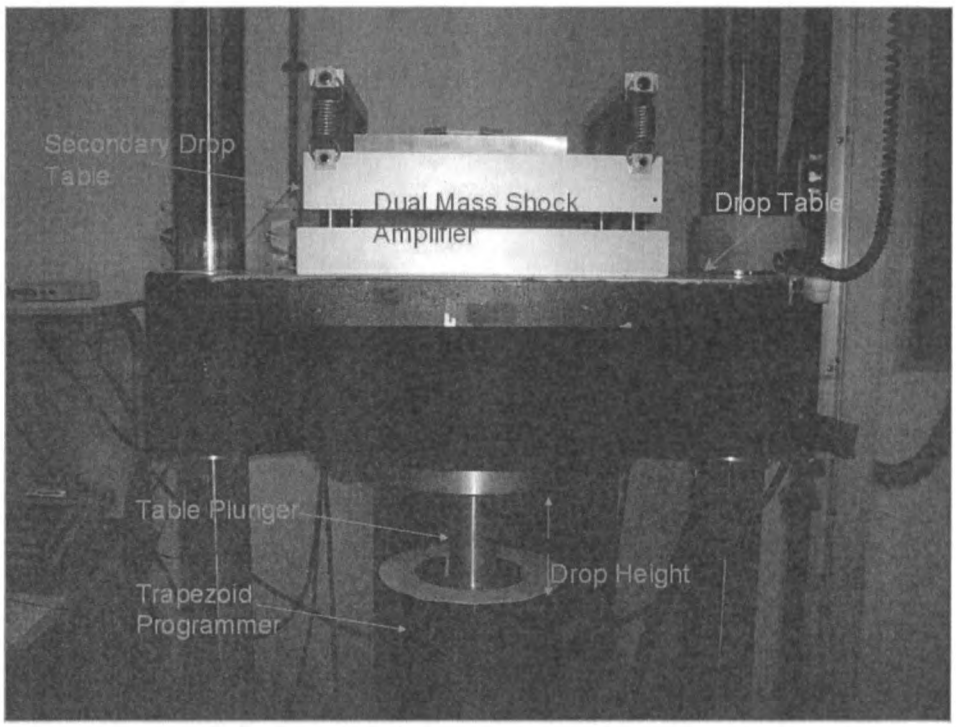

Fig. 5.2. Drop tester with the DMSA

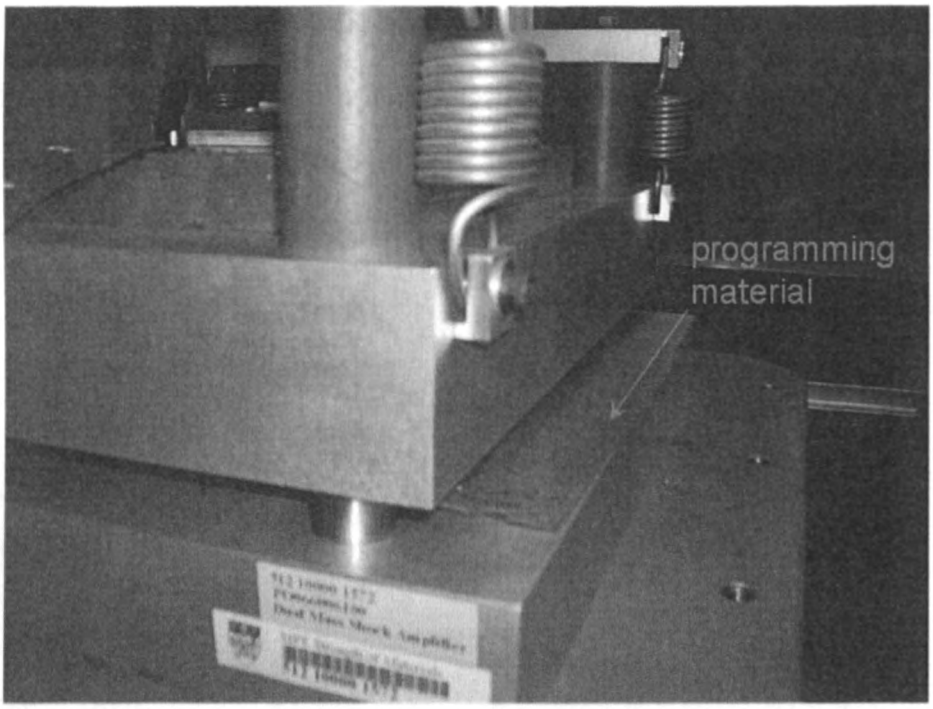

Fig. 5.3. Programming material of DMSA

In the linear drop tests, the HDD was clamped on the on the secondary shock table as Fig. 5.4 shows. The acceleration of the secondary drop table and the drop table were measured by accelerometer A and accelerometer B respectively, as Fig. 5.5 shown.

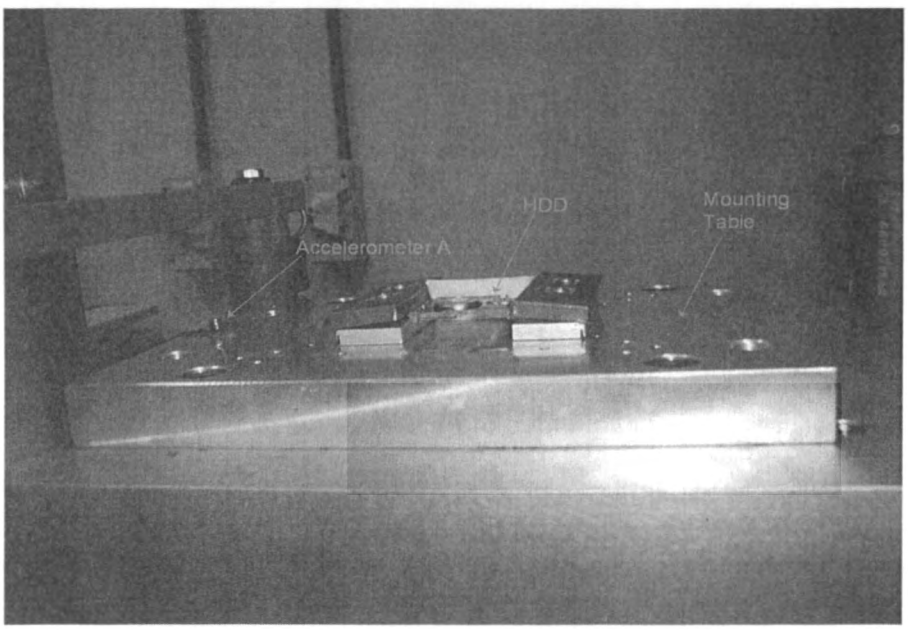

Fig. 5.4. The mounting of HDD

Fig. 5.5. The measurement spots of accelerations

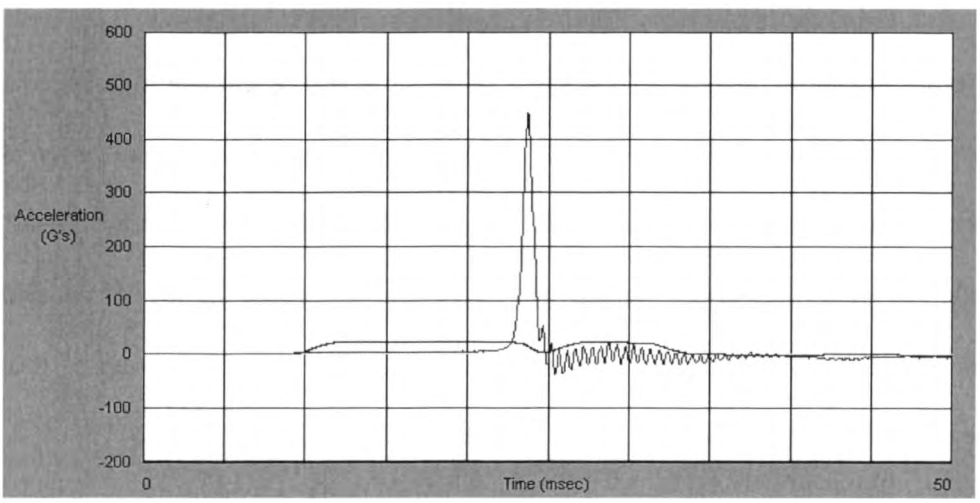

Fig. 5.6. The accelerations pulses produced by shock tester with DMSA

Fig. 5.6 showed the acceleration pulse of the secondary drop table (peak one) and acceleration pulse of the drop table (flat one) when the drop height was 5 cm. The half sine acceleration pulse was 450 g and 1.5 ms. When increasing the drop height to 10 cm, we got the half sine shock pulse of 1000 g and 0.68 ms duration as Fig. 5.7 shows.

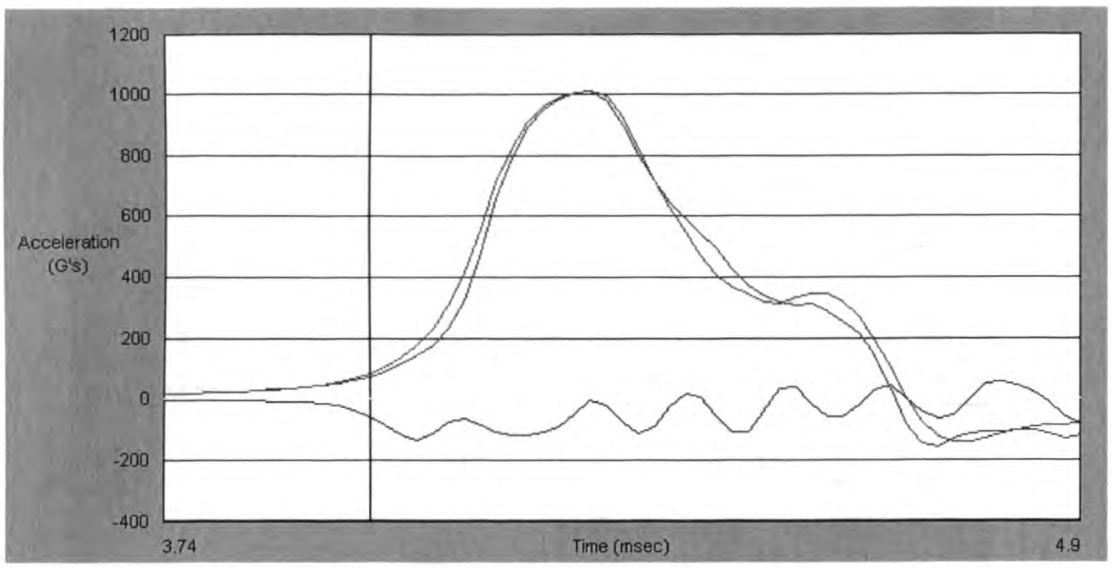

Fig. 5.7. The acceleration pulse of 10 cm drop height

In order to capture the lift off the slider in the drop test, a suitable high speed video camera is needed. The 1024 PCI FASTCAM-X high speed camera was chosen after a series of demos and comparisons with other high speed cameras. In the linear drop tests, 1024 PCI high speed camera was successful to capture the lift off the slider in both negative shock drop test and positive shock drop test. The set-up of the high speed camera in the experiments was showed in Fig. 5.8a and Fig. 5.8b.

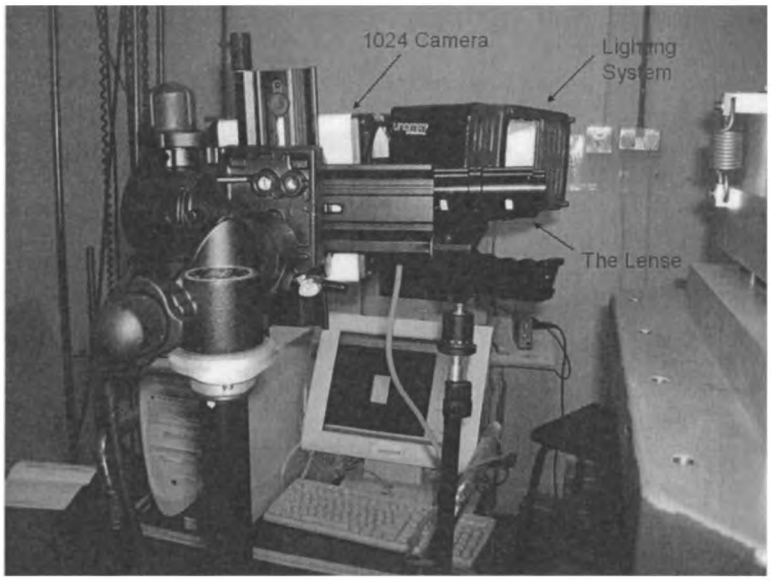

Fig. 5.8a The set-up of high speed camera

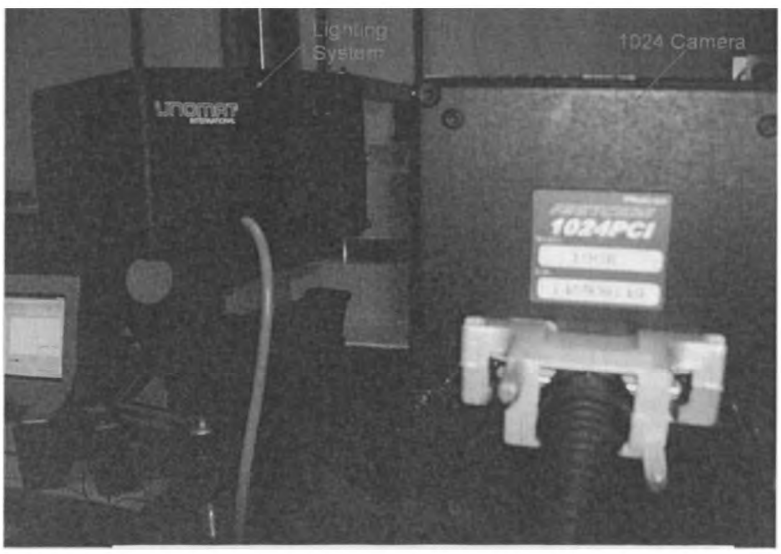

Fig. 5.8b The set-up of high speed camera

In the linear drop experiments, the drop height was 8 cm and the shock pulse produced by drop tester was 800 g and 1 ms. The 10000 fps at 256*256 resolution was used for the high speed camera. The HDD was firstly mounted on the secondary drop table upside down as Fig. 5.4. The camera captured the lift-off of the slider clearly. From the pictures drawn from the video as Fig. 5.9, we observed "head slap" three times from 1 to 5, 6 to 10 and 11 to 15, respectively.

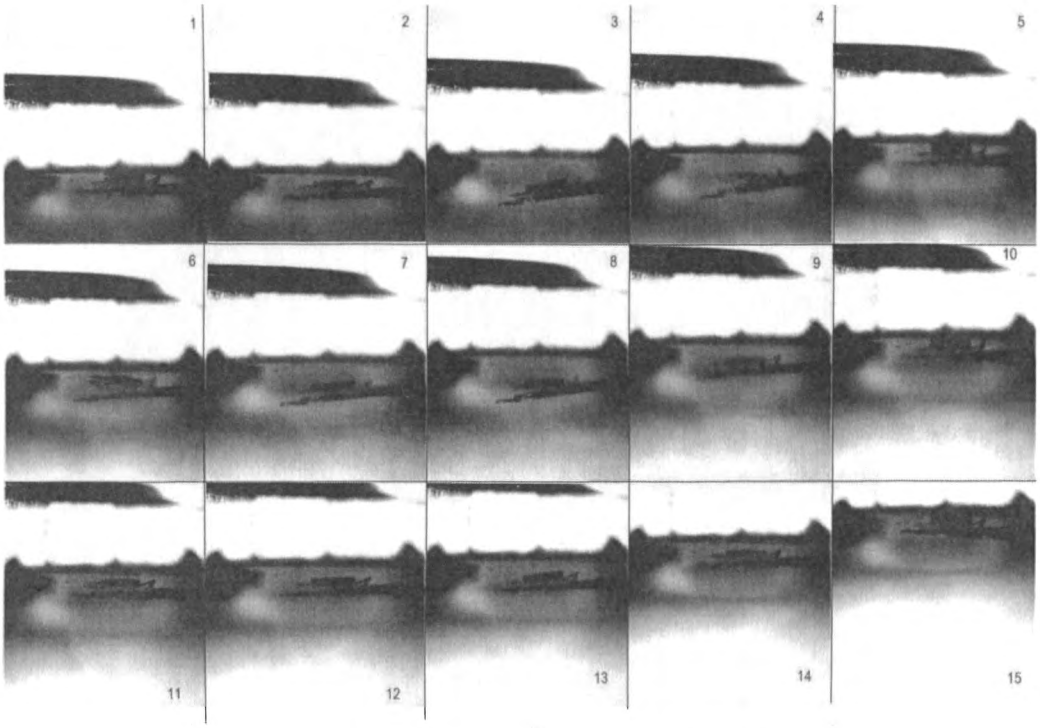

Fig. 5.9. The lift-off of slider in test one

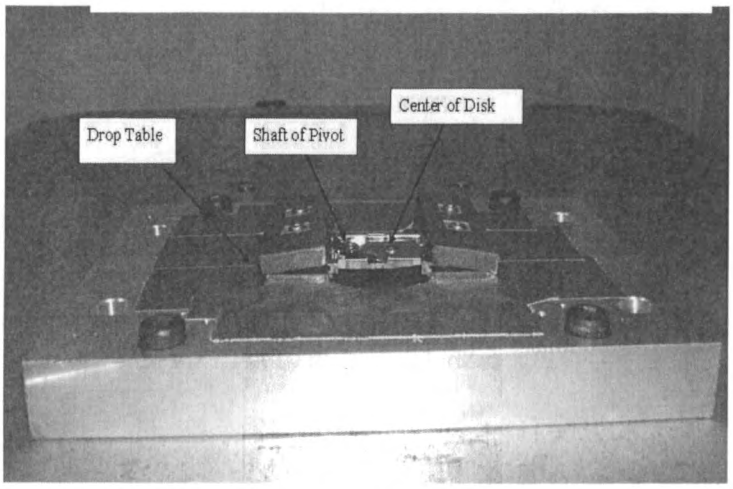

Fig. 5.10 The mounting of HDD in test two

In drop test two, the HDD was clamped as Fig. 5.10 showen. The pictures from the video captured by the high speed camera were shown in Fig. 5.11. The "head slap" also took place three times.

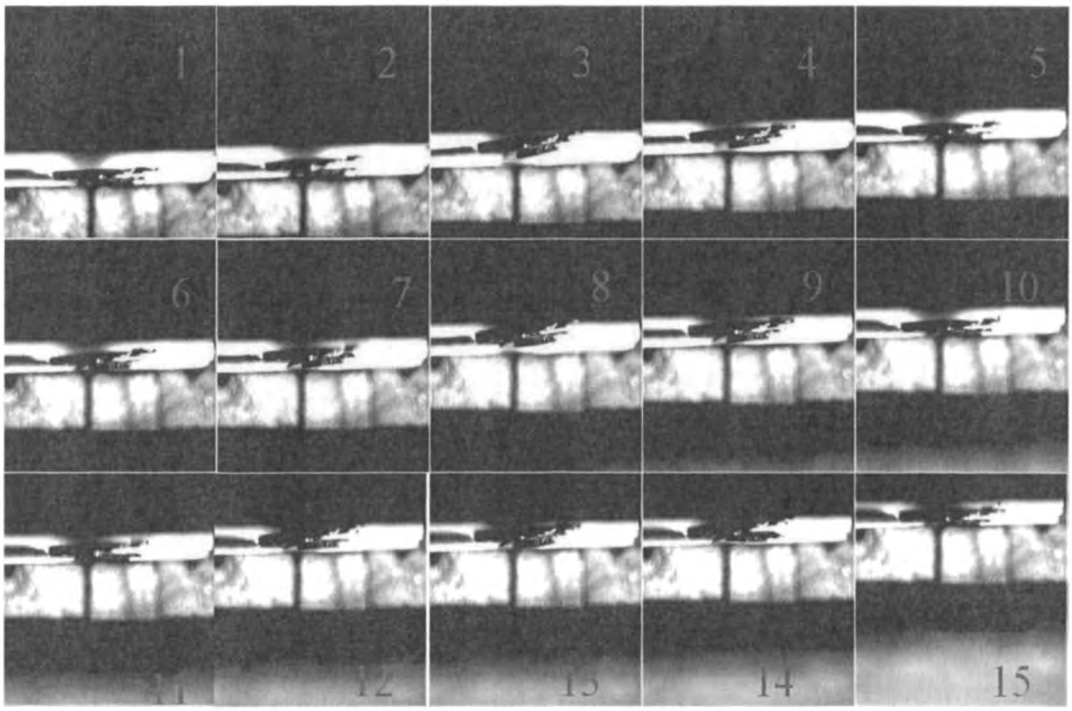

Fig. 5.11. The lift-off of slider in test two

5.2.2 Fragility Test results on Head Slap

In the experiment, pulses with different amplitudes from low to high g level, and different durations from long to short will be applied to the HDD. The lift-off of the slider will be monitored and captured by High Speed Video Camera. A fragility curve will be determined according to the experimental results in an A-D (amplitude-duration) coordinate. From the curve, the combinations of amplitude and duration, which can cause the lift-off of the slider, will be decided. The results from experiments will be compared with the results from simulations.

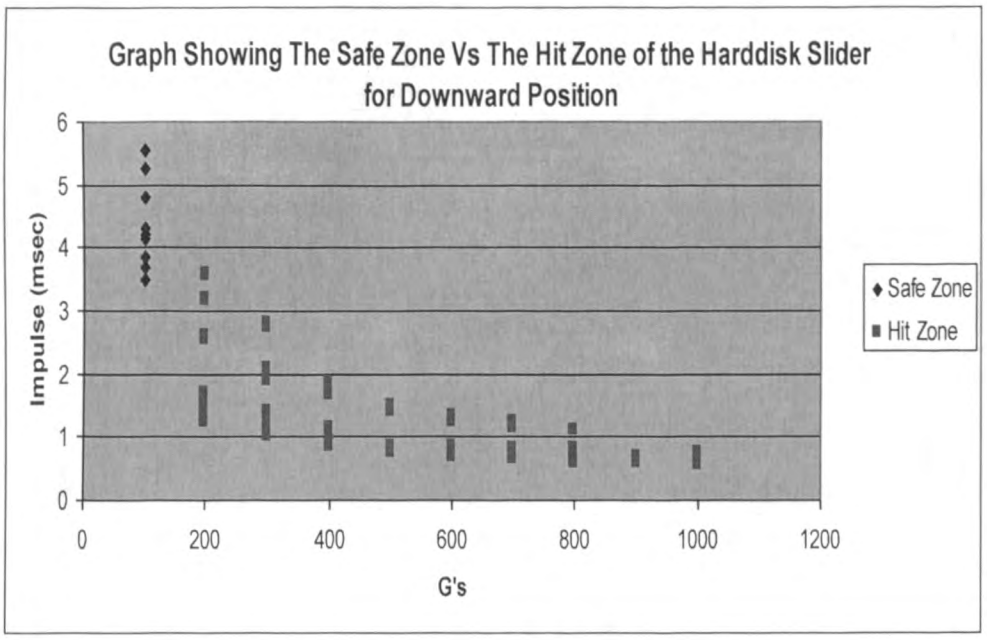

Fig. 5.12 Graph of fragility points for downward slider

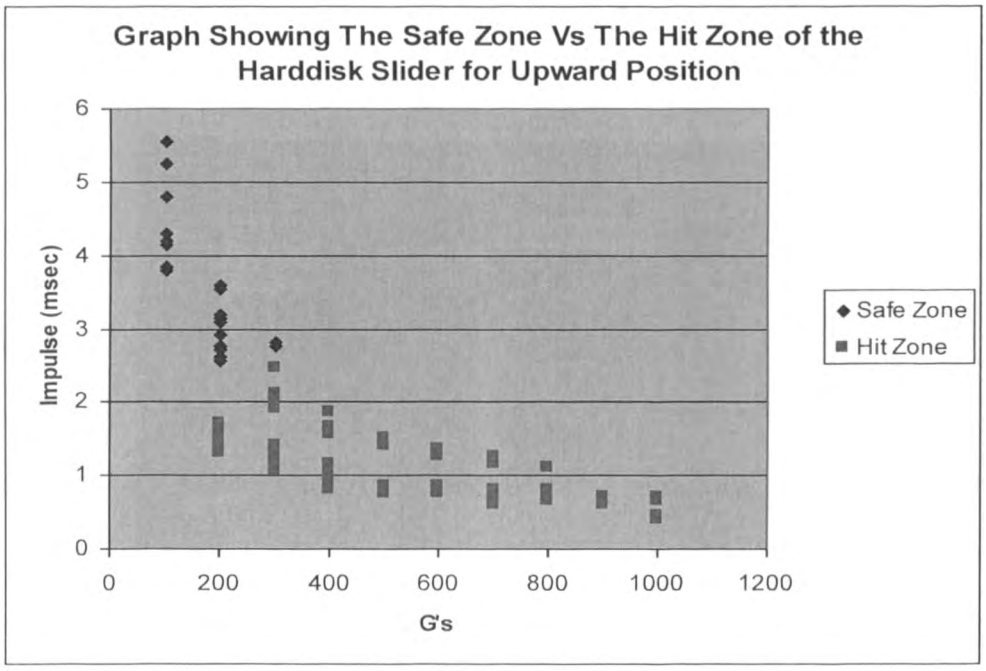

Fig. 5.13 Graph of fragility points for upward slider

According to the experiments have been done, the result of fragility test on head slap behavior is illustrated in Fig. 5.12 and Fig. 5.13. The point in safe zone means that head slap did not take place when the HDD is subjected to the shock pulse that point

presents. The point in hit zone shows that head slap happened when the disk takes that point's shock pulse. For Fig. 5.12, the HDD is mounted on the drop table upside-down. The slider which is close to the drop table is video-monitored. For Fig. 5.13, the HDD is mounted on the drop table normally. The upper slider can be monitored as Fig. 5.11 shown. Compare Fig. 5.12 and Fig. 5.13, we can see there is no head slap when amplitude is 100 G. But for amplitude of 200 G, at the same duration around 3 ms, only the slider close to the drop table sees the head slap. It can be concluded that head slap is easier to happen for the HAA in downward position. This is agreeable with the numerical results in section 4.4.

From both Fig. 5.12 and Fig. 5.13, we can see that at the same duration points, the head slap is easy to take place at points with higher amplitude. From Fig. 5.13, at the points with same amplitude, the points with shorter duration make the head slap easier. So the head slap is more like to take place under the shock with shorter duration and higher amplitude. This is also correlated with the conclusion from simulation results in section 4.4.

5.2.3 Fragility Assessment on Head Slap with Random Shock Pulse

In most of the real impact scenarios, the shock loading can not be represented by a half –sine pulse loading. Newton suggested that the item fragility is determined by the critical acceleration and critical velocity [92]. This definition is based on the damage boundary theory as shown in Fig. 5.14. The item fragility is measured by two factors: critical velocity and critical acceleration. The critical velocity represents the velocity change (which can be related to drop height) below which no damage could possibly occur, regardless of the magnitude of the peak pulse acceleration. The critical acceleration represents the acceleration above which the product will be most likely damaged.

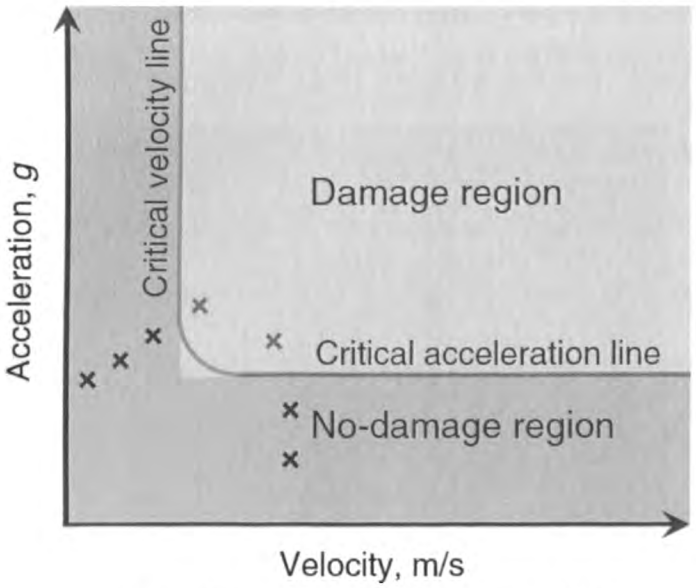

Fig. 5.14. Damage boundary curve [92]

The item fragility tests should be performed using rectangular pulses [91] as it provides an upper bound by comparison of the shock spectrum curves for various pulse shape as shown in Fig. 5.15. In real test, the rectangular pulse may be approximated by a symmetric trapezoid. To establish the complete damage boundary, tests at constant velocity and increasing shock amplitude will establish the bottom line of the damage boundary. A second sequence of tests at constant amplitude while increasing velocity will establish the left hand portion of the damage boundary. This damage boundary will provide conservative results.

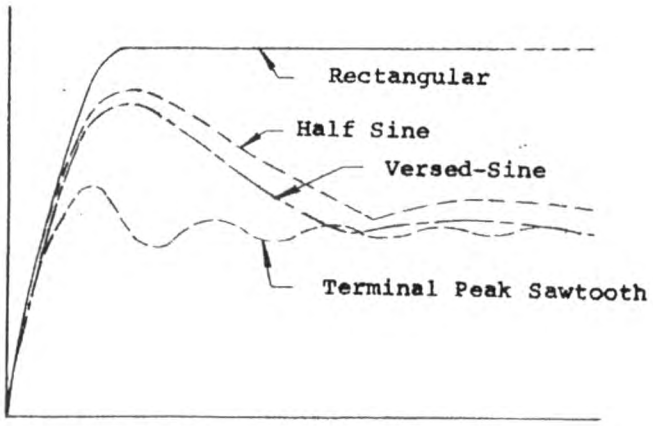

Fig. 5.15. Shock spectra for various pulses [91]

5.2.4 Constrained Drop Testing (Shock Table Test) Vs. Free Drop Testing (Drop Test)

It should be noted that the constrained drop testing (shock table test) in Fig. 5.1 or Fig. 5.2 is an HDD industrial practice. Another test method is free drop testing (drop test). The traditional free drop testing is to drop the specimen from a certain height with a drop tester. The advantage of this method is that it can duplicate the real-life impact state. The disadvantage is that the test repeatability cannot be guaranteed due to the difficulty of controlling the orientation of the object at impact and measuring it instrumentally. Moreover, free dropping test is not suitable to the shock reliability test of individual component. Constrained drop testing can overcome the above draw-backs. That's why it is practiced in HDD industrial.

However, the constrained drop testing is a simulation of a real-life drop impact process. In order to fully mimic the real free dropping test conditions, the shock table test method should allow the specimen to rotate freely and the shock duration should be much smaller compared to the contact period of real drop [93]. However, when the hard disk drive rotates freely, the measuring instruments like LDV and high speed camera cannot be used to measures the motion of arm, suspension and disk.

5.3 Shock Response of HDDs to Inclined Shock Test

In all previous experimental and numerical studies, the shock was applied to the drive linearly, which is the situation that the shock is perpendicular to the surface of the disk in the drive. In real situation, the drive may drop on the ground with an inclination angle; the shock is applied to the drive with an inclination angle and is not perpendicular to the surface of the disk.

In order to improve the shock resistance of the disk drive and to avoid the head slap, the effect of inclination angle on the head slap behavior was investigated experimentally. A small form factor HDD was clamped on an inclined surface of a fixture on the guided drop test platform during the drop test. The inclination angle of the drive during drop test was taken into consideration. A better understanding of the dynamic characterization of small form factor hard disk drive is achieved.

5.3.1 Experimental Set-up

Fig. 5.16 shows a schematic diagram of the experimental setup for evaluating the effect of the inclination angle on the shock performance of a small form factor HDD. Fig. 5.17 shows the photograph of the test. A fixture is designed to clamp the HDD with the top cover removed on the shock table platform with different inclination angles. The left end of the fixture is capable of rotating. By using different block to raise the right end of the fixture, the desired inclination angle is achieved. In the test, the inclination angle was 0 degree, 30 degree and 60 degree, respectively. For each inclination angle, the HDD was fixed with the top cover facing up and with the top cover facing down. The test equipment includes the Lansmount Drop Tester equipped with Dual Mass Shock Amplifier (DMSA) capable of producing the high amplitude and shock duration shock pulses, the 1024 PCI FASTCAM-X high video camera system capable of recording 10,000 frames per second, and B & K accelerometer attached to the fixture to record the amplitude and duration of the shock load. The magnitude and duration of the shock pulse were controlled by changing the height of the fall and material of the pads below the DMSA.

In the test, the HDD was firstly fixed with the top cover facing up on the shock table when the inclination angle is 0 degree. The shock table was raised to a proper height according to the shock level and then released. The behavior of the sliders was

recorded using high speed video camera when the shock was applied and the actual shock pulse was measured by the accelerometer in the mean time. The HDD was changed to top cover facing down and the measurement was repeated when the inclination angle was remained at 0 degree. The same procedure was repeated when the inclination angle was 30 degree and 60 degree, respectively.

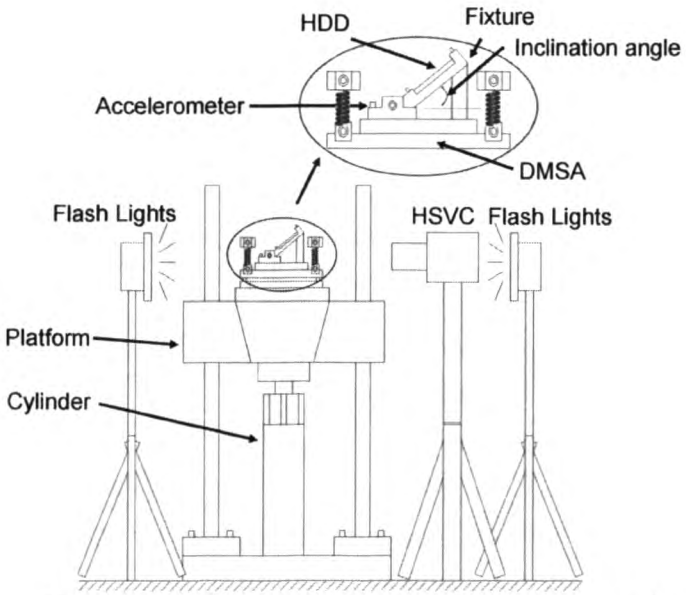

Fig. 5.16. Schematic diagram of the experimental setup

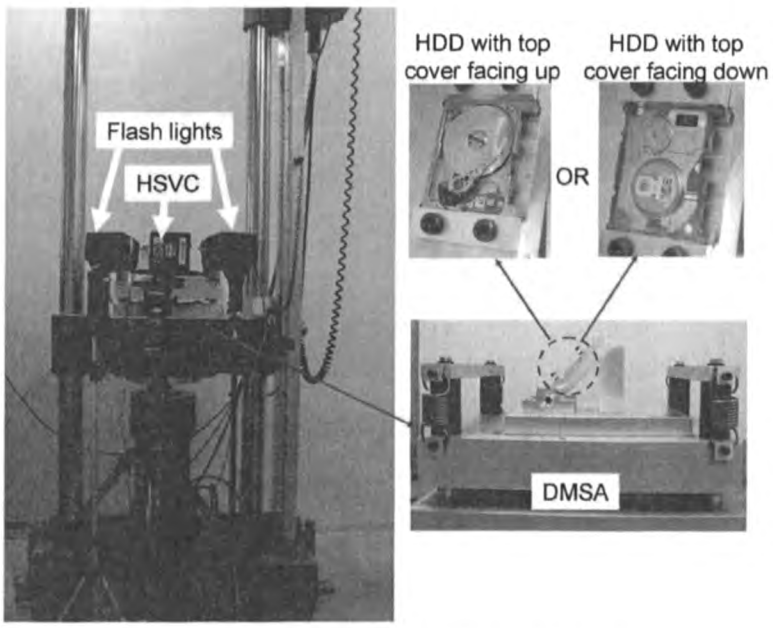

Fig. 5.17. Photograph of the experimental setup

Fig. 5.18 shows that the shock pulse was applied in the direction from the base plate to the cover when the HDD was clamped with the top cover facing up. The acceleration pulse can be decomposed into the acceleration perpendicular to the disk a_{pe} and the acceleration parallel to the disk a_{pa}. For different inclination angle α, the amplitudes of a_{pe} is A_{pe}, and $A_{pe} = A \times \cos\alpha$, A is the amplitude of the acceleration pulse in Figure 3. It is easy to see that the amplitude of a_{pe} at 0 degree $A_{pe}(0)$ equals A, due to $A_{pe}(0) = A \times \cos 0 = A$. So $A_{pe} = A_{pe}(0) \times \cos\alpha$.

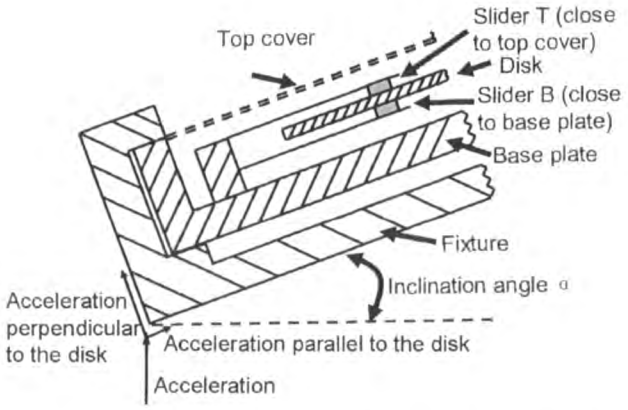

Fig. 5.18 The HDD clamped with top cover facing up

In Fig. 5.18, the slider close to the top cover (Slider T) was on the top surface of the disk and the slider close to the base plate (Slider B) was below the disk. When the HDD was clamped with the top cover facing down, the shock pulse was applied in the direction from the top cover to the base plate and can be also decomposed into the acceleration perpendicular to the disk surface and the acceleration parallel to the disk surface. The slider close to the top cover (Slider T) was below the disk surface and the slider close to the base plate (Slider B) was on the top surface of the disk when the top cover of the HDD was facing down.

5.3.2 Results and Discussion

Fig. 5.19 shows the shock pulses measured by the accelerometer (Figure 1) attached to the fixture in the tests. In all the tests, the shock pulse was remained almost identical by dropping the platform from the same height and putting the same material of the pads below the DMSA. The shock pulse can be approximated by a half sine pulse with amplitude A of 250 G and duration d of 1 ms [16].

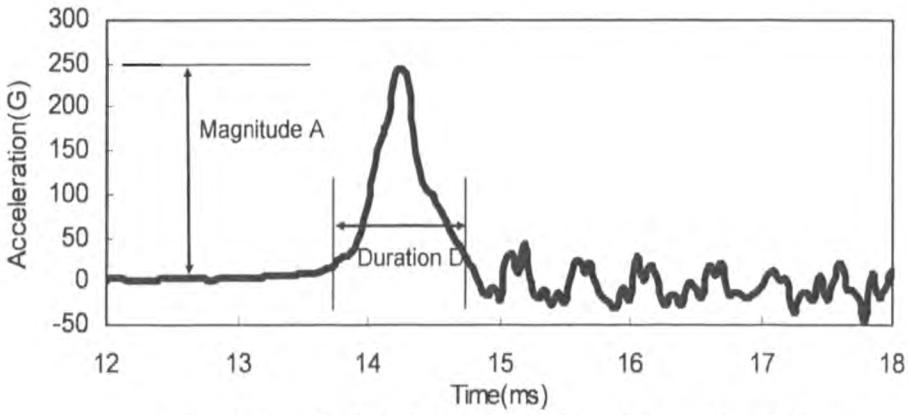

Fig. 5.19. Shock pulse measured by the accelerometer

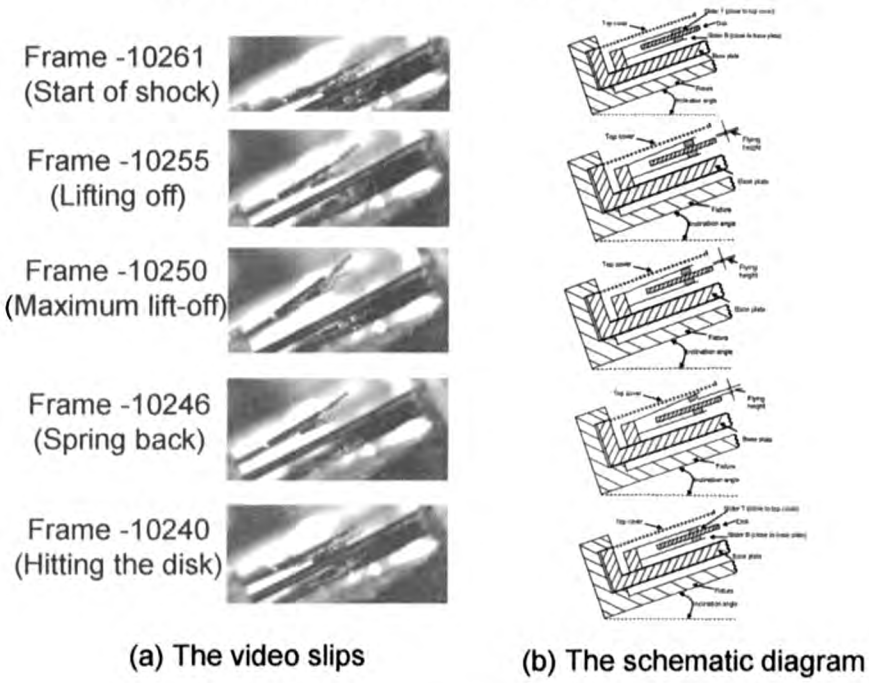

Fig. 5.20. The sequence of head slap of the slider

Both the slider T and the slider B were video recorded into the same frame. Fig. 5.20 illustrates the sequence of head slap of the slider T captured by the high speed video camera when the HDD was clamped with top cover facing up. Sequence began with the slider resting on the disk surface (frame -10261). After the applying of the shock pulse, the sliders were lifting off from the disk (frame -10255) and reaching the maximum flying height (frame -10250). Then the sliders were springing back (frame -10246) and slapping on the disk (frame -10240). More lift-offs happened, which are not shown here.

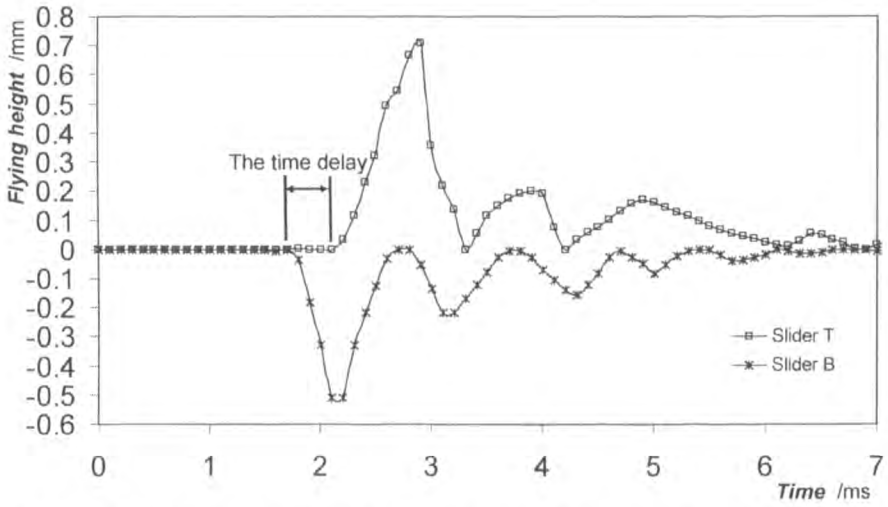

Fig. 5.21 The flying height of the sliders with top cover facing up when $\alpha = 0^{\circ}$

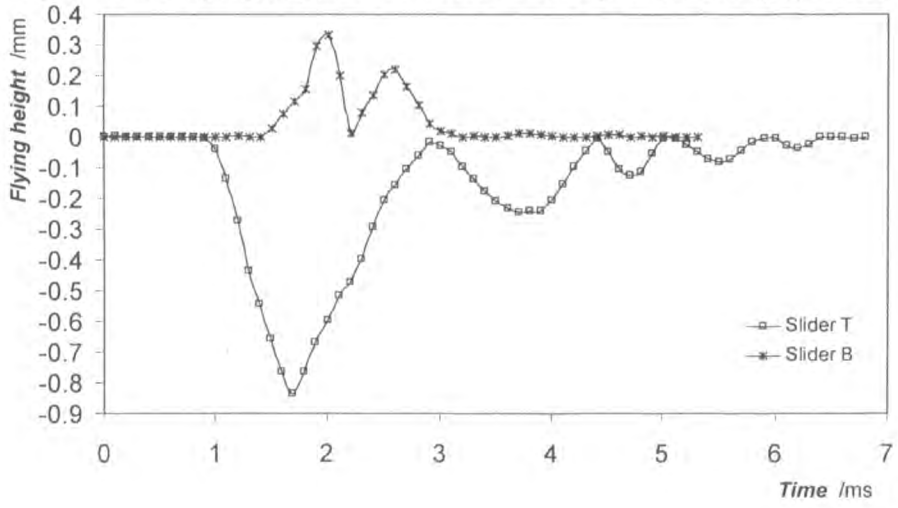

Fig. 5.22 The flying height of the sliders with top cover facing down when $\alpha = 0^{\circ}$

The flying height of the slider illustrated in Fig. 5.20, is the displacement of the center of the slider relative to the disk surface. Fig. 5.21 and 5.22 show the flying height of the slider during a drop with top cover facing up (Fig. 5.21) and a drop with top cover facing down (Fig. 5.22), respectively, when the inclination angle is 0 degree. Fig. 5.23 and Fig. 5.24 show the flying height of the slider when the inclination angle is 30 degree. Fig. 5.25 and Fig. 5.26 show the flying height of the slider when the inclination angle is 60. In Fig. 5.21, the slider B first lifted off from the disk at about 1.7ms. It quickly rose to its first peak of about 0.5mm within 0.4ms. It then slowly heading back to the disk and slapped the disk in 0.6ms at 2.7ms. It instantly rebounded from the disk surface with a second lift-off of about 0.2mm.

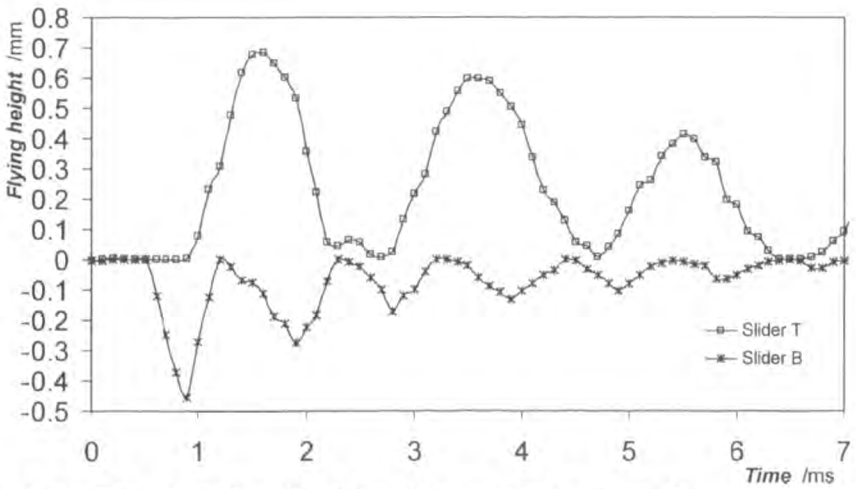

Fig. 5.23. The flying height of the sliders with top cover facing up when α =30°

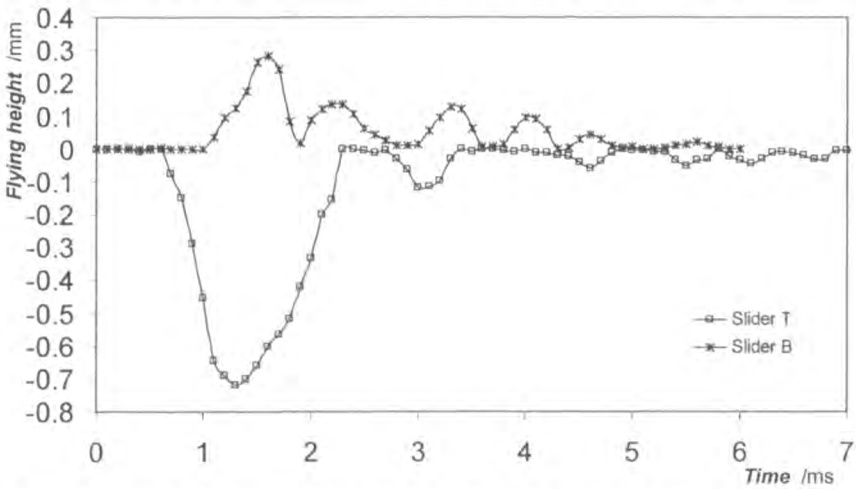

Fig. 5.24.The flying height of the sliders with top cover facing down when α =30°

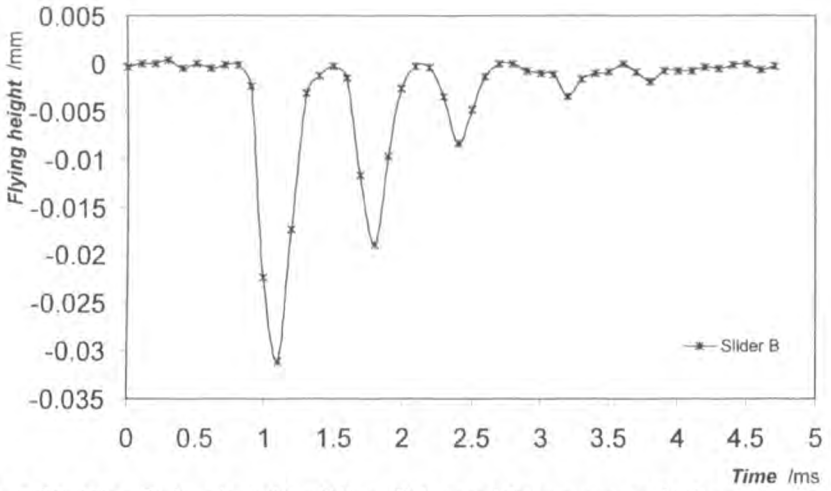

Fig. 5.25. The flying height of the sliders with top cover facing up when $\alpha = 60^{\circ}$

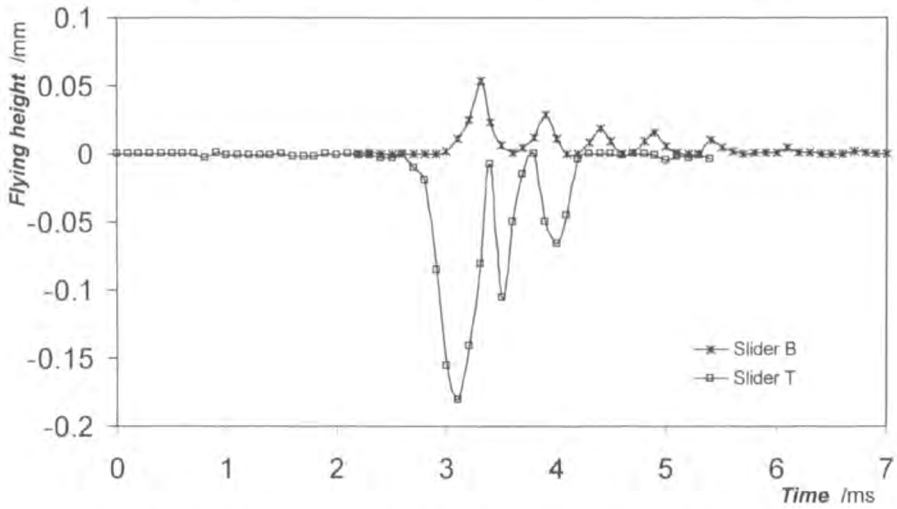

Fig. 5.26. The flying height of the sliders with top cover facing down when $\alpha = 60^{\circ}$

It can be observed that head slaps happened in all the drop tests. In Fig. 5.25, only the slider B, which was below the disk when the top cover of the HDD was facing up, lifted away from the disk. When both sliders lifted off in other figures, the slider on the top surface of the disk lifted away from the disk approximately 0.4 ms later than the slider below the disk. This is due to the inertia of the Head Disk Assembly (HDA), the initial acceleration pushes the slider on the top surface of the disk toward the disk and pushes the slider below the disk away from the disk. During the free fall, the upper slider and the lower slide are held tight to the disk by preloading. At collision, with inertia, both the disk and the two sliders continue to move downward, while the

spindle was suddenly seized by the clamp. As the disk reaches its lowest point in the vibration, the lower slide breaks free from disk and continue its downward movement with albeit lower and lower speeds. The disk will spring back in the umbrella mode, and brings upward with it the upper slider. As the disk reaches the highest point, the upper slider then lift off from the disk and continue its upward movement, leaving the disk to vibrate downward again. It is noted that the period of the disk medium is about 2900Hz from chapter 4. Therefore the period of the primary umbrella vibration mode is about 1/2900Hz = 0.33ms, which is close the delay of about 0.4ms observed in all figures. It can be seen that the disk motion can cause the slider to lift off. The vibration of the disk plays an important role in head slap behavior. In all the tests, the sliders rebound and spring back. This movement which decreases gradually due to collision resulting in energy loss is repeated a few times.

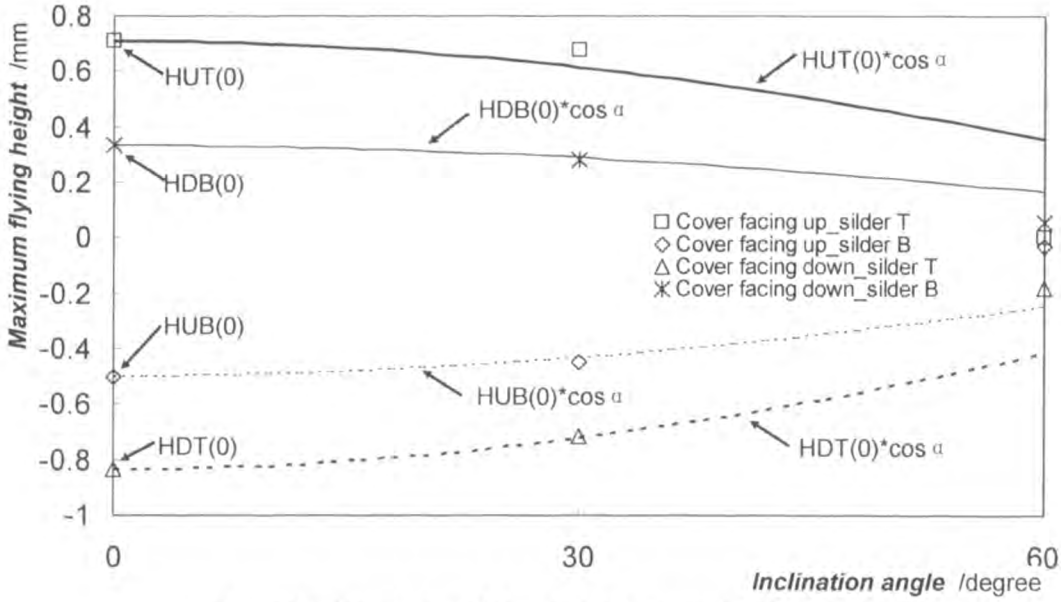

Fig. 5.27. Maximum flying height versus inclination angle

Fig. 5.27 shows the maximum flying height of the sliders versus the different inclination angles in the tests. The flying height of the sliders at 0 degree are denoted as HUT(0), HDB(0), HUB(0) and HDT(0), respectively. The curves obtained by

multiplying the maximum flying height of the sliders at 0 degree with $\cos\alpha$ are also plotted in Fig. 5.27. It shows that the flying height of both sliders decreases when the inclination angle increases both in drop with top cover facing up and in drop with top cover facing down. It is also observed that the maximum flying height of each slider at 30 degree shows a good agreement with the result from the corresponding curve. Because $A_{pe} = A_{pe}(0) \times \cos\alpha$, where A_{pe} is the amplitude of the acceleration perpendicular to the disk and $A_{pe}(0)$ is the amplitude at 0 degree. The agreement between the maximum flying height of slider at 30 degree with the corresponding curve implies that the maximum flying height of the sliders is proportional to the amplitude of the acceleration perpendicular to the disk at 0 degree and 30 degree. But the maximum flying height of the sliders at 60 degree is much smaller than the corresponding curve in Fig. 5.27. This disagreement can be explained by the fact the amplitude of the acceleration perpendicular to the disk at 60 degree is small and the lift-off of the slider is small or hardly happens. It can be concluded that the maximum flying height of the slider is proportional to the amplitude of the acceleration perpendicular to the disk when that amplitude is much greater and the lift-off of the slider is significantly high.

5.3.3 Summary

In order to improve the shock resistance of the disk and to avoid the head slap, the effect of inclination angle on the head slap for the small form factor drive is investigated here. A better understanding of the dynamic characterization of small form factor hard disk drive is achieved.

The flying height will decrease with the increasing of the inclination angle. The maximum of the flying height of the sliders is proportional to the amplitude of the acceleration perpendicular to the disk when the amplitude is high enough to overcome the preloading. The delay of lift-off between the two sliders also indicates the disk motion can cause the slider to lift off.

5.4 The Effect of The Clamping Condition on The Shock Response of The Disk

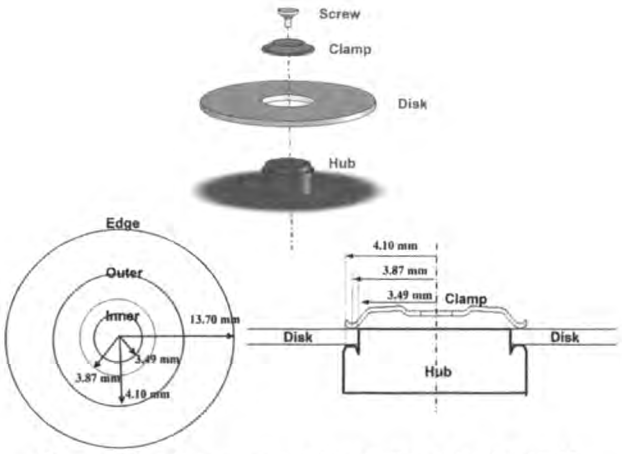

Fig. 5.28. One-screw-clamp for 1 inch HDD

In order to improve the shock resistance of the disk and to avoid the head slap, the actual boundary condition for the disk of S1 drive is further investigated here. A one-screw-clamp used by Seagate is shown in Fig. 5.28. The clamp and the hub are firmly bolted together by the screw at the center of the clamp and the hub. In this paper, the effect of clamping condition on the shock response of the disk for a small form factor HDD is investigated experimentally and numerically. A better understanding of the impact dynamic characterization of small form factor hard disk drive is achieved.

5.4.1 Experimental Setup & Procedures

In experiments, both measurement of the shock response of the disk and a modal testing of the disk are conducted. Fig. 5.29 shows a schematic diagram of the experimental setup for measuring the shock response of the disk. The setup is composed of a shaker, a B & K accelerometer, an accelerometer amplifier, an oscilloscope and Plolytec Laser Doppler Vibrometer (LDV) system. Plolytec LDV system comprises the scanning head, the junction box, the vibrometer controller and the computer. Fig. 5.30 shows a schematic diagram of the experimental setup for the modal testing of the disk. The setup is composed of the shaker, a shaker amplifier, a signal generator and Plolytec Laser Doppler Vibrometer (LDV) system. Fig. 5.31 shows a photograph of Plolytec Laser Doppler Vibrometer (LDV) system.

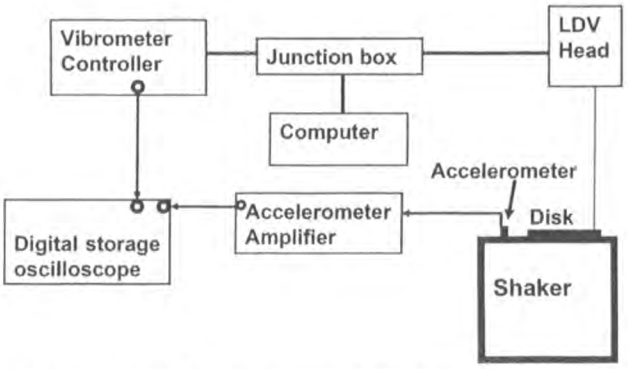

Fig. 5.29 Schematic diagram of the experimental setup for measurement of the shock response of the disk

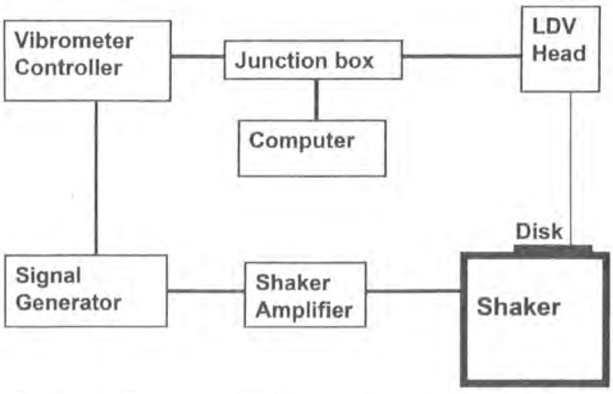

Fig. 5.30 Schematic diagram of the experimental setup for modal testing

Fig. 5.32 shows the mounting of the disk on the shaker. The disk is clamped between the clamp and the hub. The hub is glued on the shaker tightly. During the measurement of the shock response of the disk, the shaker surface covered by a felt is hit by a hammer to produce the shock pulse, which is measured by using the accelerometer attached onto the shaker. The magnitude and duration of the shock pulse are controlled by changing the hitting force and the material of the felt. The laser beam from LDV focuses at a point close to the edge of the disk to measure the displacement of that point. The acceleration history and the displacement data are recorded using the oscilloscope. The displacement of the shaker can be obtained by integrating the acceleration data twice. The hub is supposed to have the same displacement as the shaker since it is glued on the shaker tightly. Therefore, the relative displacement between the edge of the disk and the hub is obtained by subtracting the displacement of the hub from that of the disk.

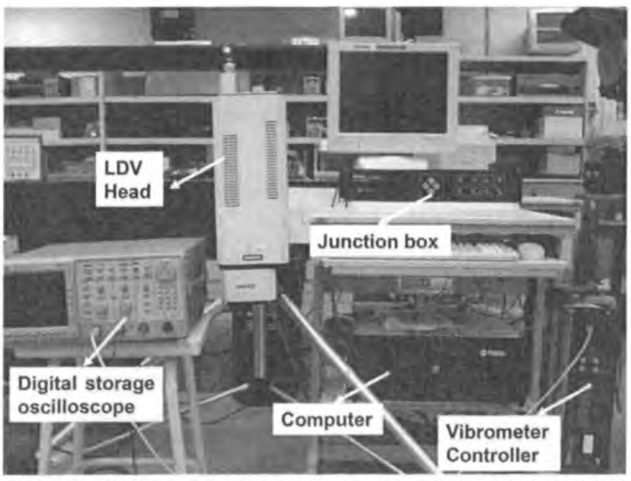

Fig. 5.31. Photo of Plolytec Laser Doppler Vibrometer (LDV) system

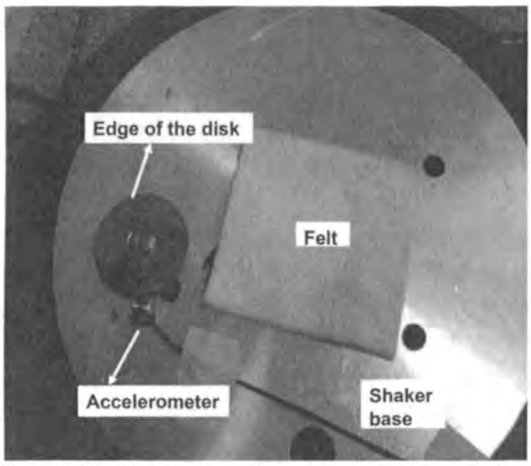

Fig. 5.32 Mounting of the disk on the shaker

Three clamping conditions are considered in the experiment as shown in Fig. 5.33. The first clamping condition is that the screw is fully tightened just as it is originally assembled in the factory. The second clamping condition is that the screw loosens a quarter turn by turning the screw with a screw driver. The third clamping condition is that the screw loosens half turn. It is known that the clamping force is approximately 40 N and the turn of the screw is one when the screw is fully tightened. Assuming that the number of turn of the screw is proportional to the clamping force, the clamping forces for the three clamping conditions are approximately 40 N, 30 N and 20 N, respectively.

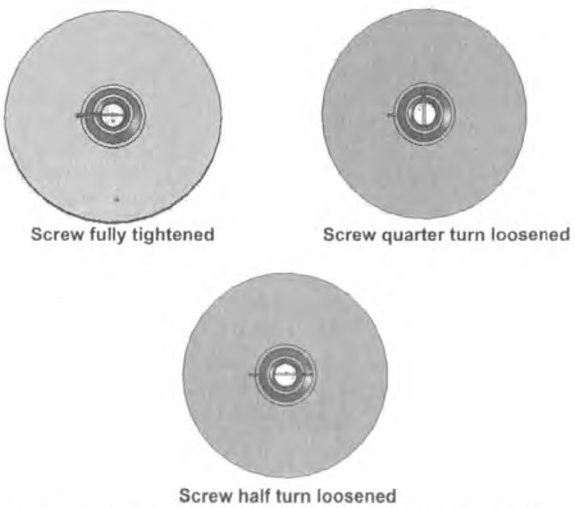

Fig. 5.33. Clamping conditions of the disk

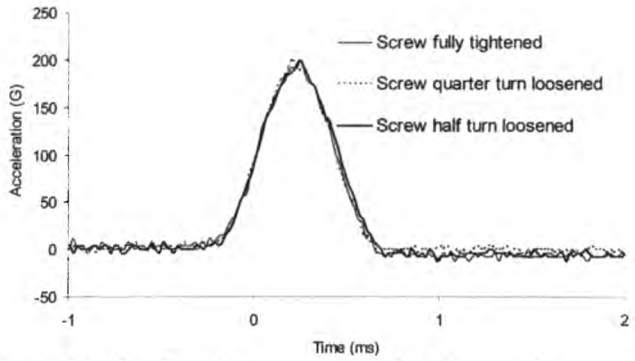

Fig. 5.34 Shock pulses measured by the accelerometer

Fig. 5.34 shows shock pulses measured by the accelerometer in the experiments. They are quite repeatable. These shock pulses can be approximated as half sine shock pulses with amplitude of 200 G and duration of 0.8 ms [16](Harris 1988).

5.4.2 Finite Element Modeling of The Disk

The boundary condition of the disk is also studied with simplified finite element (FE) models as shown in Fig. 5.35. The disk is parallel to the X-Y plane and is meshed with shell elements in ANSYS/LSDYNA. The disk is assumed to be either simply supported or fully clamped at the center rim. Here we define the simply supported boundary condition as only the translational degrees of freedom are constrained and the clamped boundary condition as all the degrees of freedom are constrained. When the Z-direction shock pulse is applied, the Z-direction translation will not be constrained. The following boundary conditions of the disk are applied to approximate the actual boundary conditions in Fig. 5.35.

B1: outer circle simply supported and where the shock pulse is applied on,

B2: both inner and outer circle clamped and where the shock pulse is applied on.

Modal analysis of the disk for boundary conditions B1 and B2 is conducted in ANSYS. The shock response of the disk is also computed when the shock pulse

shown in Fig. 5.34 is applied. The relative Z-displacement between the edge of the disk and the nodes where the acceleration pulse is applied is obtained.

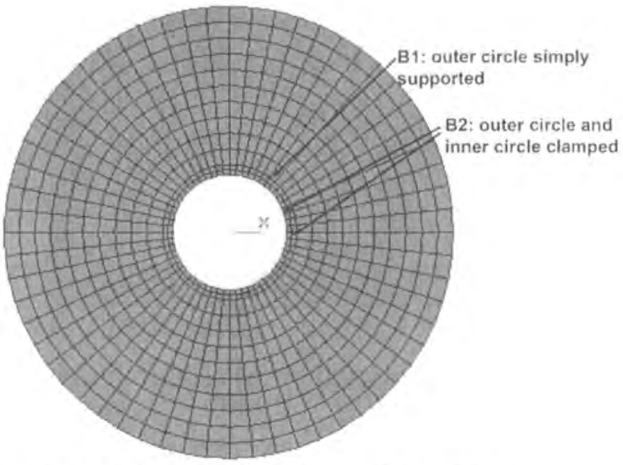

Fig. 5.35 Finite element model of the disk

5.4.3 Results and Discussion

Fig. 5.36 plots the relative displacement of the disk to the hub for the five different boundary conditions in either experiments or the FE analysis. It is seen that all the relative displacement reach the maximum magnitudes at the first peaks caused by the shock pulse and then oscillate afterwards. Compared with the simply supported boundary condition B1 in the FE analysis, vibration of the disk is much smaller for the clamped boundary condition B2. The results from experiments show that the amplitude of vibration of the disk becomes larger as the screw is loosened more. It is noted that the amplitudes of the vibration of the disk in experiments are greater than that of the disk with the clamped boundary condition B2 and are smaller than that of the disk with the simply supported boundary condition B1 in FE analysis.

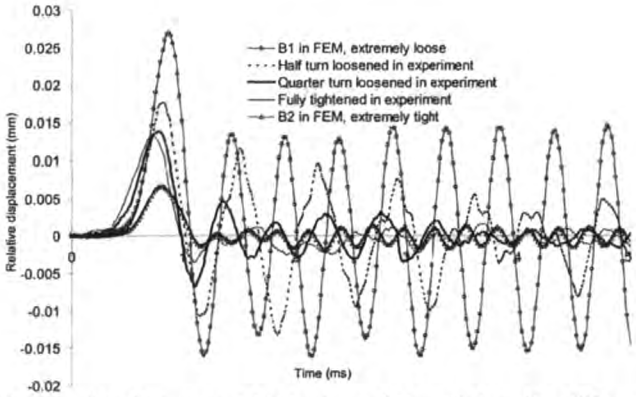

Fig. 5.36. Relative displacement histories of the disk with different boundary conditions

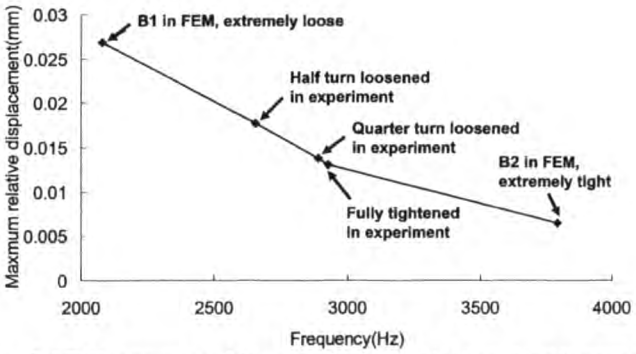

Fig. 5.37 Frequency Vs. maximum relative displacement

Table 5.1 lists all the natural frequencies of (0, 0) mode and maximum relative displacements of the disk for the five different boundary conditions both in experiments and in the FE analysis. Only the natural frequencies of (0, 0) mode from the modal testing and modal analysis are listed because the shock response of the disk is dominated by (0, 0) mode. It is found that frequencies obtained from experiments decrease as the screw is loosened. Moreover, frequencies obtained in experiments are higher than that of the simply supported boundary condition B1 and lower than that of the clamped boundary condition B2 in FE analysis. On the other hand, maximum relative displacements in experiments increase as the screw is loosened. Maximum relative displacements in experiments are higher than that of the clamped boundary condition B2 and lower than that of the simply supported boundary condition B1 in FE analysis. The frequency and maximum relative displacement of fully tightened

condition in experiments are close to that of fully clamped condition in FE analysis, while the frequency and maximum relative displacement of half turn loosened condition in experiment are close to that of simply supported condition in FE analysis. It can be concluded that the shock response of the disk decreases as the disk is more tightly clamped.

Table 5.1. Frequency of 0-0 mode and maximum relative displacement Vs. Boundary condition

Boundary conditions	Frequency of 0-0 mode (Hz)	Maximum relative displacement(mm)
B1 in FEM	2080	0.0269
Half turn loosened in experiment	2656	0.0177
Quarter turn loosened in experiment	2893	0.0138
Fully tightened in experiment	2928	0.0131
B2 in FEM	3790	0.0065

Fig. 5.37 shows the relation between the frequency and the maximum relative displacement of the disk. From Fig. 5.37, it can be found that the maximum relative displacement of the disk decreases as the frequency increases. This implies that the natural frequency of the disk increases as the disk is more tightly clamped, causing the disk to be more robust and more resistant to shock.

5.4.4 Summary

The effect of clamping condition on the shock response of the disk in the small form factor HDD is evaluated experimentally and numerically. It is found that as the disk is more tightly clamped the boundary condition of the disk is closer to the fully clamped condition and the shock response of disk decreases as well. It is also found that the maximum relative displacement of the disk decreases as the frequency increases.

5.5 Dynamic Strain Measurement of the Suspension

The strain gage is used universally by stress analysts in the experimental determination of stresses. Since strain always accompanies vibration, the strain gage or the principle by which it works is broadly applicable in the field of shock and vibration measurement. Here it serves to determine not only the magnitude of the strains produced by the shock or vibration, but also the entire time-history of the event, no matter how great the frequency of the phenomenon.

To the authors' knowledge, no measurement of the dynamic strain of the suspension of a small form factor HDD in drop tests has been achieved in published papers. In this paper the dynamic strain of the HAA of a one inch HDD in drop tests was measured using the strain gauge for the first time. A new way of measuring the shock response of the micro HDD was proposed.

5.5.1 Experimental Set-up

Fig. 5.38 shows a schematic diagram of the experimental setup used to measure the dynamic strain of the HAA in drop tests. The setup was composed of a Lansmount Drop Tester equipped with a Dual Mass Shock Amplifier (DMSA) capable of producing high amplitude and short width shock pulses, a strain-meter, an oscilloscope and a B & K accelerometer. The amplitude and width of the shock pulse were controlled by changing the falling height of the drop table and the material of the pads below the DMSA. The strain data was recorded using the oscilloscope connected with the dynamic strain-meter. Fig. 5.39 shows a photo of the experimental setup. The HAA was clamped onto the mounting table. A strain gauge was mounted on the HAA and the accelerometer was mounted on the fixture. The shock pulses were measured using the accelerometer.

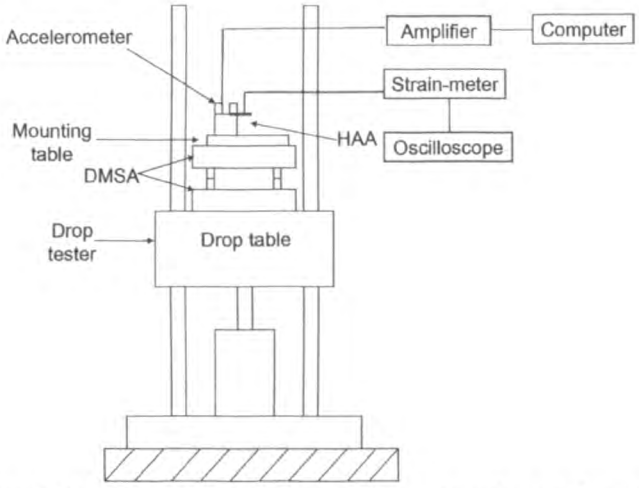

Fig. 5.38. Schematic diagram of the experimental setup.

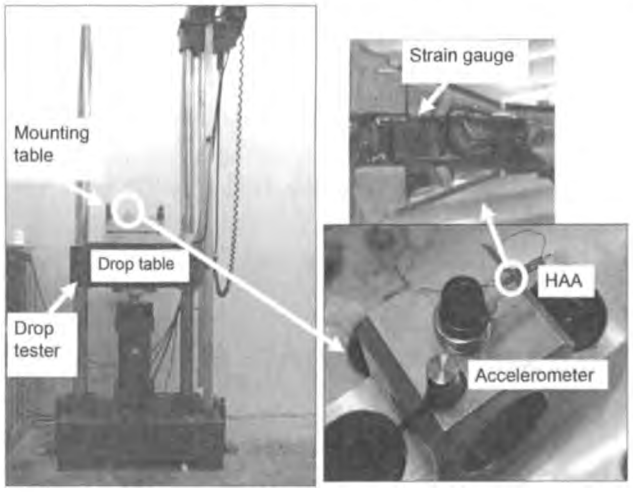

Fig. 5.39. Photographs of the experimental setup.

Fig. 5.39 shows the mounting of the strain gauge on the HAA. Due to the small size of the HAA of the one inch HDD, the area where the strain gauge was mounted onto is limited. A FBY-06-11-005LE strain gauge available in market was used. The dimension of the strain gauge is 0.8mm×0.6mm. The frequency response of a strain gauge is determined by the gauge length and the longitudinal elastic wave speed of the test specimen as shown in Fig. 5.40. The frequency response of this 0.8mm strain gauge should be higher than 530 kHz.

Gauge length (mm)	0.2	1	3	5	10	30	60
Steel [kHz]	660	530	360	270	170	–	–
Concrete [kHz]	–	–	–	–	120	50	20

Fig. 5.40. The frequency response of a strain gauge [94].

As shown in Fig. 5.41, the strain gauge was mounted onto the bottom surface of the suspension which is close to the hinge. The hinge is the thinnest part of the HAA and thus experiences the largest deformation under the shock pulse. The shock pulse was applied upward in drop tests.

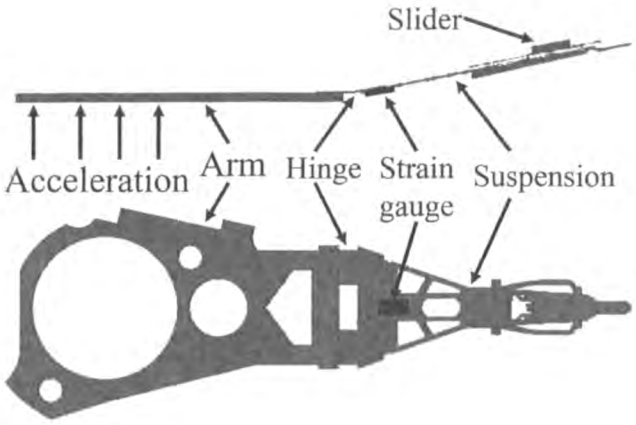

Fig. 5.41. The mounting of the strain gauge on the HAA.

5.5.2. Results and Discussion

Firstly, modal testing of the HAA was carried out to determine the influence of the mounting of the strain gauge on the dynamic properties of the HAA. Both the mode shape and natural frequency of the HAA without the strain gauge and the mode shape and natural frequency of the HAA with the strain gauge were measured by using a laser Doppler vibrometer (LDV) PSV-300 system. The first mode shape of the HAA without the strain gauge was shown in Fig. 5.42. It can be seen that the hinge bent while the arm unchanged. The HAA with the strain gauge had a similar first mode shape to that shown in Fig. 5.42, but the natural frequency of the first mode shape increased from 268 Hz to 413 Hz after the mounting of the strain gauge. Due to

the tiny size of the HAA, the mounting of the strain gauge had a big influence on the dynamic characteristics of the HAA.

Fig. 5.43 shows the three shock pulses of varying pulse widths and amplitudes measured by the accelerometer in the drop tests. These shock pulses can be approximated as half sine pulses with 250 G in amplitude and 1 ms in width, 500 G in amplitude and 1 ms in width, and 500 G in amplitude and 0.5 ms in width, respectively [16].

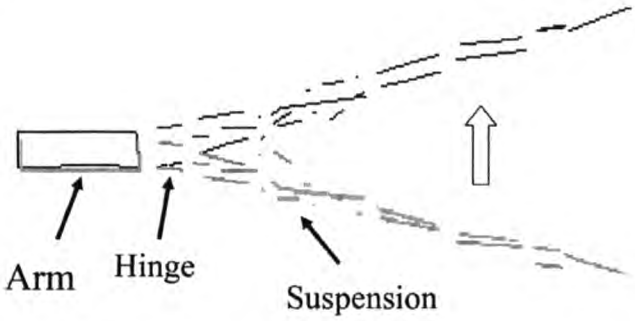

Fig. 5.42. The first bending mode shape of the HAA measured by LDV.

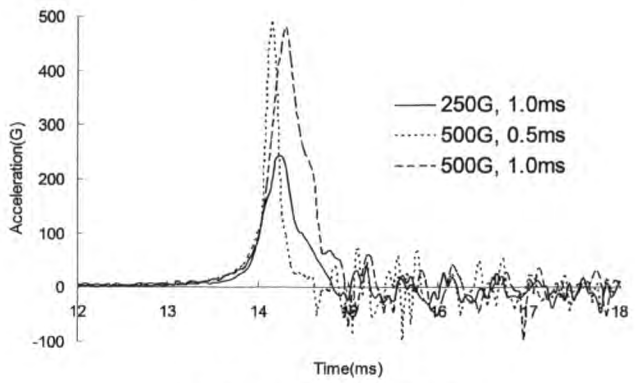

Fig. 5.43. Shock pulses.

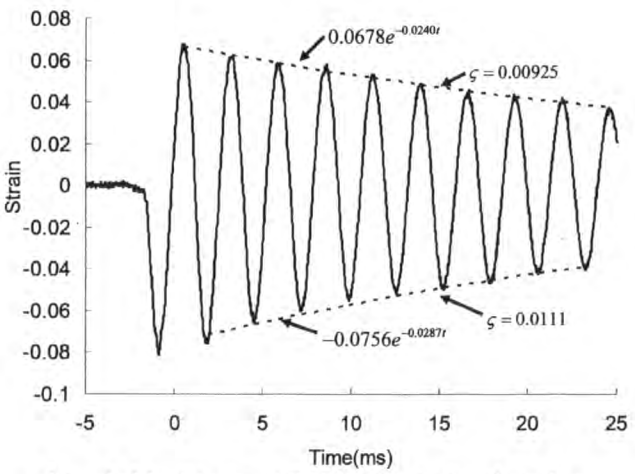

Fig. 5.44. Strain at 250G, 1 ms shock pulse

Fig. 5.44, 4.45 and 4.46 show the time histories of the dynamic strains obtained for the drop tests, where the half-sine shock pulses are 250 G in amplitude and 1 ms in width, 500 G in amplitude and 1 ms in width, and 500 G in amplitude and 0.5 ms in width, respectively. It is seen that all the dynamic strains reached the maximum magnitudes at the first negative peaks, where the strains are -0.0811, -0.181 and -0.105, respectively. Then the dynamic strains oscillated and decayed due to damping. The first peaks were caused by the shock loads and the HAA experienced the largest bending deformation. Comparison between Fig. 5.44 and Fig. 5.45 shows that the absolute maximum strain increases from 0.0811 to 0.181 with the amplitude of the shock pulse increasing from 250 G to 500 G. Comparison between Fig. 5.45 and Fig. 5.46 shows the absolute maximum strain increases from 0.105 to 0.181 with the pulse width of the shock pulse increasing from 0.5 ms to 1 ms.

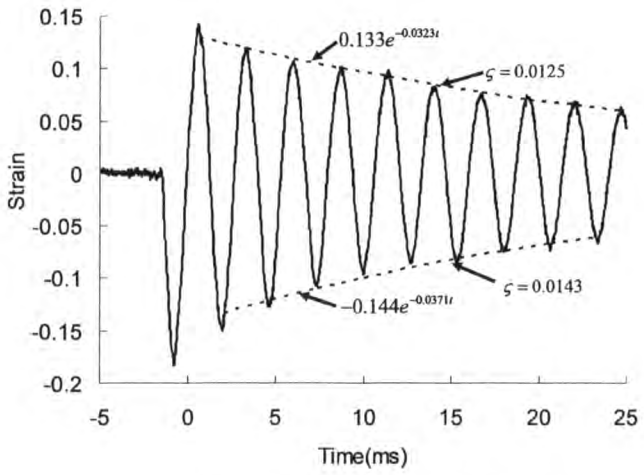

Fig. 5.45. Strain at 500G, 1 ms shock pulse.

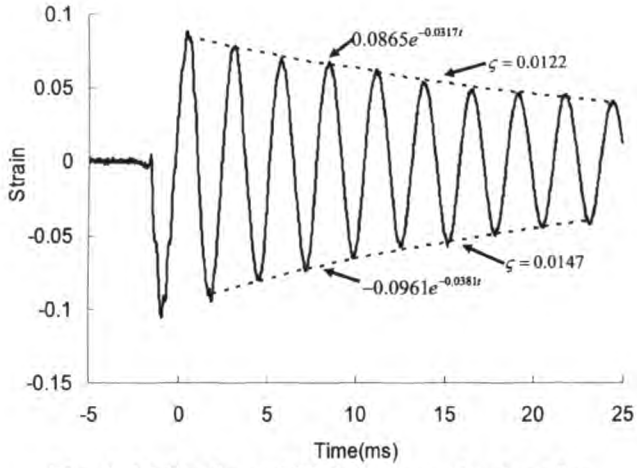

Fig. 5.46 Strain at 500G, 0.5 ms shock pulse

A power spectrum analysis was performed on the experimental dynamic strain results as shown in Fig. 5.47. It shows that the peaks of the power spectra curves are about 380 Hz, which is close to the natural frequency of the first mode shape of the HAA when the strain gauge was mounted on it. It can be seen that the first mode shape dominates the shock response of the HAA.

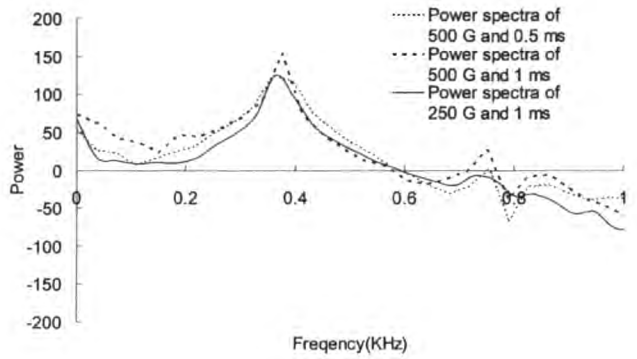

Fig. 5.47 Power spectra of the dynamic strains

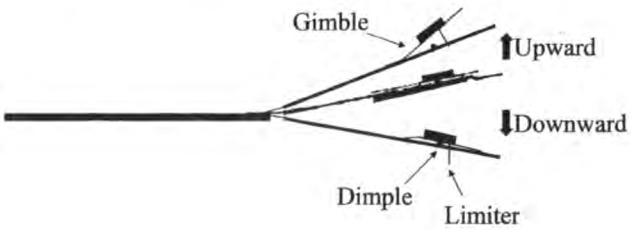

Fig. 5.48 Deformation of the HAA

The dynamic strain results are further discussed by simplifying the HAA as a single-degree-of-freedom system. For an underdamped single-degree-of-freedom system, the decaying function is $Ce^{-\zeta\omega_n t}$, where C, ζ and ω_n represent the amplitude, the viscous damping factor and the natural frequency, respectively. The functions of the exponential curves representing the decaying of the strain curves were obtained using the least squares method and are shown in Fig. 5.44, 5.45 and 5.46. Therefore, the values of $\zeta\omega_n$ are known. Because the first mode shape dominates the shock response of the HAA as discussed before, here ω_n can be approximated as $2\pi \times 413$ rad/s, which is the natural frequency of the first mode shape for the HAA with strain gauge mounted on. Therefore, the viscous damping factors ζ can be calculated and are shown in Fig. 5.44, 5.45 and 5.46. It is noted that both the amplitude C and the viscous damping factor ζ of the negative strain are greater than that of the positive strain in each strain curve. This non-linearity can be attributed to a few factors. First, there is the large deformation of the suspension due to both the initial pre-bending at the hinge and the subsequent deflection during and after the shock. Secondly, the friction and contact between the limiter and the suspension, the slider and the dimple can play a potentially important role here. The third possible factor is the larger negative and downward deformation of the suspension compared with the positive and upward deformation as shown in Fig. 5.48. During the upward and positive deformation as the suspension reaches its maximum, the slider with relatively flexible gimble tends to break away from the suspension and continue to move upward until it is finally held back by the limiter. On the other hand, when the suspension moves downward, the slider will be constrained to move together with the suspension. Because of the separate deformation of the suspension and the slider during the

upward movement, the suspension experiences lower deformation and strain than the downward movement, because part of the energy is stored in the larger deformation of the gimble and the slider. Similarly, the lower upward and positive deformation of the suspension is likely to lead to slower movement of the suspension and thus lower coefficient of viscosity.

Comparison between Fig. 5.44 and Fig. 5.45 shows the effect of shock amplitude on the damping of the oscillation of the HAA after the initial shock. Fig. 5.44 and Fig. 5.45 have the same shock width but different shock amplitude. 500 G Shock leads to damping factors of 0.0143 and 0.0125 which are 29% and 35% higher than the damping factors of 0.0111 and 0.00925 for the shock of 250 G, respectively. This is because the HAA vibrates with greater velocity as the amplitude of the shock pulse increases and the damping of the materials and structures are known to increase with velocity. Comparison between Fig. 5.45 and Fig. 5.46 shows the effect of shock width on the damping of the oscillation of the HAA after the initial shock. Fig. 5.45 and Fig. 5.46 have the same shock amplitude but different shock width. 0.5 ms Shock leads to damping factors of 0.0147 and 0.0122 which are close to the damping factors of 0.0143 and 0.0125 for the shock of 1 ms, respectively. The HAA subjected to 1 ms shock pulse vibrates with greater velocity than the HAA subjected to 0.5 ms shock pulse and thus higher damping factors. But 0.5 ms shock pulse is more likely to excite higher natural modes which tend to be damped out more quickly during the vibration. The effect of higher natural modes in Fig. 5.46 counteracts that of greater velocity in Fig. 5.45. Therefore, the damping factors in Fig. 5.45 are close to that in Fig. 5.46.

5.5.3 Summary

In this work the strain gauge was for the first time used to measure the dynamic strain of the HAA of one inch HDD in drop tests. It shows that the mounting of the

stain gauge causes the increase of the natural frequency of the HAA and the first mode shape dominates the shock response of the HAA. The maximum strain and the damping increases with the amplitude of the shock pulse. The maximum strain increases with the pulse width of the shock pulse. The effect of the pulse width on the damping is more complicated and can be further investigated in future studies. This work suggests the measurement of the dynamic strain of the HAA is conductible. A new way of measuring the shock response of small form factor HDD is proposed. The advantage of strain gauge is that it serves to determine not only the magnitude of the strains produced by the shock or vibration, but also the entire time-history of the event. The disadvantage of strain gauge is that it will change the original structure measured after the mounting.

5.6 Shock Pulse Shape Effect

Although the half-sine acceleration pulse is accepted as the industry standard, the recorded acceleration pulse in real test usually does not have the same shape as that of half-sine one. Some of the pulses shown in this chapter do not like half-sine, instead more like triangular ones.

Thus it's essential to study the influence of the shape change on the dynamic response of the drive. Shi, *et al* [3] investigated the pulse shape (half-sine, triangular and dual-quadratic pulses) effects in a shock analysis of an actuator arm.

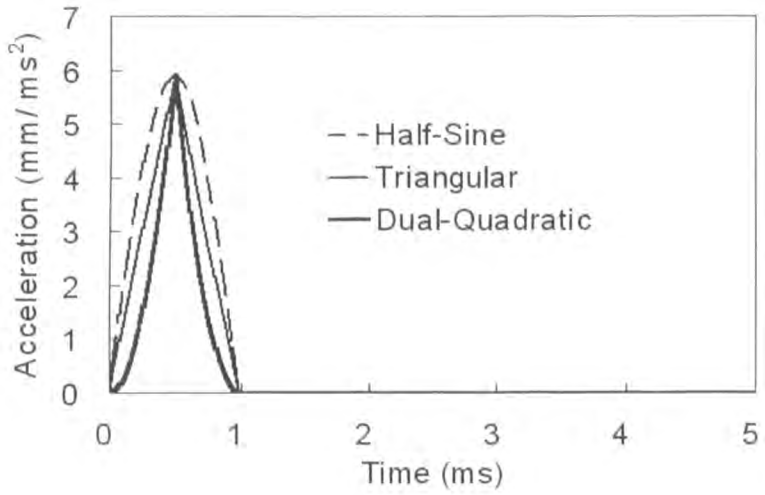

Fig. 5.49 Three acceleration shocks of 1-ms duration

There is cross-over interval of power spectrum curves located at a frequency value equal to the reciprocal of the pulse width as shown in Fig.5.49. When the natural frequency falls in the region to the left of the cross-over interval, the peak displacement of the half-sine acceleration waveform is the largest, followed by those of the triangular and dual-quadratic waveforms. However, when the natural frequency falls in the region to the right of this cross-over interval (but to the left of any possible second crossing point), the peak displacement of the dual-quadratic is the largest, followed by those of the triangular and half-sine waveforms. Near the cross-over point, the three pulse shapes give similar magnitudes of the peak displacement responses and the power spectra.

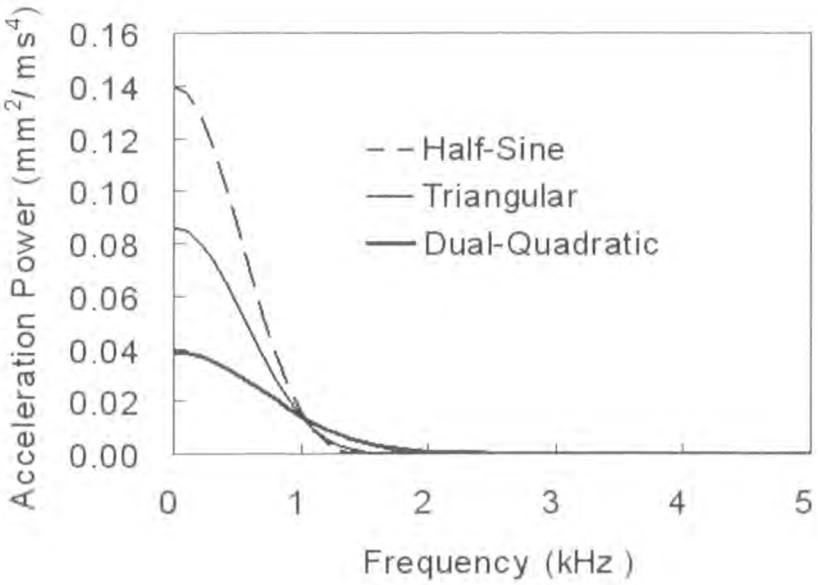

Fig. 5.50 Acceleration power spectra for 1-ms shock duration

In section 5.5, the natural frequency of the first mode shape of HAA after the mounting of the strain gauge is 413 Hz, which falls in the region to the left of the cross-over interval for 1 ms shock pulses as in Fig. 5.50, so the shock response of the HAA under triangular pulse is expected smaller than that under normal half sine pulse. In section 5.4, the (0,0) mode of the disk is higher than 2 kHz, which falls in the region to right of the cross-over interval, so the shock response of the disk under triangular pulse should be higher than that under half sine pulse.

CHAPTER 6

DYNAMIC FORCE MEASUREMENT OF A HEAD ARM ASSEMBLY

6.1 Introduction

Due to the small sizes of the head disk assembly (HDA) of the HDDs, the dynamic forces involved in these HDAs are of 0.01N in magnitude. As such, measuring these forces directly is difficult; displacement, frequency, and mode shapes are measured instead. Dynamic force measurements made using static measuring devices can be inaccurate. Other methods, including acoustic emission signals [82], force identifications [83], and direct measurements [84] have been applied in several studies to measure the contact forces in the head/disk interfaces, but the success of these methods has been limited. In the levitation mass method (LMM), the inertial force of a mass levitated using a pneumatic linear bearing is used as the reference force for the objects being tested, such as force transducers, materials [85]-[86].

In this chapter, dynamic forces of a head arm assembly (HAA) of a hard disk drive (HDD) against an impact load and in free oscillation are measured by means of non-linear finite element analysis (FEA) in ANSYS/LS-DYNA and experiments using a modified levitation mass method (LMM). Direct comparisons are made between computed and measured dynamic forces. The feasibility of applying FEA and LMM method to dynamic force measurement in drop tests of an HDD is demonstrated.

6.2 Impact Force Measurement of An HAA

In this section, dynamic response of a head arm assembly (HAA) against an impact load is obtained by means of a 3D non-linear finite element model in ANSYS/LS-DYNA and experiment using LMM method.

6.2.1 Experimental set-up

Fig. 6.1 shows a schematic diagram of the experimental setup for evaluating the dynamic force of an HAA of a Maxtor 2.5 inch HDD when it is impacted by a rigid mass. Fig. 6.2 shows the photograph of the test section.

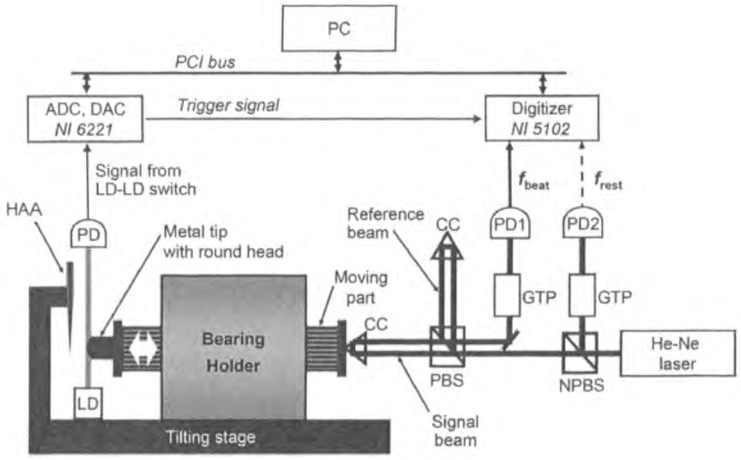

Fig. 6.1. Experimental setup for the dynamic force against impact load.

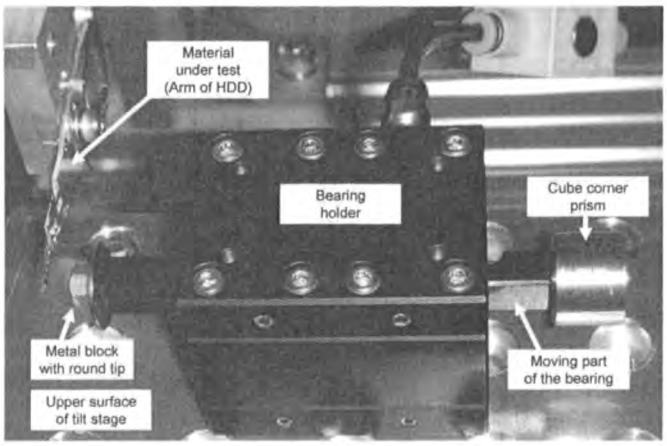

Fig. 6.2. Photograph of the test section for the dynamic force against impact load

The inertial force of the moving rigid mass (moving part) is used as the reference force applied to the HAA. An aerostatic linear bearing is used to obtain linear motion with negligible friction acting on the mass, i.e., the piston-shaped moving part of the bearing. The HAA is attached to the metallic base (tilting stage). An initial velocity is manually given to the mass. The impact force is generated by collision with the HAA. Due to the law of action and reaction, during the collision, one obtains

$$F_{Arm} = -F_{Movingpart} \tag{6.1}$$

A corner-cube prism (CC), that forms part of the interferometer, and a metal block with a round-shaped tip are attached to the moving part (made in aluminum with square pole shape); its total mass $M_{Movingpart}$ is approximately 21.18 g. The inertial force acting on the mass is measured highly accurately using an optical interferometer. The total force acting on the moving part $F_{Movingpart}$ is the product of its mass $M_{Movingpart}$ and its acceleration $a_{Movingpart}$,

$$F_{Movingpart} = M_{Movingpart} a_{Movingpart} \tag{6.2}$$

The acceleration is calculated from the time-varying velocity of the rigid mass. An optical interferometer is used to accurately measure the velocity. The light source used is a Zeeman-type two-wavelength He-Ne laser and light is incident on a polarization beam splitter (PBS). One wavelength is transmitted to the signal arm and then reflected from the corner-cube attached to the mass. The other wavelength is reflected from the beam splitter and into the reference arm. After propagation in the Michelson interferometer the signal and reference beams are transmitted through a polarizer (a Glann-Thompson prism at 45 degrees to the polarization of the beams, GTP), and hence interfere. The interfering beams are then incident on a detector PD1 and result in a beat signal, since the beams have slightly different wavelengths. The

rest frequency, f_{rest}, is measured with detector PD2. When the object is at rest, then $f_{beat} = f_{rest}$ is approximately 2.7 MHz. A digitizer (model: 5102; manufactured by National Instruments Corp., USA) records both signals from PD1 and PD2 with sampling number of 5M samples for each channel and with a sampling rate of 20MS/s. The measurement duration of the digitizer is 0.25 seconds. The mass velocity is obtained by measuring the induced Doppler shift in the signal beam of the laser interferometer and by using the following equations:

$$v = \lambda_{air} f_{Doppler} / 2 \qquad (6.3)$$

$$f_{Doppler} = -(f_{beat} - f_{rest}) \qquad (6.4)$$

where $f_{Doppler}$ is the Doppler shift, λ_{air} is the wavelength of the signal beam in the air, f_{beat} is the beat frequency, (i.e., the frequency difference between the signal beam and the reference beam), f_{rest} is the rest frequency defined above.

6.2.2 Finite Element Modelling

Fig. 6.3 shows the finite element model for the simulation of dynamic force against an impact load. In the FE model, Cartesian coordinates, X, Y, and Z are, respectively, parallel to the direction of the HAA length, width and thickness. The HAA consists of the arm, hinge, suspension, and connector, and is meshed with shell elements. The moving part is modeled as a rigid body and is constrained all the degrees of freedom except the translation in Z direction. Only the metal block with a round-shaped tip of the moving part is considered in modeling. It is meshed with solid elements and is given an enlarged mass density to make its mass to be equal to the total mass of the moving part $M_{Movingpart}$. By giving an initial velocity, the moving part is made to collide

with the tip of the HAA, which is fully constrained around the circle area of the arm. Automatic surface to surface contact is applied between the HAA (target part) and the rigid body (contact part) while friction is neglected during the collision. Z direction velocity of the rigid body is obtained from the time-history. Then the displacement and acceleration and the impact force of the moving part are calculated. Contact forces between the moving part and the HAA are also obtained through the simulation results.

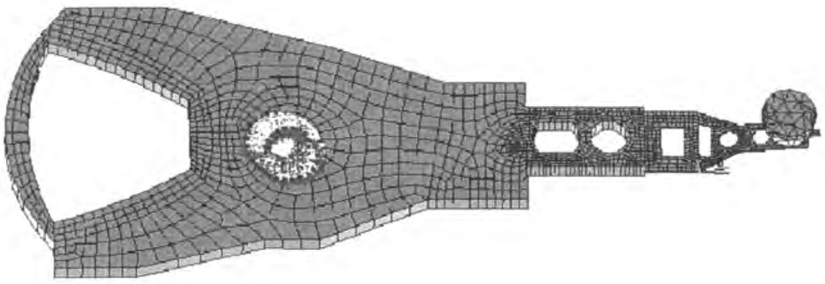

Fig. 6.3. Finite element model for the simulation of dynamic force against impact

6.2.3 Results and Discussion

Fig. 6.4 shows the comparisons between the numerical results and experimental results for the simulation and measurement of the impact force. Both the experimental results and the numerical results, such as displacement and acceleration are calculated from the velocity history of the moving part. A good agreement between the numerical results and experimental results is observed, especially the velocity and the displacement. In Fig. 6.4, the maximum value of the impact force from the experiment is 94 mN, where as from FEA it is 88 mN. The difference may contribute to the neglecting of the friction in FEA model.

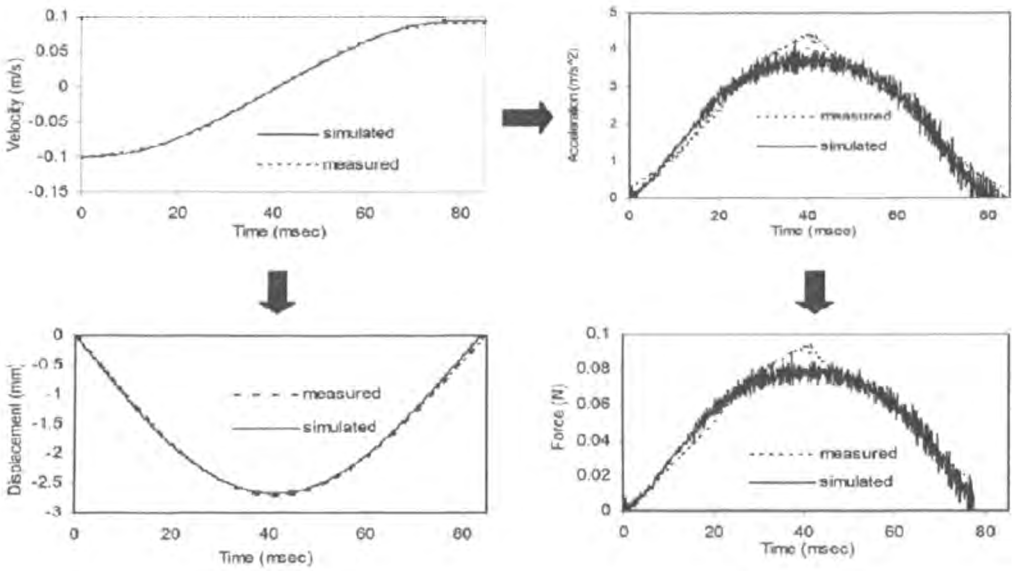

Fig. 6.4. Comparison between measured and simulated results for the impact force.

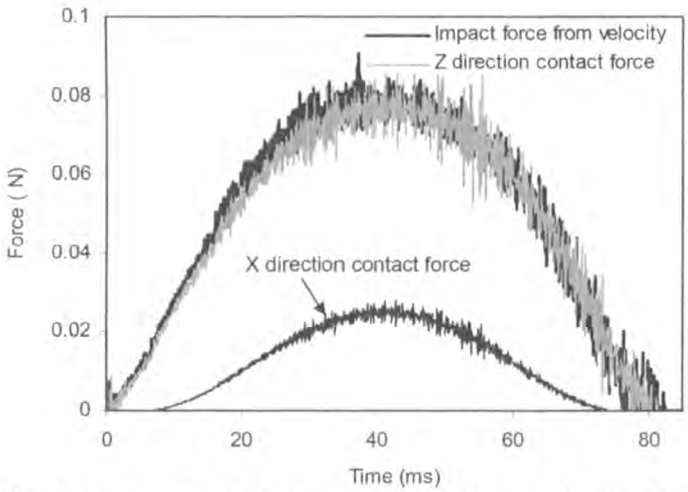

Fig. 6.5. X & Z direction contact force between the moving part and the HAA.

In Fig. 6.5, Z direction and X direction contact forces between the moving part and the HAA from the simulation results are plotted. The Y direction contact force is too small to be plotted. As shown in Fig. 6.5, the Z direction contact force is close to the simulated impact force, which is calculated from the velocity. The X direction contact force means that the impact between the moving part and the HAA is oblique due to the initial bending of the suspension and the its large deformation encountered in the impact process. The impact force either from simulation or from experiment in Fig.

6.4 is just the Z direction impact force because both of them are calculated according to the history of the Z direction velocity. In this test, the test rig is difficult to handle the oblique impact. The total impact force on the HAA is the combination effect of the X direction impact force and the Z direction impact force. The FEA is more suitable to calculate it after including the effect of friction.

6.3 Impact Induced Inertial Force Measurement of An HAA

In this section, inertial force of the Actuator Arm of a Hard Disk Drive (HDD) in free oscillation after an impact load is accurately measured by means of a finite element analysis and by carrying out experiments using a modified Levitation Mass Method (LMM).

6.3.1 Experimental Set-up

Fig. 6.6 shows a schematic diagram of the experimental setup for evaluating the inertial force of the HAA in free oscillation after an impact load. Fig. 6.7 shows the photograph of the test section. The arm is attached to the moving rigid mass (moving part) and an initial velocity is manually given to the mass. An impact is applied to the mass with the arm by colliding it to the base. Then the inertial force of the arm is evaluated during the free sliding motion of the mass. The mass of the arm M_{Arm} is 2.30 g and the mass of the moving part excluding the arm $M_{MovingPart}$ is 21.18 g.

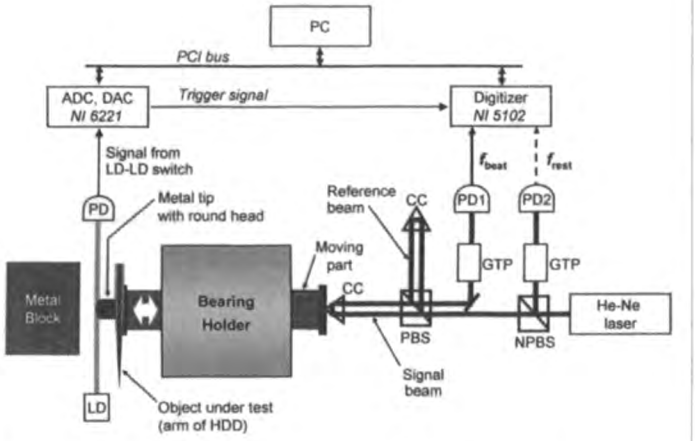

Fig. 6.6. Experimental setup for the free oscillation measurement.

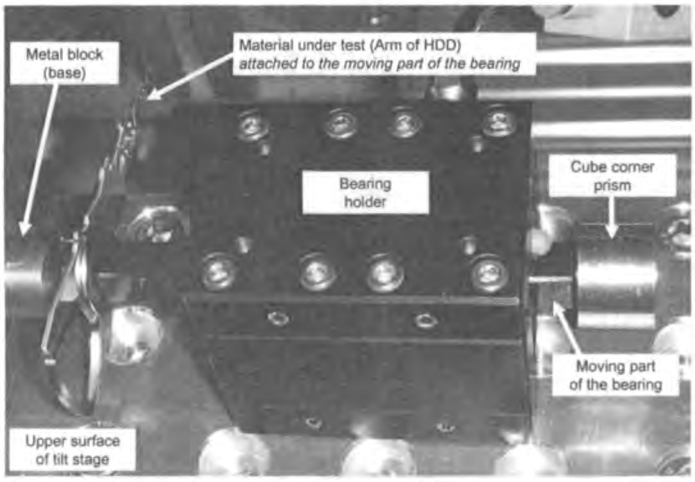

Fig. 6.7. Photograph of the test section for free oscillation measurement.

The inertial force acting on the mass of the moving part excluding the arm is measured highly accurately using the optical interferometer. The total force acting on the moving part $F_{MovingPart}$ is the product of the mass of the moving part excluding the arm $M_{MovingPart}$ and the acceleration of its center of gravity $a_{MovingPart}$, $F_{MovingPart} = M_{MovingPart} a_{MovingPart}$. The acceleration of the center of gravity of the moving part excluding the arm is considered to be the same as the acceleration of the optical center of CC attached to the moving part. The total force acting on the arm F_{Arm},

which is the product of the mass of the arm M_{Arm} and the acceleration of its center of gravity a_{Arm}, has the same absolute value and the opposite sign as the total force acting on the moving part $F_{MovingPart}$ due to the law of action and reaction. Then the inertial force of the arm is evaluated during the free sliding motion of the mass based on Eq. (6.1) – (6.4).

6.3.2 Finite Element Analysis (FEA)

A finite element model of the actuator arm of a Maxtor HDD is modeled in commercially available software, ANSYS 9.1 and simulation is carried out in LS-DYNA. The actuator arm consists of arm, hinge, suspension, connector, gimbal and slider, and is meshed with explicit thin structural shell elements, SHELL163. The moving part is modeled as a mass point and is coupled with the nodes on the arm. The FE model is shown in Fig. 6.8. Hinge, connector, suspension, and gimbal are made of stainless steel, arm is made of aluminum and the over mold is made of epoxy. Coil is inlaid into the over mold. Coil part is composed of layers of winding copper threads and its material property is anisotropic. It is assumed that the coil is made of isotropic material for simplicity. The impact load, which is modeled as a half sine force pulse, is applied to the mass point. Velocity and acceleration of the moving part are obtained from the time-history.

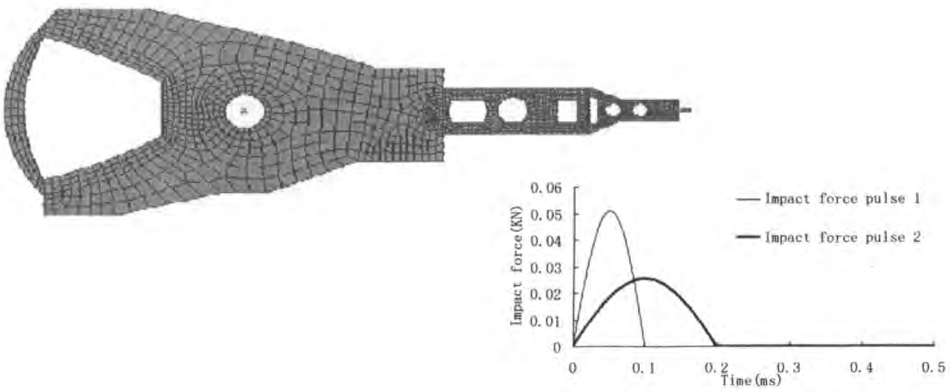

Fig. 6.8. Finite element model for the simulation of dynamic force in free oscillation

6.3.3 Results and Discussion

Fig. 6.9 shows the velocity of the moving part obtained in the experiment. The initial velocity V_0 is -0.12 mm/ms. The velocity after impact oscillates around V_{Stable}, which is 0.018mm/ms. Fig. 6.10 shows the velocity data with a magnified vertical axis and shorter duration. As for the region of 0 ms<t<2 ms, the oscillation of velocity shown in Fig. 6.9 and Fig. 6.10 is thought to mainly come from the viscoelastic vibration of the moving part itself. As for the region of 2 ms<t, the oscillation in velocity in Fig. Fig. 6.10 is thought to mainly come from the elastic vibration of the arm of HDD.

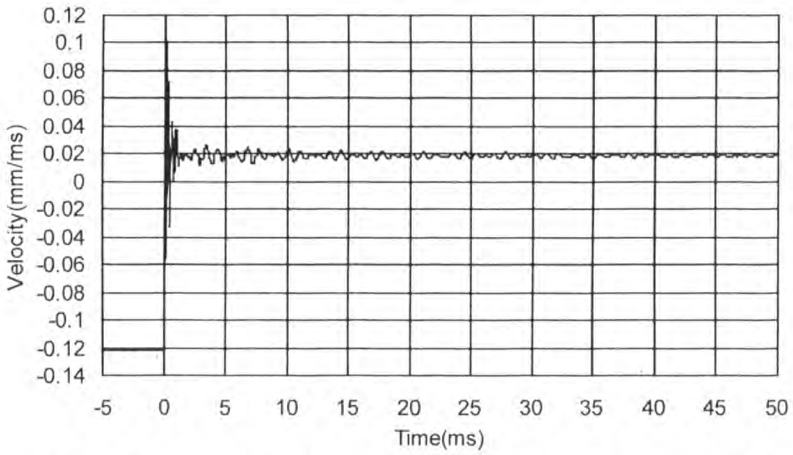

Fig. 6.9. Measured velocity against time in experiment (full scale)

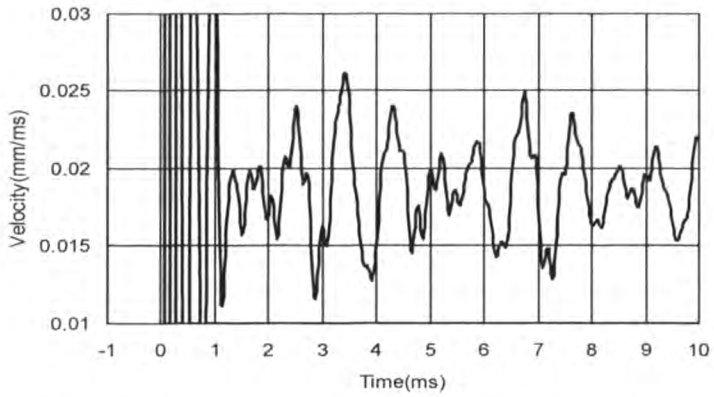

Fig. 6.10. Measured velocity against time in experiment (magnified scale)

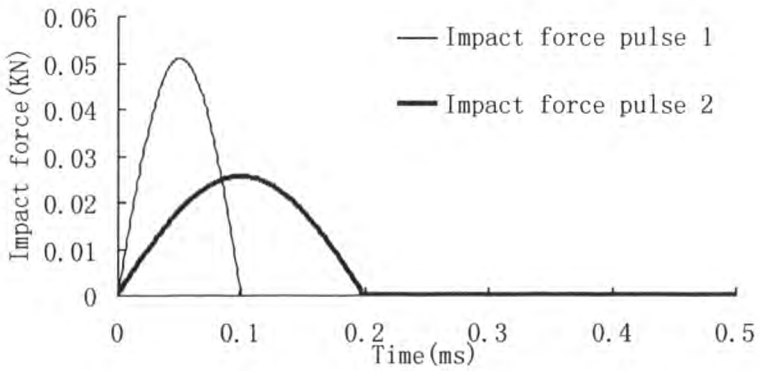

Fig. 6.11. The half sine force pulse applied in FEA

In the FEA, the friction acting on the moving part is neglected and the momentum conservation of the whole system, which consists of the arm and the moving part, is achieved. Comparing with the nearly perfectly elastic impact in the section 6.2, the impact here is so severe that the lost of kinetic energy is significant. In order to simplifying the simulation, the impact load is modeled as half sine force pulse with magnitude of F_{Peak} and width of τ. For the whole system, the following equation will be satisfied:

$$\int_0^{\tau} F_{Peak} \sin\frac{\pi t}{\tau} dt = (M_{MovingPart} + M_{Arm})(V_{Stable} - V_0) \qquad (6.5)$$

The impact time is estimated based on the inelastic impact theory [87]. So, 0.1 ms and 0.2 ms are chosen as the shock pulse width. When the pulse width is 0.1 ms and 0.2

ms, the pulse magnitude will be 0.051 KN and 0.0255 KN respectively. Fig. 6.11 shows the two force pulses applied in the FEA.

Fig. 6.12 shows the mass velocity during the whole process obtained in the simulation. It is more meaningful to compare the experimental data and numerical result in the time range of 2 ms<t< 8 ms when the whole system is in free oscillation state.

Fig. 6.13 and Fig. 6.14 show the comparison between the velocity and inertial force of FEA results and experimental data. In Fig. 6.13, the velocities of both pulses show similar low peak and high peak values, which are close to the low peak and high peak of experimental result. The periods between subsequent velocity peaks in both numerical results are close but are higher than that of experimental result. In Fig. 6.14, the inertial force of pulse 1 has more and higher low peak and high peak values than the experimental data while the inertial force of pulse 2 achieves a close low peak and high peak value to the experimental data.

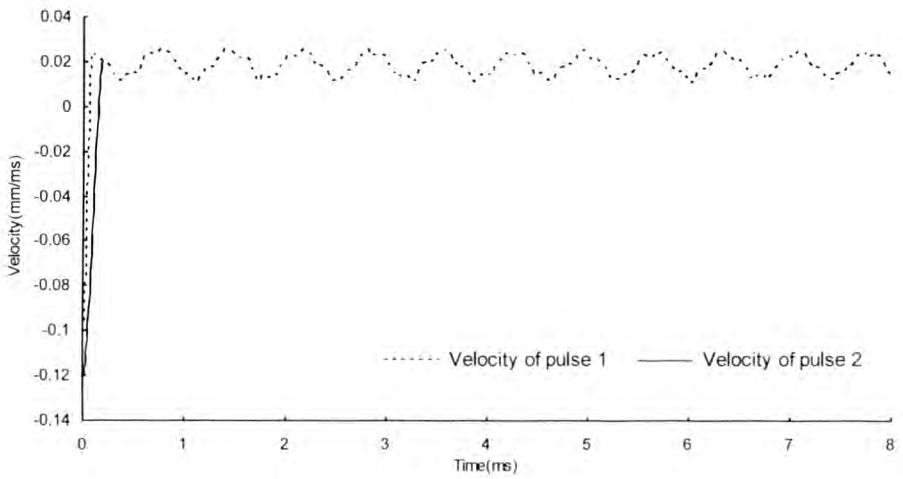

Fig. 6.12. Calculated velocities against time in the FEA

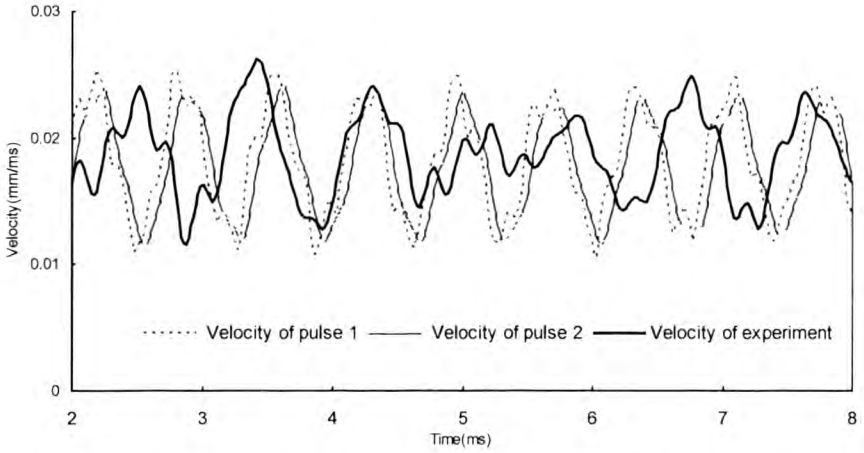

Fig. 6.13. The comparison between the velocity of FEA results and experimental data in free oscillation.

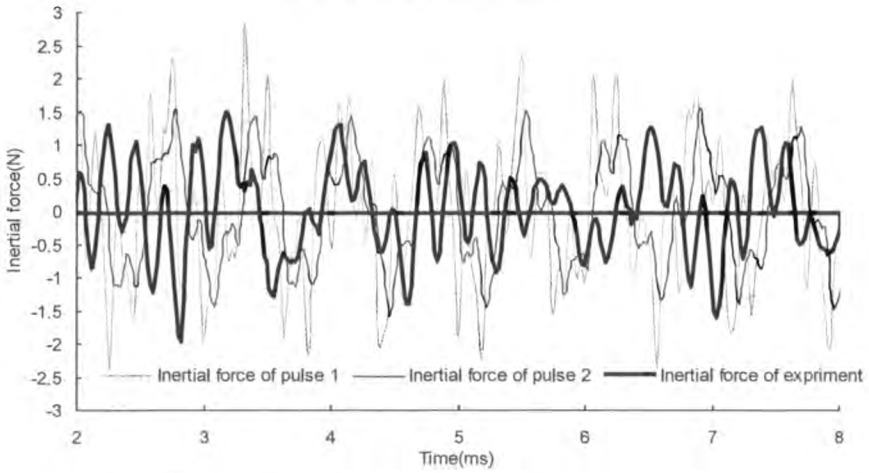

Fig. 6.14. The comparison between the inertial force of FEA results and experimental data in free oscillation.

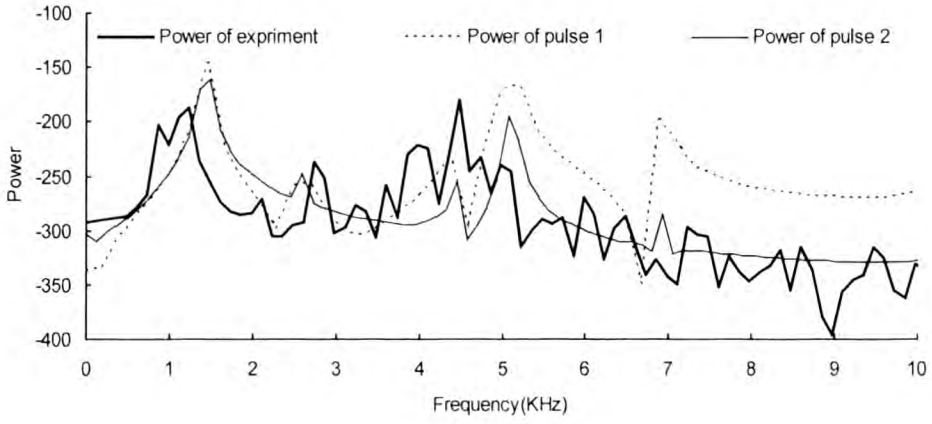

Fig. 6.15. Power spectra of the inertial force of FEA results and experimental data in free oscillation.

A power spectrum analysis is performed on the numerical and experimental inertial forces as shown in Fig. 6.15. In both curves for numerical results, each peak corresponds to one of the bending mode of the vibration of the actuator arm. The peaks in curve of experimental result also correspond to the bending mode of the vibration of the actuator arm. Due to damping, the natural frequencies in experiment are a bite lower than that of the FEA. The curve of pulse 2 is close to the curve of experiment. While the curve of pulse 1 has similar peaks with pulse 2 except the curve of pulse 1 gets a much higher peak than pulse 2 at 7000Hz. This can be explained by that the half sine force pulse with width 0.1 ms has a greater power at 7000Hz than the pulse with width of 0.2 ms in their power spectra. [6] The measurement of the inertial force of arm actuator in free oscillation is sensitive to the width of impact load.

6.4 Summary

Dynamic contact forces of the HAA are also measured and simulated by using LMM method and FEA. LMM method utilizes the first principles of Second Newtonian Law and the Doppler frequency shift and minimizes the uncertainties of using many sensors. A good agreement between the FEA results and experimental data is observed. But the limitation of the current experimental setup in oblique impact test and in inelastic impact test is investigated by the FEA method. This initial attempt demonstrates the feasibility of applying FEA and LMM method to minute dynamic forces measurement involved in HDDs. This attempt will be followed by improvement of current setup and future design of test rig to resemble the HDD drop test environment. Future modification is that attaching the disk on the metal block. The HAA head will impact the disk by giving the HAA head different initial flying

heights. The relationship between flying height and impact force, and even the disk surface's damage condition can be established.

The impact-induced free oscillation of an actuator arm of a HDD is accurately measured by means of a finite element analysis and by carrying out experiments using a modified Levitation Mass Method (LMM). A good agreement between the results of FEA and experimental data was achieved by modeled the impact load as half sine force pulse with certain width and magnitude. The inertial force of arm actuator in free oscillation after impact is sensitive to the width of impact load. Producing impact pulse with different amplitude and duration by changing the initial velocity and the base material, this experimental setup can easily investigate the shock response and shock characteristics of the actuator arm or disk (when change the actuator arm to disk) by studying the value and power spectra of the inertial force.

CHAPTER 7

CONCLUSIONS AND FUTURE WORK

7.1 Conclusions

The interest in the effects of shock on HDDs has come into currency due to the reduction of the flying height of the head/disk interface and the increasingly hostile environments encountered in the usage of many consumer electronics and portable devices. In this dissertation, drop and impact dynamic characteristics of hard disk drives were investigated by both experimental and numerical methods. The main conclusions are:

1. The real boundary condition of disk is studied with FE model. A SDOF system for disk component has been proposed. Based on the simulation results and the SDOF system, possible improvement on designs of disk assemble is discussed. It is found it help to decrease the shock response of the disk with higher clamping force and higher contact stiffness between disk and hub. The effect of clamping force on the shock response of the disk is further evaluated experimentally and numerically. The experimental results were agreeable with the numerical results.

2. The full hard disk FE models of linear drop test and rotary drop test are developed. The fundamental but important design rule of shock amplitude and duration effect is studied with FE models. Moreover, comparison between

linear drop tests and rotary drop tests shows that under the same shock pulse the slap behavior in linear drop tests is more significant than in rotary drop tests in view of the slider lift-up height.

3. The nonlinear FE model for simulation of the operational shock response of HDD is developed. The air bearing between the disk and the slider is modeled by nonlinear springs. The contact between the disk and the slider is also considered. The disk clamping condition and the shock pulse amplitude and width effects on the shock response of an operational HDD are investigated numerically.

4. Lansmount shock tester with dual mass shock amplifier (DMSA) is capable of producing very high amplitude, short duration half sine acceleration pulses. 1024 PCI FASTCAM-X high speed camera was successful to capture the lift-off the slider in both negative shock drop test and positive shock drop test. Initial fragility test on head slap has been done. Fragility assessment on head slap with arbitrary shock pulse is proposed. The differences between the shock table tests and real drop tests are discussed.

5. In experiments, the effect of inclination angle on the head slap for the small form factor drive is investigated. The flying height will decrease with the increasing of the inclination angle. The maximum of the flying height of the sliders is proportional to the amplitude of the acceleration perpendicular to the disk when the amplitude is high enough to overcome the preloading. The

delay of lift-off between the two sliders also indicates the disk motion can cause the slider to lift off.

6. The strain gauge was for the first time used to measure the dynamic strain of the HAA of one inch HDD in drop tests. It shows that the mounting of the stain gauge causes the increase of the natural frequency of the HAA and the first mode shape dominates the shock response of the HAA. The maximum strain and the damping increases with the amplitude of the shock pulse. The maximum strain increases with the pulse width of the shock pulse. The effect of the pulse width on the damping is more complicated and can be further investigated in future studies. This work suggests the measurement of the dynamic strain of the HAA is conductible. A new way of measuring the shock response of small form factor HDD is proposed.

7. Dynamic contact forces and impact-induced vibration of an HAA are measured and simulated by using LMM method and FEA. LMM method utilizes the first principles of Second Newtonian Law and the Doppler frequency shift and minimizes the uncertainties of using many sensors. A good agreement between the FEA results and experimental data is observed. But the limitation of the current experimental setup in oblique impact test and in inelastic impact test is verified by the FEA. This initial attempt demonstrates the feasibility of applying FEA and LMM method to minute dynamic forces measurement involved in HDDs.

7.2 Future Work

Based on the research work finished, the following aspects are recommended for further investigation.

Experiments:

1. To design shock table tests to mimic the real-life drop condition of hard disk drive.

2. To apply current LMM test to measure the minute dynamic forces when the slider hits the disk. Then to establish the relationship between flying height and impact force, and further the disk surface's damage condition.

Numerical simulations:

3. Spindle is an important part for the shock response of the HDD. The model of spindle will be added to the current model to make a full finite element model. So the influences from every part, the HAA, the disk, the base plate and the spindle, can be simulated in the drop test.

4. More complicated air bearing slider model to consider non-linear effect of pitch angle and roll angle of air bearing. To take into account intermolecular forces and electrostatic forces.

REFERENCE:

[1] C. J. Wilson and D. B. Bogy, "Experimental modal analysis of a suspension assembly loaded on a rotating disk," *Journal of Vibration and Acoustics, Transactions of the ASME*, vol. 116, pp. 85-92, 1994.

[2] E. M. Jayson, J. Murphy, P. W. Smith, and F. E. Talke, "Effects of air bearing stiffness on a hard disk drive subject to shock and vibration," *Journal of Tribology-Transactions of the ASME*, vol. 125, pp. 343-349, 2003.

[3] B. J. Shi, S. Wang, D. W. Shu, J. Luo, H. Meng, Q. Y. Ng, and R. Zambri, "Excitation pulse shape effects in drop test simulation of the actuator arm of a hard disk drive," *Microsystem Technologies*, vol. 12, pp. 299-305, 2006.

[4] D. W. Shu, B. J. Shi, H. Meng, F. F. Yap, D. Z. Jiang, Q. Y. Ng, R. Zambri, and J. H. T. Lau, "The pulse width effect of single half-sine acceleration pulse on the peak response of an actuator arm of hard disk drive," *Materials Science & Engineering A (Structural Materials: Properties, Microstructure and Processing)*, vol. 423, pp. 199-203, 2006.

[5] B. J. Shi, S. Wang, D. W. Shu, J. Luo, H. Meng, Q. Y. Ng, and R. Zambri, "Power spectrum analysis of the excitation pulse effects in drop test simulation of hard disk drives," presented at *Asia-Pacific Magnetic Recording Conference 2004. Digest of APMRC 2004*, 16-19, Seoul, Aug. 2004.

[6] Q. H. Zeng and D. B. Bogy, "Numerical simulation of shock response of disk-suspension-slider air bearing systems in hard disk drives," *Microsystem Technologies*, vol. 8, pp. 289-96, 2002.

[7] A. M. Allen and D. B. Bogy, "Effects of shock on the head-disk interface," *IEEE Transactions on Magnetics*, vol. 32, pp. 3717-19, 1996.

[8] S. Kumar, V. D. Khanna, and M. Sri-Jayantha, "A study of the head disk interface shock failure mechanism," *IEEE Transactions on Magnetics*, vol. 30, pp. 4155-7, 1994.

[9] A. Sagar, "Mobile Environment Demands Tougher Small Form Factor Drives," *Computer Technology Review*, pp.35-39, spring, 1993.

[10] S. Marek, Carlson, P. and Resh, R., "Why Head Suspension Need Shock Treatment," *Data Storage*, vol. 2(4), pp. 51-56, 1995.

[11] C.-W. Jen, F. E. Talke, T. Ohwe, and A. Gordon, "On suspension dynamics for pico-sliders," *IEEE Transactions on Magnetics*, vol. 33, pp. 3172-3174, 1997.

[12] S. J. Lee, S. K. Hong, and J. M. Lee, "Study of shock-resistance design of suspension subjected to impulsive excitation," *IEEE Transactions on Magnetics*, vol. 37, pp. 826-830, 2001.

[13] H. Takahashi, H. Shindo, S. Saegusa, S. Nakamura, and Y. Matsuda, "Adopting Taguchi method for designing high shock resistant head suspension assembly for mobile hard disk drives," presented at *2002 IEEE International Magnetics Conference-2002 IEEE INTERMAG*, Apr 28-May 2 2002, Amsterdam, Netherlands.

[14] H. R. Radwan, D. T. Phan, and K. Cao, "Effect of disk drive actuator unbalance on track following response to external vibration and shock," *IEEE Transactions on Magnetics*, vol. 32, pp. 1749-55, 1996.

[15] T. Kouhei, T. Yamada, Y. Kuroba, and K. Aruga, "A study of head-disk interface shock resistance," *IEEE Transactions on Magnetics*, vol. 31, pp. 3006-8, 1995.

[16] C. M. Harris, *Shock and Vibration Handbook*, 1988.

[17] T. Krauthammer, "Blast mitigation technologies: Developments and numerical considerations for behavior assessment and design," presented at *Proceedings of the 1998 5th International Conference on Structures Under Shock and Impact V*, Jun 1998, Thessaloniki, Greece, 1998.

[18] Q. M. Li and H. Meng, "Pulse loading shape effects on pressure-impulse diagram of an elastic-plastic, single-degree-of-freedom structural model," *International Journal of Mechanical Sciences*, vol. 44, pp. 1985-1998, 2002.

[19] N. Ishimaru, "Experimental studies of a head/disk interface subjected to impulsive excitation during nonoperation," *Journal of Tribology-Transactions of the ASME*, vol. 118, pp. 807-12, 1996.

[20] J.-S. Sohn, S.-H. Choa, M.-P. Hong, H.-S. Lee, and D.-H. Jang, "Experimental analysis of HDD actuator for the improvement of shock reliability," presented at *2000 Asia-Pacific Magnetic Recording Conference. Digest of APMRC2000*, 6-8 Nov. 2000, Tokyo, Japan.

[21] M. Tokuyama, Y. Katou, J. Shimizu, S. Hirose, Y. Kojima, and H. Nishida, "Development of shock proof suspension," *IEEE Transactions on Magnetics*, vol. 35, pp. 2484-2486, 1999.

[22] K.-K. Chew, "4-D shock-sensing for hard-disk drives," presented at *Proceedings of the 1999 IEEE International Magnetics Conference 'Digest of Intermag 99'*, May 18-May 21 1999, Kyongju, South Korea.

[23] H.-S. Lee, D.-H. Chang, J.-S. Sohn, M.-P. Hong, and S.-H. Choa, "Dynamic absorber for actuator arm in a disk drive," presented at *2000 Asia-Pacific Magnetic Recording Conference. Digest of APMRC2000*, 6-8 Nov. 2000, Tokyo, Japan.

[24] S. H. Lee, Lee, K.H. and Kim, K.J., "A Study on Modification of Dynamic Property of Base Structure in Hard Disk Drive for Shock Resistance Improvement," *Proceedings of ESDA2002/APM-029, 6th Biennial Conference on Engineering System Design and Analysis*, Istanbul, Turkey, July 8-11, 2002.

[25] Sharma, S.; Virmani, M.; Geers, T.L., "Direct Comparison of Computational and Experimental Head-Slap Data for a Nonoperating Hard Disk Drive," *IEEE Transactions on Magnetics*, vol.43, no.3, pp.1093,1100, March 2007

[26] J. C. Harrison and M. D. Mundt, "Flying height response to mechanical shock during operation of a magnetic hard disk drive," *Journal of Tribology-Transactions of the ASME*, vol. 122, pp. 260-263, 2000.

[27] G. Tunstall, W. Clegg, D. F. L. Jenkins, and C. Chilumbu, "Head-media interface instability under hostile operating conditions," *IEEE Transactions on Instrumentation and Measurement*, vol. 51, pp. 293-298, 2002.

[28] H. Kuwajima, H. Kita, H. Hashi, M. Miyamoto, Y. Ueno, T. Inagaki, and K. Matsuoka, "Development of balanced-type high shock suspension for 0.85-in hard disk drive," *IEEE Transactions on Magnetics*, vol. 42, pp. 255-260, 2006.

[29] Dapeng Zhao; Xiongfei Wei; Bin Liu; Shengxiang Chen; Yu Wang; Ailian Peng, "Thermal Asperity Sensor Application to Hard Disk Drive Operational Shock," *IEEE Transactions on Magnetics*, vol.49, no.2, pp.699,702, Feb. 2013

[30] G. M. Frees and D. K. Miu, "Experimental and numerical analysis of read/write head suspension dynamics for high-performance floppy drive systems," *Journal of Vibration, Acoustics, Stress, and Reliability in Design*, vol. 112, pp. 26-32, 1990.

[31] A. H. Jeans, "Analysis of the dynamics of a type 4 suspension," *Journal of Vibration, Acoustics, Stress, and Reliability in Design*, vol. 114, pp. 74-78, 1992.

[32] O. J. Ruiz and D. B. Bogy, "A numerical simulation of the head-disk assembly in magnetic hard disk files. I. Component models," *Journal of Tribology-Transactions of the ASME*, vol. 112, pp. 593-602, 1990.

[33] O. J. Ruiz and D. B. Bogy, "A numerical simulation of the head-disk assembly in magnetic hard disk files. II. Solution of the coupled system," *Journal of Tribology-Transactions of the ASME*, vol. 112, pp. 603-13, 1990.

[34] C. J. Wilson and D. B. Bogy, "Modal analysis of a suspension assembly," *Journal of Engineering for Industry, Transactions of the ASME*, vol. 116, pp. 377-386, 1994.

[35] T. G. Jeong, J. I. Chun, C. C. Chung, Y. K. Byun, and K. C. Ro, "Measurement technique for dynamic characteristics of HDD head-suspension assembly in normal operating conditions," presented at *Proceedings of International Conference on Micromechatronics for Information for Information and Precision Equipment (MIPE'97)* (Vol.9), , Tokyo, Japan, 20-23 July 1997.

[36] K. Aruga, Y. Kuroba, S. Koganezawa, T. Yamada, Y. Nagasawa, and Y. Komura, "High-speed orthogonal power effect actuator for recording at over 10,000 TPI," *IEEE Transactions on Magnetics*, vol. 32, pp. 1756-1761, 1996.

[37] L. Jiang and R. N. Miles, "A passive damper for the vibration modes of the head actuator in hard disk drives," *Journal of Sound and Vibration*, vol. 220, pp. 683-694, 1999.

[38] H. R. Radwan, F.-Y. Huang, J. Serrano, and E. Oettinger, "Control-structure interaction in disk drives using modal superposition and finite element analysis," *Journal of Information Storage and Processing Systems*, vol. 1, pp. 87-94, 1999.

[39] S. Zeng, R.-M. Lin, and L.-M. Xu, "Novel method for minimizing track seeking residual vibrations of hard disk drives," *IEEE Transactions on Magnetics*, vol. 37, pp. 1146-1156, 2001.

[40] J. L. Aristegui and T. L. Geers, "Shock analysis of a disk-drive assembly," *Journal of Information Storage and Processing Systems*, vol. 2, pp. 25-31, 2000.

[41] J. R. Edwards, "Finite element analysis of the shock response and head slap behavior of a hard disk drive," *IEEE Transactions on Magnetics*, vol. 35, pp. 863-867, 1999.

[42] C.-C. Lin, "Finite element analysis of a computer hard disk drive under shock," *Journal of Mechanical Design, Transactions of the ASME*, vol. 124, pp. 121-125, 2002.

[43] E. M. Jayson, J. Murphy, P. W. Smith, and F. E. Talke, "Head slap simulation for linear and rotary shock impulses," *Tribology International*, vol. 36, pp. 311-316, 2003.

[44] F. Gao, F. F. Yap, Y. Yan, and H. Harmoko, "Shock analysis of non-operating hard disk drives based on a multibody dynamic formulation," *Microsystem Technologies*, vol. 12, pp. 247-257, 2006.

[45] M. Suk and D. Gillis, "Effect of slider burnish on disk damage during dynamic load/unload," presented at *World Tribology Congress*, Sept. 1997 *Journal of Tribology-Transactions of the ASME*, London, UK, 1998.

[46] T.-C. Fu and D. B. Bogy, "Analysis of stresses induced by dynamic load head-disk contacts," *Journal of Tribology-Transactions of the ASME*, vol. 122, pp. 233-237, 2000.

[47] H.-L. Leo and G. B. Sinclair, "So how hard does a head hit a disk?," *IEEE Transactions on Magnetics*, vol. 27, pp. 5154-5156, 1991.

[48] G. Sheng, B. Liu, and Y. L. Zhu, "Vibrations in contact magnetic recording system: basic features, analytical solution and novel numerical method," presented at *Proceedings of International Conference on Micromechatronics for Information for Information and Precision Equipment (MIPE'97)* (Vol.9), 20-23 July 1997, Tokyo, Japan, 1998.

[49] G. Sheng, W. Hua, Q. Chen, and B. Liu, "Experimental and analytical study of head-disk impact and dynamics of negative-pressure sliders in the unloading process," *Journal of Information Storage and Processing Systems*, vol. 2, pp. 281-91, 2000.

[50] E. M. Jayson, J. M. Murphy, P. W. Smith, and F. E. Talke, "Shock and head slap simulations of operational and nonoperational hard disk drives," *IEEE Transactions on Magnetics*, vol. 38, pp. 2150-2152, 2002.

[51] B. J. Shi, D. W. Shu, J. Luo, Q. Y. Ng, and J. H. T. Lau, "Experimental and numerical analyses of the head arm assembly of a micro-drive," *Key Engineering Materials*, vol. 326-328 II, pp. 1585-1588, 2006.

[52] Hongrui Ao; Haodong Wei; Hongyuan Jiang, "Effect of the external shock on the dynamic characteristics of dual sliders at operational state for small form factor hard disk drives," *Systems and Control in Aeronautics and Astronautics (ISSCAA), 2010 3rd International Symposium*, pp.1233,1236, 8-10 June 2010

[53] Rai, R.; Bogy, D.B., "Parametric Study of Operational Shock in Mobile Disk Drives With Disk–Ramp Contact," *IEEE Transactions on Magnetics*, vol.47, no.7, pp.1878,1881, July 2011

[54] Li, L.; Bogy, D., "Numerical Analysis of Head Disk Interface Response during Operational Shock with Disk-Ramp Contact," *IEEE Transactions on Magnetics*, vol.99, pp.1,1, 2013

[55] G. H. Jang and J. H. Han, "Finite element modal analysis of a spinning flexible disk-spindle system in a HDD considering the flexibility of complicated supporting structure," *Microsystem Technologies*, vol. 11, pp. 766-778, 2005.

[56] G. H. Jang, C. H. Seo, and H. S. Lee, "Finite element modal analysis of an HDD considering the flexibility of spinning disk-spindle, head-suspension-actuator and supporting structure," *Microsystem Technologies*, vol.13, pp. 837-847, May 2007.

[57] Mengjun Liu; Fook Fah Yap; Harmoko, H., "A Model for a Hard Disk Drive for Vibration and Shock Analysis," *IEEE Transactions on Magnetics*, vol.44, no.12, pp.4764,4768, Dec. 2008.

[58] B. Liu, S. K. Yu, M. S. Zhang, L. Gonzaga, H. Li, J. Liu, and Y. S. Ma, "Air-bearing design towards highly stable head-disk interface at ultralow flying height," *IEEE Transactions on Magnetics*, vol. 43, no. 2, pp. 715-720, Feb. 2007.

[59] Z. M. Yuan, B. Liu, T. J. Zhou, et al., "Perspectives of Magnetic Recording System at 10 Tb/in(2)," *IEEE Transactions on Magnetics*, vol. 45, pp. 5038-43, 2009.

[60] P. Bhargava, and D. B. Bogy, "Numerical simulation of operationalshock in small form factor hard disk drives", *Journal of Tribology-Transactions of the ASME*, vol. 129, no. 1, pp. 153-160, 2007.

[61] A. N. Murphy, B. Feliss, D. Gillis, and F. E. Talke, "Experimental and numerical investigation of shock response in 3.5 and 2.5 in. form factor hard disk drives", *Microsystem Technologies*, vol. 12, pp. 1109-1116, 2006.

[62] D. W. Shu, B. J. Shi, H. Meng, F. F. Yap, D. Z. Jiang, Q. Y. Ng, R. Zambri, J. H. T. Lau, and C. S. Cheng, "Shock analysis of a head actuator assembly subjected to half-sine acceleration pulses," *International Journal of Impact Engineering*, vol. 34, pp. 253–263, 2007.

[63] M. J. Liu, F. F. Yap, and H. Harmoko, "Dimple-flexure contact stiffness effect on operational hard disk drive shock tolerance," *Microsystem Technologies*, vol. 14, pp. 1157-1163, 2008.

[64] B. J. Shi, D. W. Shu, J. Luo, B. Gu, G. W. Ma, Q. Y. Ng and S. Gan, "Operational Shock Simulation of the Head–Disk Assembly of a Small-Form Factor Drive", *IEEE Transactions on Magnetics*, vol. 43, pp. 4042 -4047, 2007.

[65] J. Luo, D. W. Shu, B. J. Shi, Q. Y. Ng, R. Zambri, and J. H. Lau, "Study of the shock response of the HDD with ANSYS-LSDYNA," *Journal of Magnetism and Magnetic Materials*, vol. 303, pp. 57-61, 2006.

[66] A. H. Nayfeh, A. Jilani, and P. Manzione, "Transverse vibrations of a centrally clamped rotating circular disk," *Nonlinear Dynamics*, vol. 26, pp. 163-178, 2001.

[67] A. A. Renshaw, "Increasing the natural frequencies of circular disks using internal channels," *Journal of Sound and Vibration*, vol. 229, pp. 355-375, 2000.

[68] A. A. Renshaw, "Natural frequencies of circular plates including the effects of transverse shear and rotary inertia," *Journal of Sound and Vibration*, vol. 193, pp. 1122-1124, 1996.

[69] J. Irons and W. Kennedy, "Non-linear vibration of centrally clamped thin discs," *International Journal of Non-Linear Mechanics*, vol. 24, pp. 345-352, 1989.

[70] C. I. D'Angelo and C. D. J. Mote, "Natural frequencies of a thin disk, clamped by thick collars with friction at the contacting surfaces, spinning at high rotation speed," *Journal of Sound and Vibration,* vol. 168, pp. 1-14, 1993.

[71] A. Jana and A. Raman, "Nonlinear dynamics of a flexible spinning disc coupled to a precompressed spring," *Nonlinear Dynamics*, vol. 40, pp. 1-20, 2005.

[72] A. A. Renshaw and C. D. J. Mote, "Perturbation solution for the flexible rotating disk: non-linear equilibrium and stability under transverse loading," *Journal of Sound and Vibration*, vol. 183, pp. 309-326, 1995.

[73] D. S. Dugdale, "NON-LINEAR VIBRATION OF A CENTRALLY CLAMPED ROTATING DISC.," *International Journal of Engineering Science*, vol. 17, pp. 745-756, 1979.

[74] J. W. Heo and J. Chung, "Vibration analysis of a flexible rotating disk with angular misalignment," *Journal of Sound and Vibration*, vol. 274, pp. 821-841, 2004.

[75] Hendri Harmoko, "Towards High Shock Resistance Hard Disk Drive-A Comprehensive Study by Research, Simulations and Experiments", *Confirmation Report*.

[76] *LS-DYNA users manual*. Livermore Software Technology Corporation, March 1998.

[77] Juvinal, R. C., 1983, *Fundamentals of Machine Component Design*, John Wiley and Sons, New York.

[78] A. A. Renshaw, "Maximizing the natural frequencies and transverse stiffness of centrally clamped, circular disks by thickening the clamped part of the disk," *Journal of Applied Mechanics, Transactions ASME*, vol. 66, pp. 1017-1021, 1999.

[79] G. Sheng, B, Liu and W. Hua, "A nonlinear dynamics theory for modeling slider air bearing in hard disk drives," *Journal of Applied Physics*, vol. 87, pp. 6173-6175, 2000.

[80] B. H. Thornton and D. B. Bogy, "Nonlinear aspects of air-bearing modeling and dynamic spacing modulation in sub-5-nm air bearings for hard disk drives," *IEEE Transactions on Magnetics*, vol. 39, pp. 722-728, 2003.

[81] G. Sheng, R. Dukkipati and J. Pang, "Nonlinear dynamics of sub-10 nm flying height air bearing slider in modern hard disk recording system," *Mechanism and Machine Theory*, vol. 41, pp. 1230-1242, 2006.

[82] W. Hua, Y. J. Man, and B. Liu, "Contact force studies of a burnishing slider," *Tribology International*, vol. 41, pp. 60-66, 2008.

[83] M. Matsumoto, A. Iida, and T. Hamaguchi, "Measurement of slider/disk collision forces using acoustic emission source wave analysis," *Tribology Transaction*, vol. 36, no. 4, pp. 736-740, 1993.

[84] G. J. Burger, *A Slider Motion Monitoring System: Measuring Contact and Friction Forces in Rigid Disk Storage Devices*, Ph.D dissertation, Dept. of Applied Physics, Univ. of Twente, pp. 41-82, 1995.

[85] Y. Fujii, "Proposal for a step response evaluation method for force transducers," *Measurement Science and Technology*, vol. 14, no. 10, pp. 1741-1746, 2003.

[86] Y. Fujii and T. Yamaguchi, "Proposal for material viscoelasticity evaluation method under impact load," *Journal of Materials Science*, vol. 40, no. 18, pp. 4785-4790, 2005.

[87] K. L. Johnson, *Contact Mechanics*, Cambridge, U.K: Cambridge University Press.

[88] Thornton, B.H.; Bogy, D.B., "A parametric study of head-disk interface instability due to intermolecular forces," *IEEE Transactions on Magnetics*, vol.40, no.1, pp.337,344, Jan. 2004.

[89] Ambekar R, Gupta V, Bogy DB., "Experimental and Numerical Investigation of Dynamic Instability in the Head Disk Interface at Proximity," *Journal of Tribology-Transactions of the ASME*, vol.127, no.3, pp.530-536, 2005.

[90] Gupta, V.; Bogy, D.B., "Dynamics of sub-5-nm air-bearing sliders in the presence of electrostatic and intermolecular forces at the head-disk interface," *IEEE Transactions on Magnetics*, vol.41, no.2, pp.610,615, Feb. 2005

[91] Newton, R. E., *Fragility Assessment Theory and Test Procedure*, Monterey Research Laboratory, Monterey, CA, 1968.

[92] Zhou, C. Y., Yu, T. X., Lee, S. W. R. and Suhir, E., "Shock Test Methods and Test Standards for Portable Electronic Devices", in *Structural Dynamics of*

Electronic and Photonic Systems (eds E. Suhir, D. S. Steinberg and T. X. Yu), John Wiley & Sons, Inc., Hoboken, NJ, USA, 2011.

[93] Zhou, C.Y., Yu, T.X., Suhir, E., "Design of Shock Table Tests to Mimic Real-Life Drop Conditions," *IEEE Transactions on Components and Packaging Technologies*, vol.32, no.4, pp.832,837, Dec. 2009

[94] http://www.tml.jp/e/download/catalog/STRAIN_GAUGES.pdf

LIST OF PUBLICATIONS

1. "Effect of Disk Clamping Conditions on the Operational Shock Response of Hard Disk Drives", Gu, B; Shu, DW; Yap, FF; et al., IEEE TRANSACTIONS ON MAGNETICS, 47 (7), JUL 2011.
2. "Shock Pulse Amplitude and Width Effects on the Shock Response of an Operational Disk Drive", Gu, B; Shu, DW; Shi, BJ, INTERNATIONAL JOURNAL OF MODERN PHYSICS B, 24 (1-2): 209-214 JAN 20 2010.
3. "Modal Analysis and Damping Measurement of the Head Arm Assembly of a Small Form Factor Hard Disk Drive ", Shi, BJ; Gu, B; Shu, DW; et al., INTERNATIONAL JOURNAL OF MODERN PHYSICS B, 24 (1-2): 26-33 JAN 20 2010.
4. "Dynamic Force Measurement of a Head Arm Assembly of a Hard Disk Drive by Numerical Analysis and Experiments", Gu, B; Shu, DW; Fujii, Y; et al., IEEE TRANSACTIONS ON MAGNETICS, 45 (11): 5034-5037 Part 1 NOV 2009.
5. "Shock Response of the Clamped Disk in Small Form Factor Hard Disk Drive", Gu, B; Shu, DW; Shi, BJ; et al., INTERNATIONAL JOURNAL OF MODERN PHYSICS B, 22 (9-11): 1592-1597 APR 30 2008.
6. "FEA Simulation of Linear and Rotary Drop Test for Small Form Factor HDD", Gu, B; Shu, DW; Luo, J; et al., IEEE ICMA 2006: Proceeding of the 2006 IEEE International Conference on Mechatronics and Automation, Vols. 1-3, Proceedings: 1264-1268, 2006.